

Universidade de São Paulo
Instituto de Astronomia, Geofísica e Ciências Atmosféricas
Departamento de Astronomia

Miguel Andrés Páez Murcia

**Study of the formation of Kelvin-Helmholtz
instability and shocks in coronal mass ejections**

**Estudo da formação da instabilidade Kelvin-
Helmholtz e choques em ejeções de massa
coronal**

São Paulo
2018

Miguel Andrés Páez Murcia

**Study of the formation of Kelvin-Helmholtz
instability and shocks in coronal mass ejections**

**Estudo da formação da instabilidade Kelvin-
Helmholtz e choques em ejeções de massa
coronal**

Thesis presented to the Astronomy
Department at Instituto de Astronomia,
Geofísica e Ciências Atmosféricas da
Universidade de São Paulo as a partial
requisite for obtaining a PhD in Sciences.

Research Field: Astronomy
Advisor: Prof. Dr. Vera Jatenco Silva Pereira

Versão corrigida. O original encontra-se
disponível na Unidade.

São Paulo

2018

Dedicada al gran amor de mi vida: Mi Mamá

Acknowledgements

Neste momento gostaria de expressar meu sentimento de agradecimento com todas aquelas pessoas que me permitiram avançar em minha vida profissional e pessoal. Acho difícil conseguir expressar todo meu afeto e gratidão à elas.

Gostaria de agradecer de maneira especial à minha orientadora a Professora Vera Jatenco por sua atenção, paciência e ajuda, em estes quatro anos.

Gostaria de agradecer a meus colaboradores de pesquisa Professora Merav Opher e Professor Diego Falceta-Gonçalves.

Gostaria de agradecer à Professora Elisabete M. de Gouveia Dal Pino por seu curso de plasma.

Quiero agradecer inmensamente a Tatiana por su amor y ayuda durante estos años.

Quero agradecer a meus amigos Juan, Gustavo, Ana, Nathália, Paty, Rogério, Reinaldo, Douglas, Daiane, Larissa, Marília, Jhon, Irapuan, Raphael Alves, Raphael Oliveira e Bruno.

A mi Mamá, mi hermana y mis sobrinas por su amor incondicional.

Un rincón de mi corazón es exclusivo de Newton, Paco, Lupe, Lucas y Simona. Sin dudar sé que todos ustedes me hubieran acompañado en todas las noches de ciencia y café.

Gostaria de agradecer à Universidade de São Paulo, em especial aos Professores e Funcionários do Departamento de Astronomia quem tornam do Instituto um ambiente adequado para o desenvolvimento da ciência.

Agradeço ao suporte financeiro da CAPES (Coordenação de Aperfeiçoamento de Pessoal de Nível Superior–PROEX 3474/2014)

Esta tese/dissertação foi escrita em \LaTeX com a classe IAGTESE, para teses e dissertações do IAG.

Resumo

As ejeções de massa coronal (do inglês coronal mass ejections, CMEs) são consideradas traçadores da atividade solar. Durante a evolução das CMEs no vento solar (do inglês solar wind, SW), o choque e o envoltório (do inglês sheath, Sh) são estabelecidos. Nesta fase, a transferência da energia e a termalização do choque podem ter origem através de vários processos, entre eles instabilidades e aceleração de partículas. Aqui nós apresentamos dois estudos relacionados às CMEs. No primeiro estudo, analisamos a existência da instabilidade Kelvin–Helmholtz (KHI) nas interfaces CME–Sh e Sh–SW. Para isto, supomos duas CMEs que se propagam independentemente no SW lento e rápido. Modelamos as velocidades, densidades e a intensidade do campo magnético dos envoltórios e SW nos flancos das CMEs, a fim de resolver a condição de Chandrasekhar para a existência da KHI magnética. Nossos resultados revelam que a formação da KHI pode ser mais provável na CME que se propaga no SW lento do que na CME que se propaga no SW rápido. Isto é devido a um maior cisalhamento entre a CME e o SW lento. Além disso, encontramos que a interface Sh–SW é ser mais suscetível à instabilidade. No segundo estudo, examinamos as distribuições das regiões de aceleração de partículas e turbulência em choques ondulados com características semelhantes a ondas. Assumimos choques ondulados como resultado de perturbações do SW bimodal, deflexão da CME, expansão irregular da CME, e flutuações onipresentes na coroa solar. Construímos choques sem ondulações usando perfis Gaussianos. Com adição de funções semelhantes a ondas, obtemos os choques ondulados. Para ambos tipos de choques, calculamos os ângulos entre o vector normal ao choque e o campo magnético coronal radial, assim classificamos as regiões como quase-paralelas e quase-perpendiculares que são ligadas às regiões de aceleração de partículas e turbulência, respectivamente. Nossos cálculos mostram a predisposição do choque para o fenômeno de

aceleração de partículas, e indicam que a expansão irregular da CME é o fator de maior relevância neste processo. Consideramos que assumir ondulações nos choques pode ser essencial nos estudos de problemas atuais como injeção de partículas, instabilidades, jatos e termalização dos choques.

Palavras-chave: Sol: ejeções de massa coronal (CMEs) – Sol: campos magnéticos – ondas de choque – vento solar – instabilidades – emissão de partículas

Abstract

The coronal mass ejections (CMEs) are phenomena that evidence the complex solar activity. During the CME evolution in the solar wind (SW) the shock and sheath (Sh) are established. With these, the transfer of energy and shock thermalization have origin through several processes like instabilities and particle acceleration. Here, we present two studies related to CMEs. In the first study, we analyze the existence of the Kelvin–Helmholtz instability (KHI) at the interfaces CME–Sh and Sh–SW. For this purpose, we assumed two CMEs that propagate independently in the slow and fast SW. We model velocities, densities and magnetic field strengths of sheaths, and SW in the CMEs flanks, in order to solve the Chandrasekhar condition for the magnetic KHI existence. Our results reveal that KHI formation is more probably in the CME that propagate in the slow SW than in CME propagating in the fast SW. It is due to large shear flow between the CME and the slow SW. Besides we find that the interface Sh–SW is more susceptible to the instability. In the second study, we examine the distributions of particle acceleration and turbulence regions around CME-driven shocks with wave-like features. We consider these corrugated shock as the result of disturbances from the bimodal SW, CME deflection, irregular CME expansion, and the ubiquitous fluctuations in the solar corona. We model smooth CME-driven shocks using polar Gaussian profiles. With the addition of wave-like functions, we obtain the corrugated shocks. For both shock types are calculated the shock normal angles between the shock normal and the radial upstream coronal magnetic field in order to classify the quasi-parallel and quasi-perpendicular regions linked to the particle acceleration and turbulence regions, respectively. Our calculations show the predisposition of the shock to the particle acceleration and indicate that the irregular CME expansion is the relevant factor in the particle acceleration process. We consider that these wave-like

features in shocks may be essential in the study of current problems as injection particle, instabilities, downstream-jets, and shock thermalization.

Key words: Sun: coronal mass ejections (CMEs) – Sun: magnetic fields – shock waves – solar wind – instabilities – particle emission

List of Figures

2.1	The illustrative internal (panel (a)) and atmosphere structure (panel (b)) of the Sun. From the center, the Sun is composed by the core ($\sim 0.25 R_{\odot}$, $\sim 15.7 \times 10^6$ K), radiative zone ($\sim 0.86 R_{\odot}$, $\sim 8 \times 10^6$ K) characterized by radiative transport of energy (wave-like arrows), convective zone ($\sim 1 R_{\odot}$, ~ 6600 K) characterized by convective motions (circle arrows), photosphere (thickness ~ 550 km, 4300 K), chromosphere (thickness ~ 2.5 Mm (10^3 km)), and finally the solar corona ($> 10^6$ K) (gray shadow). Values taken from (Priest, 2014). Panel (b) shows the magnetic field topology of the corona (gray lines, image from Nasa) and solar structures of coronal hole (blue lines), active region (yellow lines), and coronal loops (orange lines). .	32
2.2	Plot of the behavior of β , Equation (2.1) over AR. The plot shows the β -values above an AR in function of the height from the photosphere to solar wind (c.f., Gary 2001). In the left side, the black thick line indicates the model for a sunspot with $B \approx 2500$ G (Gauss), while the black thin line in the right side represents the plage region in the chromosphere with $B \approx 100$ G. Source: Gary (2001).	34
2.3	Observation of the SW speed from Ulysses spacecraft during the two first orbits. On the left the observation in the solar minimum, and at right solar maximum. Source: McComas et al. (2003).	35
2.4	Image of the narrow CME of Gilbert et al. (2001). The authors show the evolution of a narrow CME by images from LASCO C2 on 1999 April 24. We highlight the magnetic field jet-like structure through the red lines. Source: Gilbert et al. (2001).	36

2.5 The time step of the CME of 1999 June 11 between 11:06 UT to 12:06 UT from LASCO/C2 (Brueckner et al., 1995). Snapshots illustrate the CME evolution in distances from 2.0 to 6.0 R_{\odot} between 11:05 to 12:50 UT. For the CME we show the three-part structure: core, cavity, and frontal loop, together with shock and sheath. Particularly, Bemporad and Mancuso (2011) and Bemporad et al. (2014) driven full set of plasma physical parameters in shock from ultraviolet and white-light coronagraphic data. 37

2.6 Schematic plot proposed in Zhang and Dere (2006) for the CME kinematic. The author emphasized in three dynamical phases: initiation, acceleration, and propagation, related to the flare phases of preflare, rise, and decay of the associated flare, respectively. Source: Zhang and Dere (2006). 38

2.7 The shock wave formation (orange line) allow that the downstream (post-shock) and upstream (pre-shock) regions to be established. The subscript 1 and 2 in density (ρ), magnetic field (blue arrows, \mathbf{B}), velocity (\mathbf{V}), and angle (θ), we identify the downstream and the upstream region quantities, respectively. 41

2.8 Schematic view of the two shocks types. In panel (a) we show the shock originated in the condition that driver propagate in the plasma. We indicate the faster CME propagating in the equator region with a shock wave (blue line) in CME nose region. We highlight the CME three parts structure region i.e., core, cavity, and frontal loop, CME-pause (orange line), the sheath region (green shadow) behind the shock, coronal magnetic field lines (MFL, gray lines). In panel (b), we illustrate the bow shock (blue line) that occurs when there is the SW collision between SW with the magnetosphere. In this case, the stand-off distance to the driver is constant and the piston and the shock maintain the same velocity. In a similar way to the panel (a), here originates the magnetosheath (green shadow) between magnetopause (orange line) and shock. 42

2.9	Schematic of mechanism of SEPs acceleration that define the SEPs types. Panel (a) shows the gradual SEPs accelerated in the shock waves driven by CMEs While panel (b) shows the impulsive SEPs associated to the open magnetic field lines that are accelerated in the magnetic reconnection process present in the flare. Source: Reames (1999)	44
3.1	Schematic of the linear phase of the KHI between two plasmas indicated by subscripts 1 (higher gray shadow) and 2 (light gray shadow). Panel (a) indicates the hydrodynamical conditions of the KHI where the magnetic field \mathbf{B} is perpendicular to the shear flow $\hat{\mathbf{x}}$ (blue arrow) at the interface between fluids (orange line). The KHI vortices formation is indicated by the black dashed arrows. For two plasmas we consider: $\mathbf{V}_1 > \mathbf{V}_2$, $\rho_1 > \rho_2$, and $\mathbf{B}_1 > \mathbf{B}_2$, in order to illustrate the interface CME and SW. In panel (b), we present the MHD KHI case with the \mathbf{B} (black arrows) parallel to $\hat{\mathbf{x}}$ in the interface (green line). The KHI vortices size are shown larger in the HD case than in the MHD case, in order to emphasize the role of the magnetic field tension opposing to the KHI origin.	48
3.2	First KHI observations in the CME environments. The image was observed in the AIA/SDO 131Å (Fe XX). The X and Y (both in arcsecs) are orientated for the west and north, respectively. Source: Foullon et al. (2011)	50
3.3	CME images of event occurred on 2010 April 8. This image corresponds to 193 Å (Fe XII). The larger and small boxes correspond to CME and KHI observations, respectively. The columns of the frames in the right side correspond to the temporal evolution of the vortices in 211 Å (Fe XIV) images. Source: Ofman and Thompson (2011)	52
3.4	Observations of the KHI by Möstl et al. (2013) . In panel (a) the authors show the AIA/SDO images in 304 Å (He II) channel (orange images). The gray images corresponding to the AIA/SDO observations in 171 Å (Fe IX) channel. Source: Möstl et al. (2013)	53

4.1	<p>Illustrative two-dimensional scheme of the CME 1 (panel (a)) and CME 2 (panel (a)) propagating in the slow and fast solar wind (SW), respectively. The panels (a) and (b) show our zones proposed for the KHI formation on CME flanks. We also show the CMEs internal structure (core and cavity) and the presence of the external structures sheaths and shocks for both CMEs. The sheaths of the CME 1 and CME 2 are represented as the cyan and yellow shaded regions, respectively. We show the helical magnetic structures of both CMEs (curved black arrow, $\mathbf{B}_{\text{CME}}^{\text{Helical}}$) evolved by the sheaths magnetic field lines shown $\mathbf{B}_{\text{Sh}}^{\text{Slow}}$ (orange lines) and $B_{\text{Sh}}^{\text{Fast}}$ (green lines) lines and the magnetic field lines of the SW $\mathbf{B}_{\text{SW}}^{\text{Slow}}$ (purple lines) and fast SW $\mathbf{B}_{\text{SW}}^{\text{Fast}}$ (pink lines). We indicate the KHI region by dashed black line rectangle together with the shear flow, $\hat{\mathbf{k}}$, on CME flanks. The solid black point represents the Sun. In our calculation we assume the solar rotation in $\hat{\mathbf{z}}$ direction. Source: Páez et al. (2017).</p>	58
4.2	<p>The panels show the SWs velocity, Equation (4.3) (km s^{-1}, solid blue line), SWs density Equation (4.4) (cm^{-3}, dashed green line) with the SWs magnetic field strength Equation (4.5) (G, dotted red line) of the slow (a) and fast (b) SW. The shadow cyan and yellow in background are intentional to empathize the sheath color of Figure 4.1. The axis show the color plot feature associated. Source: Páez et al. (2017).</p>	60
4.3	<p>Comparative panels for the slow in (a), $B_{\text{SW}}^{\text{Slow}}$, Equation (blue continuous line) and fast in (b), $B_{\text{SW}}^{\text{Fast}}$ (red continuous line) SW (Equation (4.5)) and magnetic fields models. In orange Dulk and McLean (1978) profile. In green Patzold et al. (1987). In pink Gopalswamy and Yashiro (2011) profile (G & Y 2011). Source: Páez et al. (2017).</p>	61

- 4.4 The figure shows the CME 1 velocity profile ($V_{\text{CME } 1}$, solid blue line) and sheath 1 ($V_{\text{Sh } 1}$, dashed blue line), together with the CME 2 velocity ($V_{\text{CME } 2}$, solid red line) and sheath 2 ($V_{\text{Sh } 2}$, dashed red line) in the outer corona between 4 to 30 R_{\odot} (solid black vertical lines). The shadows color are related to sheath structure colors in Figure 4.1. The cyan and yellow regions between solid and dashed blue and red lines represent the amplitude of the shear flow function, $S(r)$, Equation (4.15) for CME 1 and CME 2 cases, respectively. Source: Páez et al. (2017). 62
- 4.5 The schematic magnetic configuration of the KHI regions on the CME flanks. The panel (a) generalize the CME, sheath and SW plasmas by gray shadows and indicate the interfaces CME–Sh (green shadow), Sh–SW (orange shadow), and the shear flow, $\hat{\mathbf{k}}$ (dashed black arrows). We show the CME helical magnetic field $\mathbf{B}_{\text{CME}}^{\text{Helical}}$ by black arrow among the symbols \odot and \otimes that represent the magnetic field polarities outward and inward, respectively. The sheaths (\mathbf{B}_{Sh}) and SW (\mathbf{B}_{SW}) magnetic field lines by blue and green arrows, respectively. In panel (b) we amplify the structure of interface CME–Sh. We decompose the $\mathbf{B}_{\text{CME}}^{\text{Helical}}$ in its poloidal ($\mathbf{B}_{\text{CME}}^{\text{Pol}}$, red arrow) and toroidal ($\mathbf{B}_{\text{CME}}^{\text{Tor}}$, brown arrow) components. We simplify our calculation of these components by assuming θ angle for the stretch caused by propagation and expansion of the CME on the helical structure. We assume that $\mathbf{B}_{\text{CME}}^{\text{Tor}}$ affect the KHI formation while the $\mathbf{B}_{\text{CME}}^{\text{Pol}}$ not (Chandrasekhar, 1961). The panel (c) shows the interface Sh–SW. The structure of this boundary is less complex to CME–Sh interface due to the sheath structure is formatted by compression of the SW magnetic field lines. Source: Páez et al. (2017). . . 65

4.6 Plots for the KHI formation constraints. The panels (a) and (b) show the CME magnetic field, $B_{\text{CME}}^{\text{KH}}$, (Equation (4.16), solid red line) necessary for the KHI formation and the logarithm of the shear flow, $S(r)$, (Equation (4.15), dashed black line) for the interfaces CME 1–Sh and CME 2–Sh, respectively. The values below the $B_{\text{CME}}^{\text{KH}}$ curve are the appropriate for KHI formation. The panels (c) and (d) show the SW magnetic field strength, B_{SW} , (Equation (4.5), dotted blue line), SW magnetic field strength for the KHI formation, $B_{\text{SW}}^{\text{KH}}$, (Equation (4.22), solid red line) and the shear flow, $\xi(r)$ (Equation (4.21), dashed black line). The values below the $B_{\text{SW}}^{\text{KH}}$ curve are linked with KHI formation. The blue shadow along the B_{SW} represent the error of $\pm 30\%$ assumed in the SW model, while the red shadow along of $B_{\text{CME}}^{\text{KH}}$ and $B_{\text{SW}}^{\text{KH}}$ represent the error propagation of $\pm 34\%$. The cyan and yellow shadow represent the colors assumed in Figure 4.1 for the sheaths structure. We find CME and slow SW magnetic field values less than 7.9 ± 2.7 mG and 16.8 ± 5.7 mG, respectively, may allow the KHI in slow SW environment. While CME and fast SW magnetic field values less than 3.0 ± 1.0 and 7.0 ± 2.4 mG, respectively, allow the instability in fast SW environment. These results are summarized in Table 4.1. Our calculation show that KHI magnetic field strength of Sh–SW interfaces are larger than CME–Sh interfaces for both CMEs cases, in this way we comment that Sh–SW interface will be susceptible to the KHI formation. Source: [Páez et al. \(2017\)](#).

5.1 Schematic view of a meridional view of CME 1, CME 2, and CME 3 and their shocks. We show three different CMEs structures: core; cavity; and frontal loop (Illing and Hundhausen, 1985). For all situations we considered a sheath structure (yellow shadow) formed behind the shocks. The CME-pause and coronal magnetic field lines (MFL) are indicated by the red and black thin lines, respectively. Panels (a), (b), and (c) indicate the smooth shocks. For the three CME cases, the shock signatures (green, blue, and orange thick lines) are assumed in different latitude locations. The shock morphology preserve similar features to the events of 1999 September 11 (here assumed in the equator region), 1997 November 6, and 1998 June 4 studied in Ontiveros and Vourlidas (2009). Panels (d), (e), and (f) show our proposed corrugated shocks. We assume this type of shock by imposing wave-like features from bimodal SW (e.g., Manchester et al., 2005), CME deflection (e.g., Kay et al., 2013, 2015), CME irregular expansions (e.g., Evans et al., 2011), and ubiquitous fluctuations of density and magnetic field of the solar corona (e.g., Warmuth and Mann, 2005; Evans et al., 2008; Zucca et al., 2014). For the six cases, we analyze throughout the shock width in order to provide a general diagnostic. But particularly, we adopt the supercritical shocks conditions at the convex regions (rounded) indicated by the green, blue, and orange transverse lines (e.g., Bemporad and Mancuso, 2011; Bemporad et al., 2014). Source: Páez et al. (2018). 81

- 5.2 Reconstruction of the shocks shapes presented in Figure 5.1. Panel (a) shows the function $h(\phi)$ (black dashed line) Equation (5.1), together with the smooth shocks $S_1(\phi)$ (green line), $S_2(\phi)$ (blue line), and $S_3(\phi)$ (orange line), Equations (5.2), (5.4), and (5.5), respectively. In panel (b) we show the corrugated shocks $C_1(\phi)$ (green line), $C_2(\phi)$ (blue line) and $C_3(\phi)$ (orange line), Equation (5.6). The gray shadow between 2.0 to 4.0 R_\odot corresponds to the region where the shock are analyzed. In this interval we considerate the shock formation ($\sim 1.5 R_\odot$, e.g., [Ma et al. 2011](#); [Zucca et al. 2014](#); [Gopalswamy et al. 2016](#)) and particle acceleration ($\sim 3.0 R_\odot$, e.g., [Reames 2009](#); [Gopalswamy et al. 2012](#)). For both shocks types we classify the quasi-parallel and quasi-perpendicular regions in order to understand the shock predisposition for particle acceleration and turbulence in the upstream shock region. The green, blue, and orange transverse lines at convex (rounded) regions indicate the locations where we assumed the supercritical shock conditions (e.g., [Bemporad and Mancuso, 2011](#); [Bemporad et al., 2014](#)). The gray half-circle represents the Sun. Source: [Páez et al. \(2018\)](#). 83
- 5.3 Corrugated function $k(\phi)$ (R_\odot), Equation (5.7) (blue line), and its contributions $k_1(\phi)$, Equation (5.8) (maroon line), $k_2(\phi)$, Equation (5.9) (green line); and $k_3(\phi)$, Equation (5.10) (red line) as function of polar angle coordinate, ϕ . The $k(\phi)$ function is imposed on smooth shocks $S_m(\phi)$, Equations (5.2), (5.4), and (5.5), in order to construct the corrugated shock, $C_m(\phi)$, Equation (5.6). The blue shadow indicate the amplitude of 0.3 R_\odot and angular width $\sim \pi/6$ rad ($\sim 30^\circ$) of the larger undulations. Source: [Páez et al. \(2018\)](#). 84

- 5.4 Schematic comparison between smooth, panel (a), and corrugated shocks, panel (b). We indicate the differences between CME piston (gray shadow), CME-pause (red line), downstream or sheath (yellow shadow), upstream (orange shadow) of the shock (black thick arrows), and distribution of the shock normal vectors ($\hat{\mathbf{n}}$, red arrows). For both cases we assume the coronal magnetic field lines (MFL) (black thin arrows) turbulent disposed in the sheath region and radially in the upstream region. We classify the quasi-parallel (Q- \parallel) and quasi-perpendicular (Q- \perp) regions by calculation of the shock normal angle, θ_{Bn} , between shock normal, $\hat{\mathbf{n}}$, and the radial upstream coronal magnetic field, ($\mathbf{B}_{\text{cor}}^{\text{up}}$). Our results for the smooth and corrugated shock in Figure 5.5 are illustrated by irregular distributions filamentary structures (blue structures) in the Q- \parallel upstream regions. Source: Páez et al. (2018). 86
- 5.5 Plots of shock normal angles for smooth, $\theta_{\text{Bn}}^{\text{Sm}}(\phi)$, and corrugated $\theta_{\text{Bn}}^{\text{Cm}}(\phi)$ shocks, with $m = 1, 2, 3$, see Figure 5.2. Panel (a) shows the θ_{Bn} values for the three smooth shocks, and panels (b), (c) and (d) show separately the $\theta_{\text{Bn}}^{\text{Sm}}(\phi)$ (black dotted line), and $\theta_{\text{Bn}}^{\text{Cm}}(\phi)$ (color continuous line) values for each one of the shocks. The plots are associated to the color features in Figures 5.1 and 5.2, i.e., the shocks 1, 2, 3 in green, blue and orange, respectively. The quasi-parallel (Q- \parallel , $0 \leq \theta_{\text{Bn}} \leq \pi/4$) and quasi-perpendicular (Q- \perp , $\pi/4 \leq \theta_{\text{Bn}} \leq \pi/2$) regions around the shocks are indicated by yellow and white background shadow colors separated by red line of $\theta = \pi/4$ rad. The gray shadows in the plots indicate the initial supercritical regions assumed from Figure 5.2. The results between smooth and corrugated shocks are illustrated in the Figure 5.4 by distributions of filamentary structures in the upstream regions for quasi-parallel θ_{Bn} values. Source: Páez et al. (2018). 88

List of Tables

4.1	Results from Figure 4.6 for the CME 1 and CME 2 cases for 4 and 30 R_{\odot} at the CME–Sh and Sh–SW interfaces. Shear function S (km s^{-1}), the CME magnetic field strengths for the KHI existence $B_{\text{CME}}^{\text{KH}}$ (mG), the shear function ξ (km s^{-1}) and the SW magnetic field strengths for the KHI existence $B_{\text{SW}}^{\text{KH}}$ (mG).	70
5.1	Values of the constants a_i (R_{\odot}), and b_i (dimensionless) of the $p_m(\phi)$ function, Equation (5.3), in order to constructed the symmetric shocks 2 and 3.	85

Contents

1. Introduction	25
2. Coronal mass ejections (CMEs)	29
2.1 Solar observations	29
2.2 The Sun	31
2.3 Solar wind (SW)	33
2.4 Coronal mass ejections	35
2.5 Shock waves	40
2.6 Solar energetic particles (SEPs)	44
<i>Part I</i>	46
3. Kelvin–Helmholtz instability (KHI) in coronal mass ejections	47
3.1 Introduction	47
3.2 KHI in coronal mass ejections	49
4. Kelvin–Helmholtz instability at the CME–Sheath and Sheath–Solar Wind interfaces	55
4.1 Methodology	56
4.1.1 Solar wind model	57
4.1.2 Coronal mass ejection model	59
4.1.3 Shock and sheath structures	63
4.2 KHI formation in boundary layers	64
4.2.1 Interface between CME and its sheath structure	66
4.2.2 Interface between the sheath and solar wind	68

4.3 Discussion and conclusions	71
<i>Part II</i>	75
5. <i>SEPs and self-turbulence regions in corrugated CME-driven shocks</i>	77
5.1 Methodology	79
5.1.1 Coronal smooth shocks model	80
5.1.2 Coronal corrugated shocks model	82
5.2 Calculation	87
5.2.1 Shock normal angles calculation	89
5.3 Discussion and conclusions	91
6. <i>Conclusions and perspectives</i>	95
<i>Bibliography</i>	97
<i>Appendix</i>	115
A.	117

Introduction

The scientific advances and partial comprehension of the solar phenomena have allowed to understand the relevance of the space weather sciences in our tech lifestyle. The space weather sciences explore three crucial topics: (*i*) energy origin in the Sun and its atmosphere, (*ii*) energy propagation in the interplanetary space, and (*iii*) energy deposited in the magnetosphere and upper atmosphere of the Earth (c.f., [Echer et al., 2005](#)). Our work focuses on the first item: Sun and its solar atmosphere. This involves the solar physics science, which covers studies from the magnetic field generation in the convective region by dynamo process, to the propagation of coronal mass ejections (CMEs) in the solar corona. The solar physics is known as starting point of solar-like studies in stellar, planetary and astrophysical plasma sciences. Among some works comparable with solar physics studies we mentioned, (*i*) stellar cycle (e.g., [Estrela and Valio, 2016](#)), (*ii*) stellar wind, e.g., isolated supergiant stars (e.g., [Martínez-Núñez et al., 2017](#)), (*iii*) stellar flares (e.g., [Davenport, 2016](#)), (*iv*) ejections like solar CME (e.g., [Collier Cameron et al., 1990](#); [Villarreal D'Angelo et al., 2018](#); [Odert et al., 2017](#)), and even (*v*) solar-twins studies (e.g., [Galarza et al., 2016](#)). For the incoming years is expected that these types of studies grow due to the continuous discovering of the systems as TRAPPIST-1 ([Gillon et al., 2017](#)), and new telescope era that includes projects as: European Extremely Large Telescope (e.g., [Vernin et al., 2011](#)), The Giant Magellan Telescope (e.g., [Johns et al., 2012](#)), James Webb Space Telescope (e.g., [Mather, 2010](#)), Parker Solar Probe (e.g., [Fox et al., 2016](#)), and Solar Orbiter (e.g., [Müller et al., 2013](#)).

The spectrum of solar phenomena is broad, but the flares, the CMEs, and the solar wind (SW) have been of greatest importance in the last decades. The flares and CMEs are eruptive and sporadic phenomena related to the accumulation of magnetic energy,

while the SW is a constant flux of plasma. The first flare detection was associated with the observation made by Carrington in 1859, while the first CME was detected in the decade of the 1970s (Tousey, 1973), curiously more than one hundred years after the Carrington flare. The CMEs are the strongest ejections of plasma and magnetic field which reconfigure the coronal magnetic field (e.g., Low, 2001; Liu et al., 2009), and release its stored energy in the interplanetary space (Emslie et al., 2004). Due to its complexity and random occurrence, the CMEs are analyzed through observations, theoretical analysis, and numerical simulations. Thereby, the CMEs are one of the most important phenomena in the space sciences. In super-Alfvénic CMEs ($> 800 \text{ km s}^{-1}$), shock waves are originated in low corona distances (e.g., Ma et al., 2011; Zucca et al., 2014; Gopalswamy et al., 2016), where the radio Type II burst (Wild and McCready, 1950; Uchida, 1960), and Moreton waves (Moreton, 1960; Moreton and Ramsey, 1960) evidence the shock formation. Together with the shock wave, the sheath is established by compression of the coronal plasma caused by the CME expansion and propagation. These two structures, shock and its sheath, proportionate the convenient conditions for acceleration of particles (e.g., Zank et al., 2000; Manchester et al., 2005; Kozarev et al., 2013), by the diffuse shock acceleration (e.g., Bell, 1978a,b; Blandford and Ostriker, 1978). These are known as gradual solar energetic particles (electrons, protons, ions, hereafter SEPs, e.g., Reames 1999, 2013).

The shock waves are originated in the CME flanks or in the CME nose regions (e.g., Ontiveros and Vourlidas, 2009). In this way, some shocks are associated to SEPs origin in flanks (e.g., Kahler, 2016), or at shock nose (e.g., Reames et al., 1997; Reames, 1999). Faster CMEs ($\sim 2000 \text{ km s}^{-1}$) can be called large SEPs events, associated with the Ground Level Enhancement (GLE) events, where the particle acceleration occur in ranges of ~ 2.0 to $\sim 4.0 R_{\odot}$, but with an average in $\sim 3.0 R_{\odot}$ (e.g., Reames, 2009; Gopalswamy et al., 2012). The particle acceleration occurs in the shock supercritical regions, where the downstream Alfvénic Mach number, M_A , is larger than the critical (crt) Mach number, M_A^{crt} , in which the flows and sound velocities are equivalent (e.g., Edmiston and Kennel, 1984). The shock normal angle θ_{Bn} , between the shock normal and the upstream magnetic field, can allow that supercritical shock sustain two phases: the quasi-parallel ($0 \leq \theta_{\text{Bn}} \leq \pi/4$) and quasi-perpendicular ($\pi/4 \leq \theta_{\text{Bn}} \leq \pi/2$) (Balogh and Treumann 2013 page 28). These two phases are related to the particle acceleration or turbulence.

The SEPs travel through the SW magnetic field lines from the flare, or from the shock

waves. These two phenomena, define the SEPs types: impulsive and gradual (Reames, 1999, 2013). The first is related to the magnetic reconnection process in the flare evolution and the second one to the diffuse shock acceleration in shock waves. From two mechanisms the shock wave is more efficient. Besides of particles accelerated during its formation, the shock can accelerate particles during its propagation in the interplanetary space. The SEPs are constituted by protons, electrons, He and Pb that evidence the solar corona composition. The SEPs abundance is relevant in order to understand the process of acceleration and transport of the particles. The accelerated particles have energies from 10 keV to 1 GeV, for non-relativistic and relativistic conditions, respectively. The near-relativistic particles can travel up to 90% of the light speed.

The dynamical process and sophisticated magnetic field configurations in the solar corona allow the existence of phenomena as waves in streamer structures (e.g., Chen et al., 2010), instabilities as Rayleigh–Taylor instability in filamentary structure (e.g., Isobe et al., 2005; Innes et al., 2012), and Kelvin–Helmholtz instability (hereafter KHI) in the CME environment (e.g., Foullon et al., 2011), among others. These instabilities are the consequence of microscopic and macroscopic interactions that increase the gradients of velocity, pressure or magnetic field, which allow the exponential growth of the initial perturbations even to turbulent conditions. The KHI is a common phenomenon that occurs in plasma and fluids as rotating regions known as KHI vortices. These vortices take energy from shear at the plasma interface and became in rotating motions. In conditions where the magnetic field is parallel to the shear flow interface, the tension of the magnetic field lines opposes to the growth of the vortices affecting the KHI formation (Chandrasekhar, 1961). Thus, the KHI observations allow the understanding of the geometry and the strength of the magnetic field before the turbulence generation. The KHI has been detected in some astrophysical surroundings as: planetary environments (Hasegawa et al., 2004; Amerstorfer et al., 2007; Sundberg et al., 2010), stellar jets (Micono et al., 1998), solar atmosphere and coronal streamer (Cavus and Kazkapan, 2013; Feng et al., 2013). In CME environments only exists three KHI observations (e.g., Foullon et al., 2011; Ofman and Thompson, 2011; Möstl et al., 2013). These observations motivated some theoretical studies as Zaqarashvili et al. (2010, 2014, 2015) and Zhelyazkov et al. (2015) for the twisted flux tubes, and Páez et al. (2017) for the CME–Sheath (CME–Sh) and Sheath–Solar–wind (Sh–SW) interfaces in the outer coronal distances.

This thesis is structured in two parts. The first part presents our study of the existence of the KHI at the CME–Sh and Sh–SW interfaces. Motivated by KHI observations in the low corona close to the solar surface, we analyze the KHI formation in the outer corona. Our work is focused on the interfaces of CME–Sh and Sh–SW of two CMEs that propagate in the slow and the fast SW. We are interested in these unequal environments to identify the suitable conditions for the KHI formation. We model the velocities, densities and magnetic field strengths of the SW, and the sheaths, in order to model the condition for KHI formation proposed in Chandrasekhar (1961). This work was published in *The Astrophysical Journal* volume 851 page 112¹ on 2017 December (Páez et al., 2017). The second part presents our analysis of the distributions of SEPs and self-turbulence in the corrugated shocks in the low corona distances, submitted to *The Astrophysical Journal* on 2018 May, currently under revision (Páez et al., 2018). Based in the observations of Susino et al. (2015) of the irregular shock front between 2 to 12 R_{\odot} , we discuss the distribution of the SEPs and self-turbulence regions with wave-like shocks fronts imposed from irregularities of the medium as SW types, solar corona, and nonuniform expansion and deflection of the CMEs.

¹ <http://iopscience.iop.org/article/10.3847/1538-4357/aa9753/meta>

Coronal mass ejections (CMEs)

As discussed in Chapter 1, our work focuses on the theoretical studies on the Kelvin-Helmholtz instability, and predisposition to particle acceleration and turbulence at the interfaces in the shocks wave driven by coronal mass ejections (CMEs). In this Chapter, we expose the necessary concepts to understand our methodology and calculation presented in Chapters 4, and 5. First, we present the relevance of the spacecraft coronagraphs for understanding the CME physics. Afterward, we present the fundamental concepts of the Sun and solar wind (SW) phenomenon, in order to understand the morphology and dynamic phases of CMEs, that allow the possible shock formation and their consequences as particle acceleration and turbulence.

2.1 *Solar observations*

The complex nature that is involved in the flares, CMEs, and SW, is studied through an ensemble of spacecraft in order to obtain the more possible information for their understanding. During the last decades were launched a set of spacecrafts where the most notables are the Solar and Heliospheric Observatory (SOHO) launched on 1995 December 2 (Domingo et al., 1995), with Large Angle Spectroscopic Coronagraph (LASCO) onboard (Brueckner et al., 1995), and the Solar Terrestrial Relation Observatory (STEREO) launched by NASA on 2008 October 26 (Kaiser et al., 2008). In conjunction with them, a set of complementary spacecrafts were launched as Yohkoh¹ (Tsuneta et al., 1991), Hinode² (Lites et al., 2013), Solar Dynamics Observatory (SDO) (Pesnell et al., 2012) with The Atmospheric Imaging Assembly (AIA) onboard SDO (Lemen et al., 2012). All these ins-

¹ <http://ylstone.physics.montana.edu/ylegacy/>

² https://www.nasa.gov/mission_pages/hinode/index.html

truments allow acquiring observations in several wavelengths as X-rays (e.g., [Sterling and Hudson, 1997](#)) extreme ultra-violet (e.g., [Tian et al., 2012](#)), and radio (e.g., [Gopalswamy et al., 2001](#)). The use of these wavelengths enable a better understanding of the CME phenomenon.

Each one of the previous spacecraft was launched with the objective to contribute with new observations and supplement each other. The scientific objectives of SOHO are related to the studies of the solar interior, the heating of the solar corona, and the SW acceleration. On the other hand, LASCO is structured in three coronagraphs each one with a different observation range, C1 (1.1 - 3.0 R_{\odot}), C2 (1.5 to 6.0 R_{\odot}) and the C3 (3.7 to 30 R_{\odot}), that maintain the ability to obtain high spatial resolution images. Additionally, STEREO are two identical spacecraft traveling ahead (STEREO-A), and behind (STEREO-B) of the Earth. The mission of STEREO has been allowing to follow the CME propagation through Heliosphere, additionally to studies of the SW properties as the magnetic topology, temperature, velocity, and density. With STEREO the space weather studies scale up to 1 AU ($\sim 215 R_{\odot}$). With these array of spacecrafts, the detection of CMEs has been increased. Before the SOHO era, the averaged occurrence rate was found to increase from 0.2 per day at solar minimum to 3.5 per day at solar maximum (e.g., [Webb and Howard, 1994](#)), with SOHO and LASCO it is known of 0.5 per day near solar minimum to 6 near solar maximum.

For the next years is expected a large increase of observations with the new era of spacecraft. [Parker Solar Probe](#)³ and [Solar Orbiter](#)⁴ are two important solar missions that will be launched on the 2018 and 2019 years, respectively. These space tech will bring new research challenges over the coming years. The Parker Solar Probe, is dedicated to Dr. Eugene Parker whose studies improved the understanding of the Sun, among them like, origin of the SW ([Parker, 1958](#)), dynamo solar (e.g., [Parker, 1993](#)), nanoflares ([Parker, 1988](#)), magnetic reconnection (e.g., [Parker, 1973](#)), heating of the coronal hole ([Parker, 1991](#)), magnetic field structures in solar atmosphere ([Parker, 1989](#)), and others relevant findings. In the similar way, is expected that Parker Solar Probe revolutionizes the current solar physics. This is a spacecraft project part of the Program Living with a Star⁵ of the NASA launched on 2018 August and will make 24 solar orbits over 7-year.

³ <https://www.nasa.gov/content/goddard/parker-solar-probe>

⁴ <http://sci.esa.int/solar-orbiter/55772-solar-orbiter-launch-moved-to-2018/>

⁵ https://lws.gsfc.nasa.gov/program_details.html

The first perihelion through solar corona will occur on 2018 November and the last in 2024 December. The last three orbits will be in distances $< 10 R_{\odot}$. With Parker Solar Probe observations the scientific community expect to understand the structure and the magnetic field, the heating of the solar corona, SW acceleration, and the origin acceleration of energetic particles (e.g., Fox et al., 2016). In a complementary way, the Solar Orbiter spacecraft will make observations of polar regions close to $\sim 60 R_{\odot}$. These observations will allow to understand how the solar magnetic field is generated, and its change of polarity. Solar Orbiter will provide elements to understand how the Sun creates the heliosphere (e.g., Müller et al., 2013). During the seven-year mission, this instrument will measure SW, fields, waves, and energetic particles close enough to the Sun.

2.2 The Sun

The Sun is a star of spectral type G, with radius R_{\odot} equivalent to 6.96×10^5 km and mass of 1.98×10^{30} kg, i.e., ~ 109 and ~ 332 times the radius and mass of the Earth. The solar energy is produced through the nuclear fusion of Hydrogen (H) to Helium (He) in the solar core ($\sim 0.25 R_{\odot}$, $\sim 15.7 \times 10^6$ K). In this process is released energy that establishes the radiative zone ($\sim 0.86 R_{\odot}$, $\sim 8 \times 10^6$ K), continuing in convection motions that allow dynamo process (e.g., Parker, 1955) which generate the solar magnetic field in the convective zone ($\sim 1 R_{\odot}$ km, ~ 6600 K). This magnetic field crosses the photosphere (thickness 550 km, 4300 K), chromosphere (thickness ~ 2.5 Mm (10^3 km), and solar corona ($> 10^6$ K), even cross the interplanetary space conforming the heliosphere. Figure 2.1 shows the interior and the atmosphere structure of the Sun. In panel (a) we show the above mentioned internal layers structure of the Sun with their size and temperature values (c.f., Priest 2014). Panel (b) illustrates the magnetic field structure (gray lines) in the solar corona. This panel highlights the loop magnetic structure (orange closed lines with Ω shape), the coronal holes (CHs, blue open lines) in the solar polar regions, and the active region (AR, yellow lines). These two structures are illustrated from the convection region where the solar magnetic field is generated. Panel (b) is constructed editing the image of magnetic field of the Sun printed by NASA⁶.

The solar atmosphere is the external structure of the Sun. This region is structured

⁶ <https://www.nasa.gov/content/goddard/what-is-solar-activity>

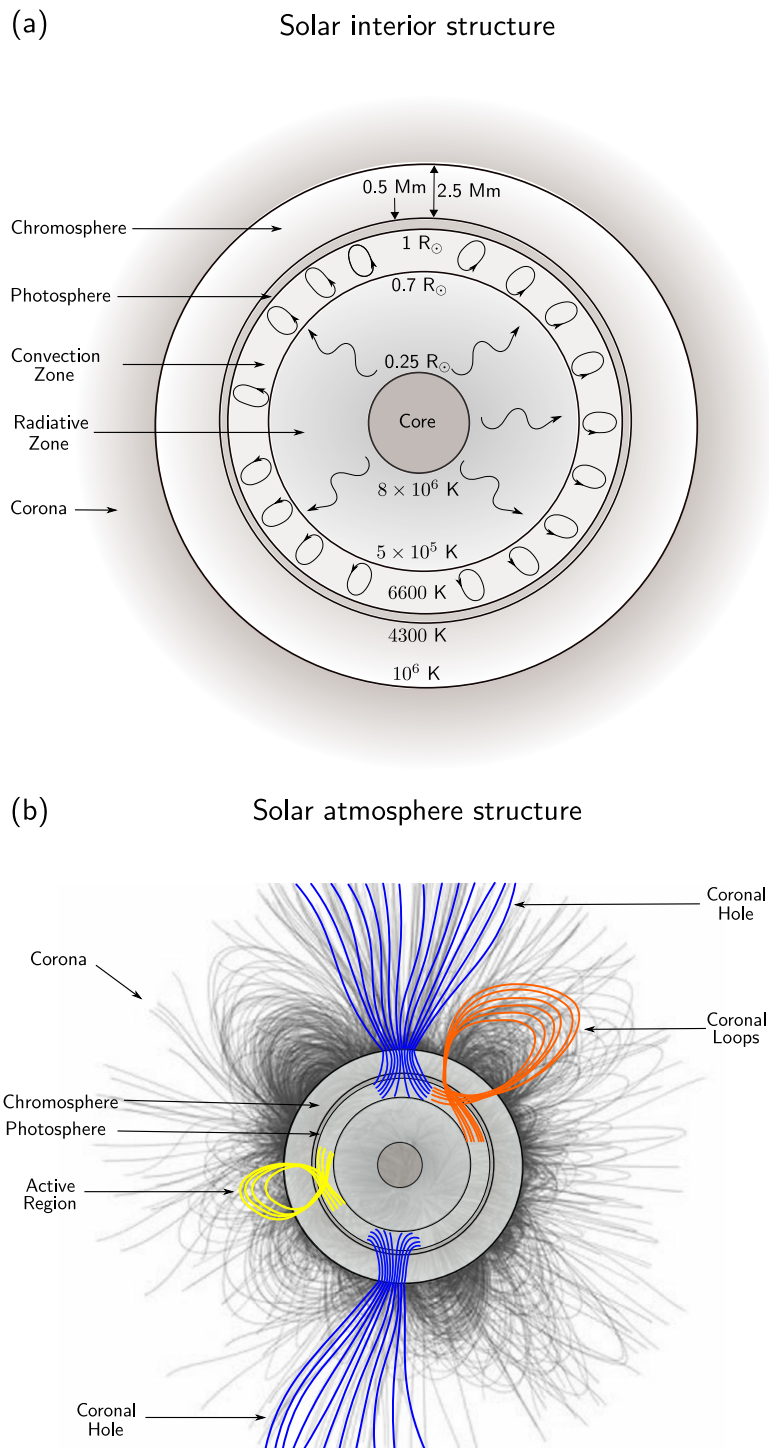


Figure 2.1: The illustrative internal (panel (a)) and atmosphere structure (panel (b)) of the Sun. From the center, the Sun is composed by the core ($\sim 0.25 R_{\odot}$, $\sim 15.7 \times 10^6$ K), radiative zone ($\sim 0.86 R_{\odot}$, $\sim 8 \times 10^6$ K) characterized by radiative transport of energy (wave-like arrows), convective zone ($\sim 1 R_{\odot}$, ~ 6600 K) characterized by convective motions (circle arrows), photosphere (thickness ~ 550 km, 4300 K), chromosphere (thickness ~ 2.5 Mm (10^3 km)), and finally the solar corona ($> 10^6$ K) (gray shadow). Values taken from (Priest, 2014). Panel (b) shows the magnetic field topology of the corona (gray lines, image from [Nasa](#)) and solar structures of coronal hole (blue lines), active region (yellow lines), and coronal loops (orange lines).

in three regions with different properties: the photosphere, chromosphere, and the corona. The solar corona is characterized by low density $\sim 10^{-16}$ g cm $^{-3}$ and range temperature of $> 10^6$ K, even larger than the solar surface > 4300 K. It is known as coronal heating. Two mechanisms have been interpreted as responsible of the chromosphere and coronal heating: (i) the magnetic waves generated in the convection zone, and (ii) the magnetic reconnection process in the magnetic field lines (c.f., [Priest 2014](#)). The corona shows a complex behavior where the magnetic field develops a crucial role. In order to understand the role of the magnetic field it is used the β -plasma parameter as ratio of gas pressure, p_{th} , and magnetic pressure, $p_{\text{mag}} = B^2/2\mu_0$,

$$\beta = \frac{p_{\text{th}}}{p_{\text{mag}}} = \frac{2\mu_0 p_{\text{th}}}{B^2},$$

where μ_0 is the permeability of medium. [Figure 2.2](#) shows the β behavior above an AR and a plage region in the solar surface (c.f., [Gary 2001](#)). In the left side the black thick line indicates the model for a sunspot with $B \approx 2500$ G (Gauss), while the black thin line in the right side represents the plage region in the chromosphere with $B \approx 100$ G. The solar magnetic field has its origin in dynamo process in the tachocline located in the lower boundary of the convection zone. The dynamo process defines the solar cycle as an interval of 11-years where the solar activity change between a minimum to maximum. In the solar minimum the magnetic field is weak in comparison with the solar maximum when occur the peak in magnetic activity. The solar activity is reflected by the increase of sunspots, CMEs, flares, latitudinal distribution of the SW types, emission of extreme ultraviolet and X-ray and larger emission of solar particles.

2.3 Solar wind (SW)

The SW is a constant flux of solar plasma that propagates through the heliosphere and represent the mass loss controlled by the coronal heating and by energy flow between chromosphere and corona. The SW fill the heliosphere transporting plasma and magnetic field. Its composition corresponds to the chemical composition of the solar atmosphere i.e., electrons, protons, heavier ions as He $^{++}$, and heavier ions in different stages of ionization ([Schmelz et al., 2012](#)). The SW interacts with others solar phenomena as the CMEs, and the interplanetary bodies as comets, moons, magnetized and non-magnetized planets (c.f.,

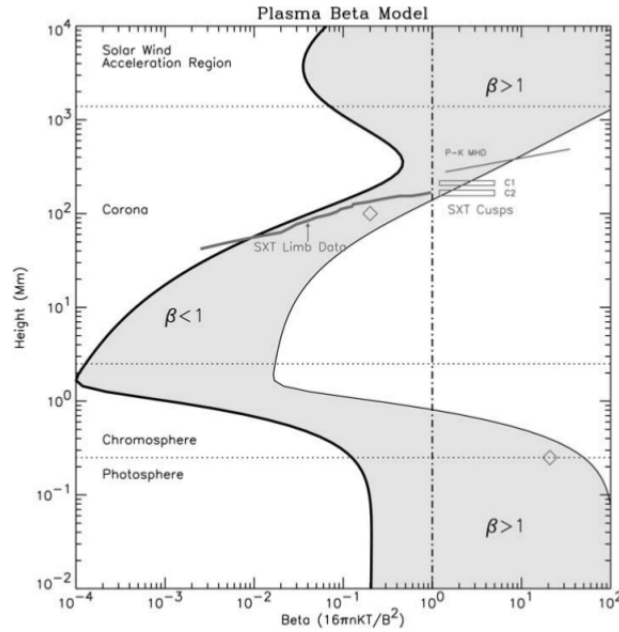


Figure 2.2: Plot of the behavior of β , Equation (2.1) over AR. The plot shows the β -values above an AR in function of the height from the photosphere to solar wind (c.f., Gary 2001). In the left side, the black thick line indicates the model for a sunspot with $B \approx 2500$ G (Gauss), while the black thin line in the right side represents the plage region in the chromosphere with $B \approx 100$ G. Source: Gary (2001).

Kivelson and Russell 1995).

Both types of geometry of the coronal magnetic field, i.e., closed and open, define the source of the SW. The slow SW have the origin in regions with closed magnetic field lines, while the fast SW in the opened magnetic field regions. Both can be described by the mass and momentum conservation laws. The slow SW at solar minimum is localized in the solar equator while at solar maximum it can originate in all latitudes. The fast SW has its origin in the coronal holes (CHs) in the polar regions during the solar minimum while in the solar maximum can occur from the CH present in others latitudes. Figure 2.3 shows the SW speed variations through latitudes at solar minimum (left) and maximum (right) corresponding to the first orbits of Ulysses spacecraft. For the solar minimum condition, the figure shows the fast and slow SW in the polar and equatorial regions. In contrast at the solar maximum conditions the coronal streamers extend for all latitudes. Near to $40 R_{\odot}$ the SW speed can be approximated to 400 km s^{-1} for the slow SW (e.g., Chen, 1996), and 750 km s^{-1} for the fast SW (e.g., Stakhiv et al., 2015). The electrons temperature for both SW are comparable, while the proton temperatures for the fast SW is higher than for the slow SW. In the fast SW, the density of protons is stable while in the slow SW the proton density varies drastically. It is useful for known information about the SW sources.

The temperature in the slow SW varies substantially, and for the fast SW is stable. The high conductivity properties of the SW, allow that magnetic field freeze, and with solar rotation the magnetic field is deformed in a spiral forming the Parker Spiral (Parker, 1958). At Earth distances (1 AU equivalent to $\sim 215 R_{\odot}$) the Parker spiral preserve an angle near of 45° .

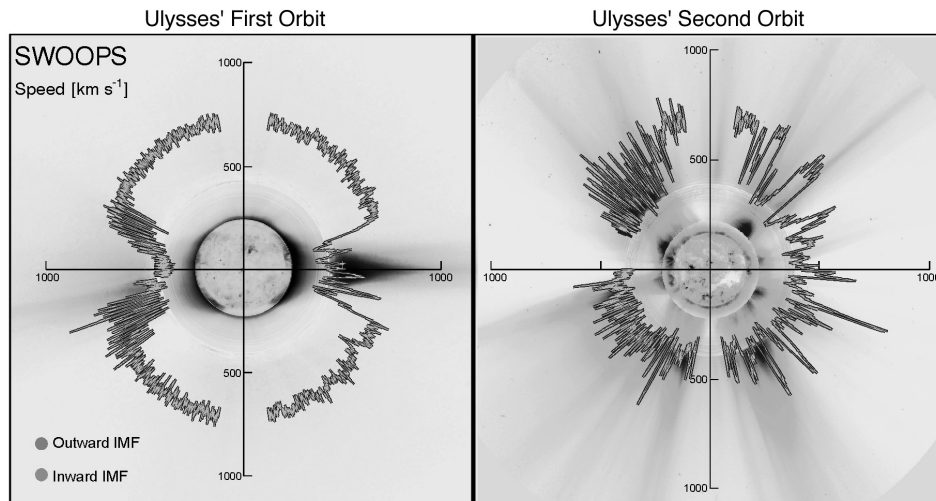


Figure 2.3: Observation of the SW speed from Ulysses spacecraft during the two first orbits. On the left the observation in the solar minimum, and at right solar maximum. Source: McComas et al. (2003).

2.4 Coronal mass ejections

On 1971 December 14 was discovered the first CME through the coronagraph of the Orbiting Solar Observatory (OSO-7) (Tousey, 1973). This approximately one hundred years later than the first observation of solar flares in the 1859 year (Carrington, 1859). The CMEs are known as an observable change in the coronal structure (e.g., Hundhausen et al., 1984). They are large-scale explosions of plasma that inject large quantities of mass and magnetic flux into the heliosphere. The CMEs propagating in the interplanetary space interact with the planets, where inducing interesting phenomena as the auroras in the magnetized planets and ionospheres in the non-magnetized planets. Their propagation is defined by the aerodynamic drag with the SW (e.g., Cargill, 2004; Borgazzi et al., 2009; Vršnak et al., 2010), shock dynamics and deflections (e.g., Kay et al., 2013). The number of the CMEs change through the solar cycle. In the solar minimum, the CMEs are ejected near to the equator region, while in the solar maximum are ejected through all latitudes (e.g., Yashiro et al., 2004). The currently detection of the CMEs have been allowed the

wider construction of catalogs as [LASCO CME catalog](#)⁷ and the [CACTUS catalog](#)⁸ with CME information from 1996 January, 1 at 00:14:26 to current data.

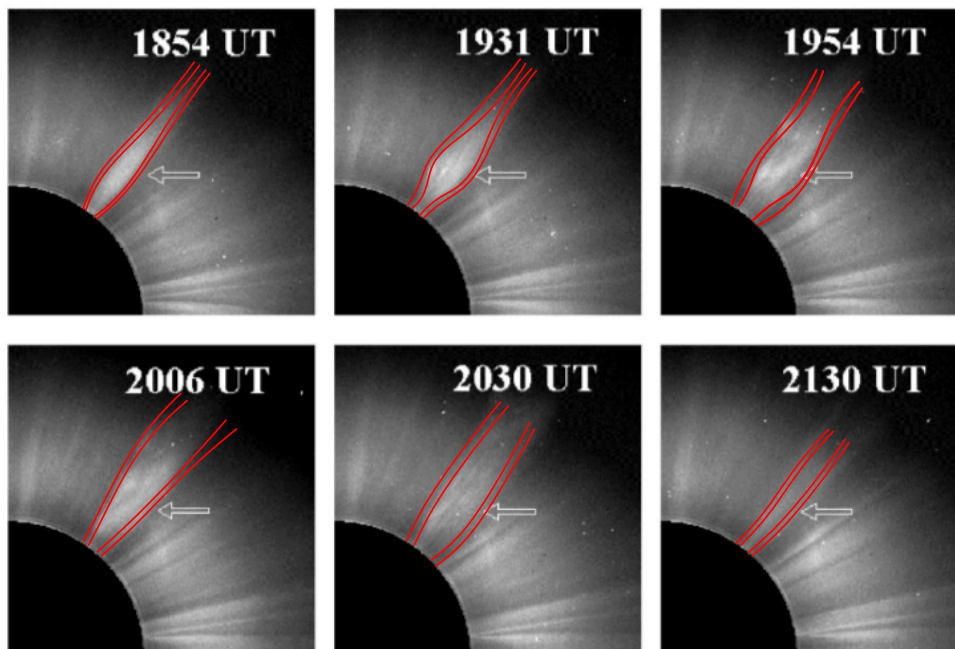


Figure 2.4: Image of the narrow CME of [Gilbert et al. \(2001\)](#). The authors show the evolution of a narrow CME by images from LASCO C2 on 1999 April 24. We highlight the magnetic field jet-like structure through the red lines. Source: [Gilbert et al. \(2001\)](#).

The irregular and complex nature of the CMEs allow some variations in their morphology, but it can be structured in two types: the narrow and the normal CMEs. The first are jet-like explosions, with angular width of $< 15^\circ$, in regions with open magnetic field lines (e.g., [Gilbert et al., 2001](#); [Wang et al., 1998](#)). In Figure 2.4 we show the LASCO/C2 images of the narrow CMEs that occurred on 1999 April 24 analyzed in [Gilbert et al. \(2001\)](#). In this work, the authors show the evolution of the narrow CME. We highlight the magnetic field jet-like structure through the red lines. The second type of morphology is the normal CMEs (hereafter CMEs). This type presents the cone-like shape that is structured into three parts: core, cavity and frontal loop (e.g., [Illing and Hundhausen, 1985](#)). The normal CMEs on average show an angular width of $< 120^\circ$ (e.g., [Yashiro et al., 2004](#)). In Figure 2.5 we show the evolution of CME event of the 1999 June 11 between 11:06 UT⁹ to 12:50 UT observed by the LASCO/C2 ([Brueckner et al., 1995](#)). For the CME we show the three-part structure: core, cavity, and frontal loop, together with shock and sheath.

⁷ <https://cdaw.gsfc.nasa.gov/>

⁸ <http://sidc.oma.be/cactus/>

⁹ UT:universal Time sometime Greenwich Mean Time (GMT)

Particularly, [Bemporad and Mancuso \(2011\)](#) and [Bemporad et al. \(2014\)](#) driven full set of plasma physical parameters in shock from ultraviolet and white-light coronagraphic data.

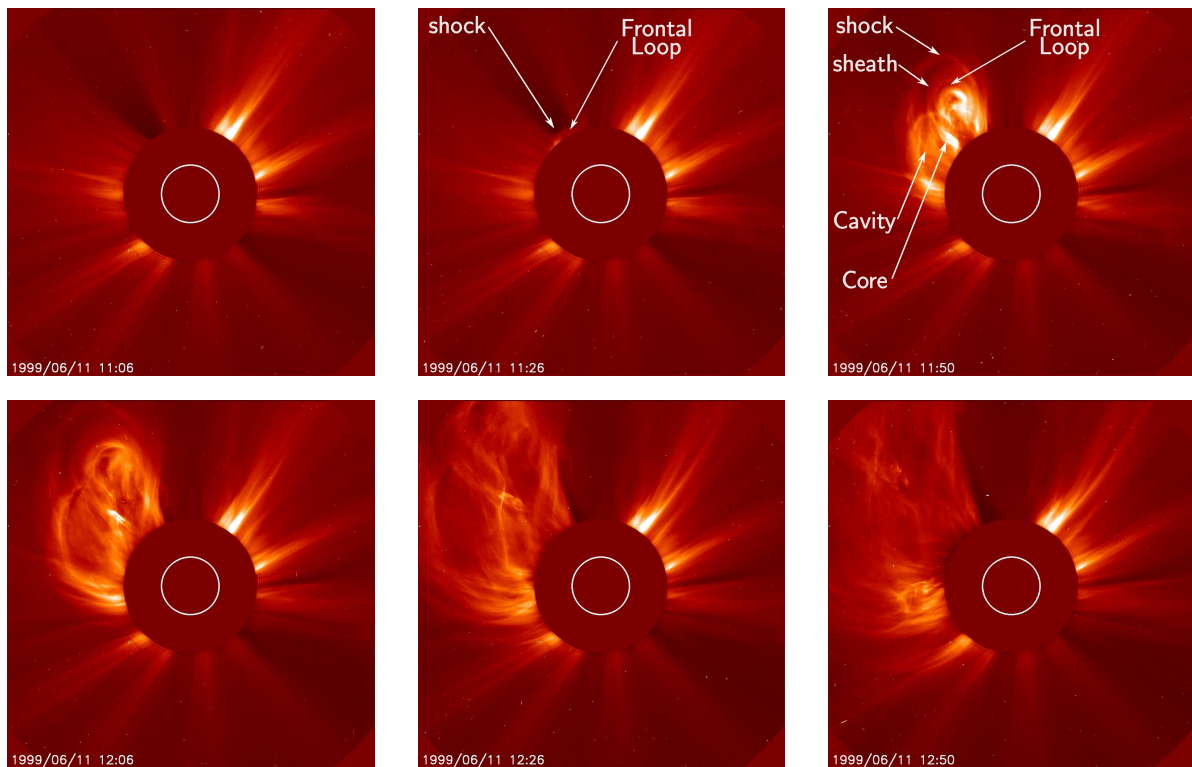


Figure 2.5: The time step of the CME of 1999 June 11 between 11:06 UT to 12:06 UT from LASCO/C2 ([Brueckner et al., 1995](#)). Snapshots illustrate the CME evolution in distances from 2.0 to 6.0 R_{\odot} between 11:05 to 12:50 UT. For the CME we show the three-part structure: core, cavity, and frontal loop, together with shock and sheath. Particularly, [Bemporad and Mancuso \(2011\)](#) and [Bemporad et al. \(2014\)](#) driven full set of plasma physical parameters in shock from ultraviolet and white-light coronagraphic data.

During the CME evolution, they interact with the slow and fast SW and with the solar corona structures as CHs, coronal streamers, quiet Sun, even others CMEs. Thus, the expansion, propagation, deflection, rotation, and magnetic reconnection of the CMEs is the result of the interaction with these structures in the range from its formation to propagation in the larger distances e.g., in ~ 5.4 AU (e.g., [Liu et al., 2005](#)). The expansion of the CMEs is characterized by self-similar expansion or of constant angular width. This behavior is due to that expansion evolve according to the distance of propagation. This makes that CMEs frequently are modeled by cone-model (e.g., [Xie et al., 2004](#); [Mays et al., 2015](#); [Na et al., 2017](#)), and generally this behavior can be assumed for distances above of $5 R_{\odot}$ (e.g., [Chen, 1996](#); [Chen et al., 1997](#)). In lower distances the CME expansion is faster than self-similar expansion (e.g., [Cremades and Bothmer, 2004](#)).

The radial propagation of the CMEs has been studied through coronagraphs observa-

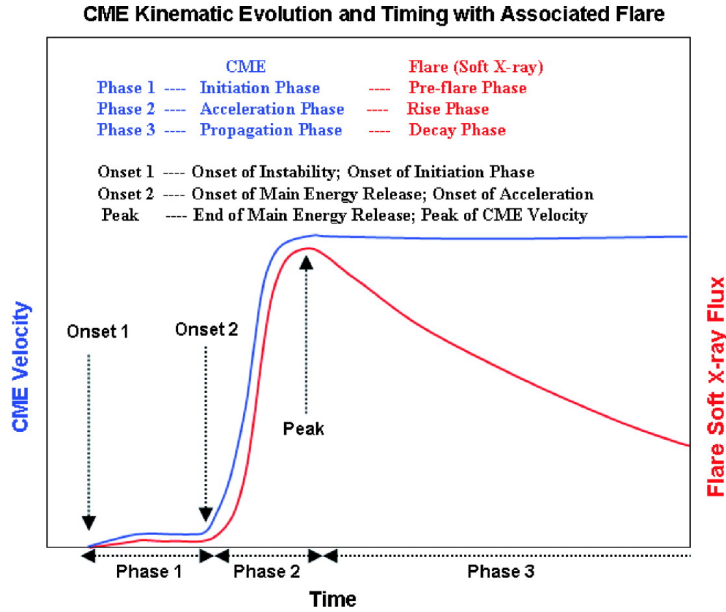


Figure 2.6: Schematic plot proposed in Zhang and Dere (2006) for the CME kinematic. The author emphasized in three dynamical phases: initiation, acceleration, and propagation, related to the flare phases of preflare, rise, and decay of the associated flare, respectively. Source: Zhang and Dere (2006).

tions. This motion is considered in three dynamical phases: initiation, acceleration, and propagation (Zhang et al., 2001, 2004; Zhang and Dere, 2006). The two initial phases are linked to the formation and acceleration of the eject in the low corona, while the third phase is related to the residual acceleration during eject propagation in the interplanetary space.

The CME initiation phase can be interpreted as a sequence of equilibrium states. Its duration is of some hours, here the CME shows a slow increase with constant velocity in the interval 1 to 100 km s⁻¹ (e.g., Zhang and Dere 2006 and references therein). The initiation phase coincides with the onset of the flare (Zhang et al., 2001). Figure 2.6 illustrates the CME kinematic in the three temporal phases associated to evolution of the flare proposed by Zhang and Dere (2006). The authors propose slow-rise initiation phase, an impulsive acceleration phase, and the last phase with a residual acceleration of the CME propagating in the SW.

The acceleration phase of the CMEs is of particular interest in the solar physics. This phase involves or is complementary with relevant phenomena as flare and shock formation, consequently with particle acceleration. The CME acceleration phase starts with the catastrophic loss of equilibrium of the eject (e.g., Forbes, 2000; Lin, 2004). In this spatial and temporal range, the CME increases its velocity suddenly, for this reason, is interpreted

as impulsive acceleration. [Maričić et al. \(2007\)](#) through statistical analysis of 22 CMEs between pre-eruption to the propagation phase, the authors conclude that in the majority of the events the acceleration phase starts before the soft X-ray (SXR) burst and its duration is larger than SXR burst. The CME initiation phase begin some tens minutes before the flare onset, while the CME acceleration starts quasi-simultaneously with the flare onset time ([Zhang et al., 2001](#)). [Vršnak et al. \(2007\)](#), with a temporal and spatial study of CME acceleration phase, show that the peak of acceleration is inversely proportional to the duration and the height range involved. In contrast is proportional to the source region dimensions, if the CME source region is compact, the acceleration is more impulsive.

In the last phase, the CME suffers the second acceleration or residual acceleration. During this phase the CME interacts with the SW, where the aerodynamic drag force is established (e.g., [Chen, 1996](#); [Cargill, 2004](#); [Borgazzi et al., 2009](#); [Tappin, 2006](#); [Vršnak et al., 2010](#)). The relative constant velocity of the CME in the outer corona indicates that acceleration of CMEs occurs in the inner corona, thus the acceleration residual occurs after main acceleration. A statistical study of [Zhang and Dere \(2006\)](#) estimate the main acceleration average in 330.9 m s^{-2} in the low corona, while residual acceleration of 0.9 m s^{-2} in the outer solar corona.

Due to the magnetic and pressure gradients in the solar corona and in the interplanetary space the CMEs can be deflected from their radial propagation. The CME deflection is a known problem that has been discussed since early CME observations (e.g., [MacQueen et al., 1986](#)). From the initial studies of the deflection, it was understood as a consequence of the fast SW. [Gopalswamy et al. \(2009\)](#) and [Gopalswamy et al. \(2010\)](#), quantified the CH influence on CME propagation. The authors affirm that CH pushes the CMEs toward the solar equator region (e.g., [Cremades and Bothmer, 2004](#); [Kilpua et al., 2009](#)). In complementary way, some studies indicate that slow and fast CMEs are deflected of different manners. The first, toward the solar equator, and the second away the streamer belt (SB) (e.g., [Xie et al., 2009](#)). [Shen et al. \(2011\)](#) and [Gui et al. \(2011\)](#), show that the density of background magnetic energy in the solar corona induce the CMEs deflection toward the streamer region in distances $\geq 1.5 R_{\odot}$. The CME deflection can occur in latitude and longitude, [Isavnin et al. \(2013\)](#) with observations found the latitudinal deflection up to 35° and a maximum longitudinal deflection of 5.4° , while [Lugaz et al. \(2011\)](#) by MHD simulation for the event of 2005 August 22, found that magnetic forces drive a deflection

of 10° to 15° within $8 R_\odot$, lower than the observational values.

Recently, [Kay et al. \(2013\)](#) constructed the model ForeCAT (forecasting a CME's Altered Trajectory) in order to understand how the magnetic forces i.e., magnetic pressure gradients and magnetic tension define the CME deflection. The authors include the CME expansion, three-part model propagation, and effect of the drag force, their model, ForeCAT, is susceptible to the mass, velocity in the propagation phase, initial radius and initial magnetic field strength. [Kay et al. \(2015\)](#) using ForeCAT compare simulations with observations of the CME deflection of the event 2008 December 12, they show the model efficiency to predict the CME deflection with their model. Few years ago, [Kay and Opher \(2015\)](#) show that CME deflection and rotation are established beyond $2 R_\odot$.

2.5 Shock waves

The MHD shock waves occurs in astrophysical environments from smaller scales, as the bow shock in the magnetosphere (e.g., [Kivelson and Russell, 1995](#)), to larger scales, as in galaxy cluster (e.g., [Markevitch et al., 2002](#)). The shock can manifest as non-relativistic, such as in space plasma, supernova remnants, galaxy clusters, and relativistic for the active galactic nuclei, gamma-ray bursts. The shock waves are formed in super-Alfvénic or super-magnetosonic plasmas. The first occurs in plasmas with velocity, V , larger than Alfvén velocity $V_A = B/\sqrt{\mu_0\rho}$, i.e., when the Alfvénic Mach number $M_A = V/V_A > 1$. The second take place in plasmas with Mach number $M_{ms} = V/c_{ms} > 1$, when the plasma velocity is larger than magneto-sonic velocity $c_{ms} = \sqrt{V_A^2 + c_s^2}$, where c_s is the sound velocity.

Figure 2.7 illustrates the shock wave (orange line) when the driver propagates with $M_A > 1$ the upstream (pre-shock) and downstream (post-shock) regions are established. We distinguish these two regions by subscript 1 and 2, respectively, in their densities (ρ), magnetic fields (blue arrows, \mathbf{B}), velocities (\mathbf{V}), and angle (θ). The set of equations that control the jump through the shock are called the Rankine–Hugoniot (RH) conditions (e.g., [Balogh and Treumann, 2013](#)). These equations allow to describe the downstream in function quantities of the upstream, together with the temperature and pressure. The most important parameters that control the shock physics are the Mach number M_A , and the shock normal angle, θ_{Bn} . The M_A represent the strength of the shock and quantify energy processed in the shock, while θ_{Bn} represents the angle between the upstream magnetic

field and the shock normal. The shock orientation can be parallel, $\theta_{\text{Bn}} = 0$, quasi-parallel, $0 \leq \theta_{\text{Bn}} \leq \pi/4$, quasi-perpendicular ($\pi/4 \leq \theta_{\text{Bn}} \leq \pi/2$) or perpendicular ($\theta_{\text{Bn}} = \pi/2$). Depending on θ_{Bn} exist different physical behavior, the quasi-parallel regions are associated with the turbulence regions, and the quasi-perpendicular regions are associated to the acceleration of particles.

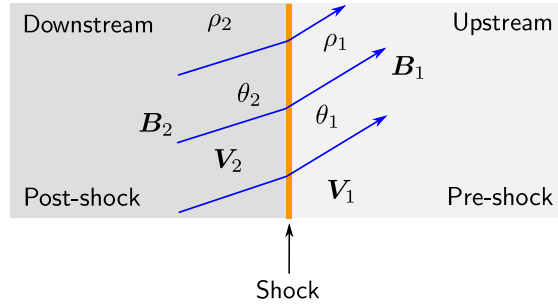


Figure 2.7: The shock wave formation (orange line) allow that the downstream (post-shock) and upstream (pre-shock) regions to be established. The subscript 1 and 2 in density (ρ), magnetic field (blue arrows, \mathbf{B}), velocity (\mathbf{V}), and angle (θ), we identify the downstream and the upstream region quantities, respectively.

Figure 2.8 shows the two types of the shock formation. In panel (a) we illustrate the CME piston during its impulsive expansion and acceleration phase, where occurs the shock formation, and the sheath structure (green shadow) by SW compression. In the initial range, the piston accelerates rapidly controlling the shock kinematics, but for incoming distances the eject decelerate and the shock continues propagating. In panel (b) we indicate the bow shock, where the stand-off distance to the driver is constant and the piston and the shock maintain the same velocity. We present the bow shock (blue line) that occurs when the SW arrived at the magnetosphere. In a similar way to the panel (a), here originates the magnetosheath (green shadow) between the magnetopause (orange line) and the shock. The CME and magnetosphere are shock examples, but exist others examples in astrophysics as the supernova shock, comets, among others.

In space plasma, the shocks can be interpreted as collisionless shocks. In this shock type, the magnetic field allows a behavior equivalent to the collision shocks through the interaction of waves with the particles. A collisionless shock wave is defined as “irreversible (entropy-increasing) wave that causes a transition from supersonic to subsonic flow” (Kivelson and Russell, 1995). The dissipation in shocks corresponds to the change between the kinetic energy of the flow into the thermal energy of the particles. The collisionless shocks are characterized by dissipation and thermalization process caused by the viscosity

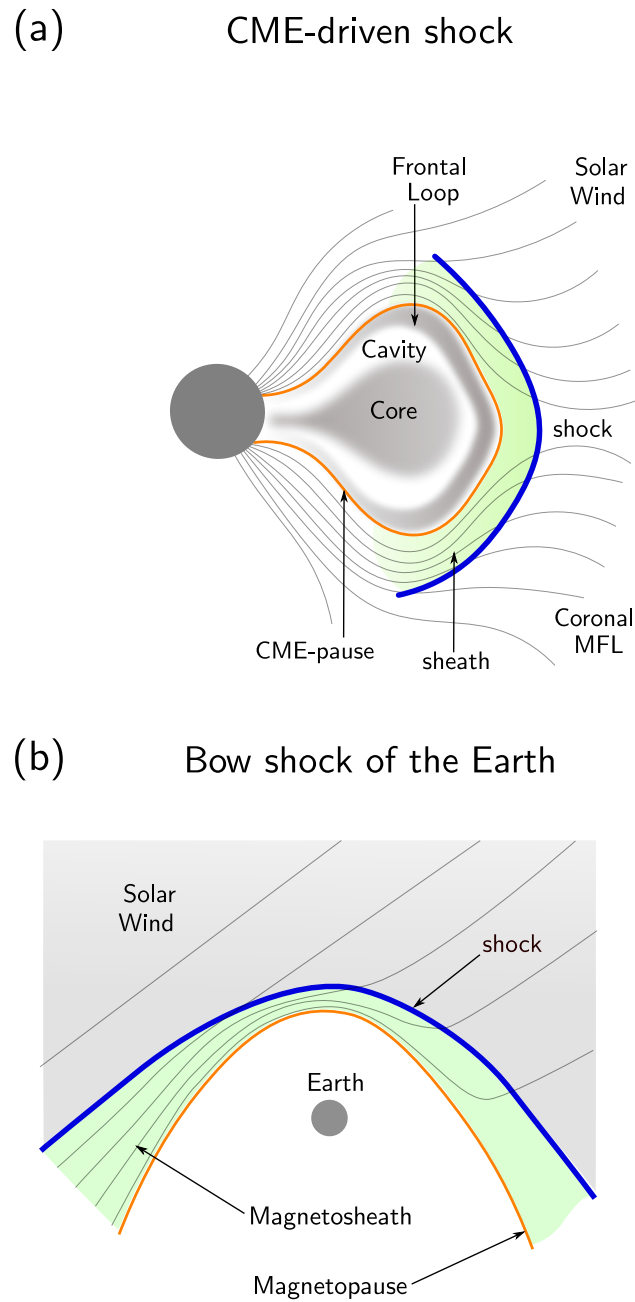


Figure 2.8: Schematic view of the two shocks types. In panel (a) we show the shock originated in the condition that driver propagate in the plasma. We indicate the faster CME propagating in the equator region with a shock wave (blue line) in CME nose region. We highlight the CME three parts structure region i.e., core, cavity, and frontal loop, CME-pause (orange line), the sheath region (green shadow) behind the shock, coronal magnetic field lines (MFL, gray lines). In panel (b), we illustrate the bow shock (blue line) that occurs when there is the SW collision between SW with the magnetosphere. In this case, the stand-off distance to the driver is constant and the piston and the shock maintain the same velocity. In a similar way to the panel (a), here originates the magnetosheath (green shadow) between magnetopause (orange line) and shock.

and anomalous resistivity. These two are due to the change velocity in the particles by the perturbations in the fields. Thus, the waves in the fields replace the collisions between particles, and the collisionless plasma can be interpreted as collisional. The turbulence in the plasma, from waves-particle interaction, allow the increase of the kinetic temperature and also provide the source of free energy to complete the dissipation process.

In shocks with low Mach number, M , the dissipation process is caused by the heating that suffer the shock and the Joule heating, ηJ^2 , where η is the resistivity and the J is the current density. While in shocks with higher M , the ion reflection become important and provide the shock dissipation. This is the clearest difference between subcritical (low M) and supercritical (high M) shocks, the first associated to the Joule heating, and the second to the particle acceleration. However, the ion reflections can be found in shocks with low Mach and Joule heating in shocks with high Mach, but with reduced relative importance without developing a role in the shock structure (Kivelson and Russell, 1995). thus, the particle acceleration is an important process in supercritical shocks, because is the only processes that compensate the dissipative process in the shock.

In super-Alfvénic CMEs ($> 800 \text{ km s}^{-1}$) the shock and sheath are generated ahead of and behind of the ejecta, see Figure 2.8(a). Some CME parameters are relevant for the shock formation as the velocity, the duration of the acceleration phase, and the Alfvén velocity (e.g., Žic et al., 2008). Complementary to the CME properties, the presence of a flare during the CME acceleration may optimize the conditions for the shock formation, an example is explained by Magdaleníć et al. (2010). In this study the authors show the shock wave formation in slow CME ($< 500 \text{ km s}^{-1}$) by the flare associate to the ejecta. They explain that the shock occurs due to the flare pressure, besides the shock is temporally associated with the release of energy of the flare. Complementary works also show that shock can be consequence of flare and CME (e.g., Magdaleníć et al., 2008; Oh et al., 2007; Reiner et al., 2001; Vršnak and Cliver, 2008). As mentioned above, the understanding of shock phenomenon can be confusing due to the synchronization of the CME acceleration phase and the flare energy release (e.g., Zhang et al., 2001).

2.6 Solar energetic particles (SEPs)

Since the first report of solar energetic particles (SEPs) (Forbush, 1946), that occurred approximately 87 years after first white-light solar flare observation on 1 September on 1859 by Carrington, the SEPs has been associated with the eruptive events i.e., flares and CMEs. The different physical process between these last phenomena defines two different mechanisms of SEPs acceleration, and consequently two SEPs types: the impulsive and the gradual. The first are associated to the magnetic reconnection present in flares, while the second are associated to the shock waves driven by CMEs (Reames, 1999). The impulsive and gradual denomination is not related to the duration of these SEPs. Figure 2.9 illustrates in the left the gradual SEPs (helical blue lines) associated with CME shocks (thick blue line) in the corona and interplanetary (IP) space, and in the right, the impulsive SEPs linked to the flares. The SEPs basically are proton, electrons, He and Pb, (e.g., Reames, 1995; Reames and Ng, 2004). The composition and abundance of the elements and isotopes turn relevant in order to interpret the origin, the acceleration process in the sources, or even the process of transport involved.

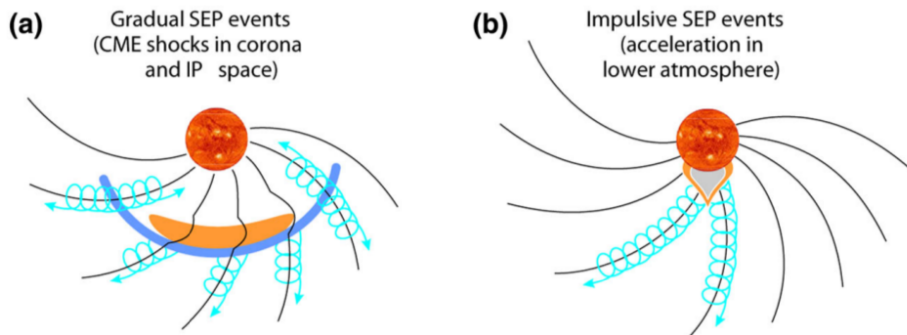


Figure 2.9: Schematic of mechanism of SEPs acceleration that define the SEPs types. Panel (a) shows the gradual SEPs accelerated in the shock waves driven by CMEs While panel (b) shows the impulsive SEPs associated to the open magnetic field lines that are accelerated in the magnetic reconnection process present in the flare. Source: Reames (1999).

The large events of gradual SEPs have been associated to CMEs with velocity of ~ 1500 km s^{-1} and with some exceptions to ~ 800 km s^{-1} (e.g., Kahler, 2001). Some additional CME constraints are the mass and kinetic energy larger than 10^{15} g and 3×10^{31} ergs, respectively (e.g., Yurchyshyn et al., 2005). These fast and wide CMEs can be linked to secondary CME in the same active region (e.g., Liu et al., 2009). In these events, the first CME may optimize the surrounding environment in order to the secondary CME to be more efficient to accelerate particles, or the physical process is optimized for accelerate particles.

Some of them (c.f., [Desai and Giacalone 2016](#)), (i) the initial CME may pre-accelerate the particles, i.e., proportionate seed particles, or even allow enhance the turbulence of medium to the secondary CME may be efficient (e.g., [Li and Zank, 2005](#); [Ding et al., 2013](#)); (ii) in the same way, the first CME-driven shock may proportionate an initial acceleration, in order to the second CME-driven shock re-accelerate these particles ([Gopalswamy et al., 2004](#); [Mewaldt et al., 2012](#)); (iii) during the CME origin the pseudo streamer leads to the reconnection between closed field lines that drape the CME and its shock, as well, as the open field lines that drape the second CME, creating enhanced seed populations and higher turbulence levels in front of the second CME shock (e.g., [Li et al., 2012](#)); (v) the previous reconnection process between open and closed lines decrease the Alfvén velocity creating a stronger shock in front of the second CME (e.g., [Gopalswamy et al., 2004](#)).

Part I:

Kelvin–Helmholtz instability
at CME–Sheath and Sheath–Solar Wind
interfaces

Kelvin–Helmholtz Instability (KHI) in coronal mass ejections

The instabilities are common phenomena in fluids and plasmas. They represent the transfer of energy and play an important role in the origin of turbulence, and plasma heating (e.g., [Karpen et al., 1994](#)). In the astrophysical researches, the Kelvin–Helmholtz instability (KHI) has been of regular detection. Particularly, the KHI is of great interest in the space plasma, and it was detected in the SW, CMEs, and magnetosphere. In this Chapter, we present a summary of the state of the art of KHI studies in the CME environments. We summarize the relevant findings of the observations and analytical models previous to our work, which we will present in the next Chapter.

3.1 Introduction

The KHI is a hydrodynamical (HD) and magnetohydrodynamical (MHD) phenomenon that occurs in different scales in nature. The conditions for magnetic KHI formation are the shear velocity at the interfaces of one, or at boundary layer between two plasmas (e.g., [Chandrasekhar, 1961](#); [Hasegawa, 1975](#)). In the magnetic medium, the tension of the magnetic field lines can stabilize the interface and affect the KHI formation or its growth rate, even inhibit its formation. When the shear flow and the magnetic field are parallel the instability can be suppressed, while in the case where they are perpendiculars the situation is equivalent to the HD case.

The KHI evolve in two phases. The first phase is known as the linear phase, where the KHI vortices show growth with an exponential rate powered by the kinetic energy of shear flow. The second phase is the non-linear stage where the KHI allow the formation

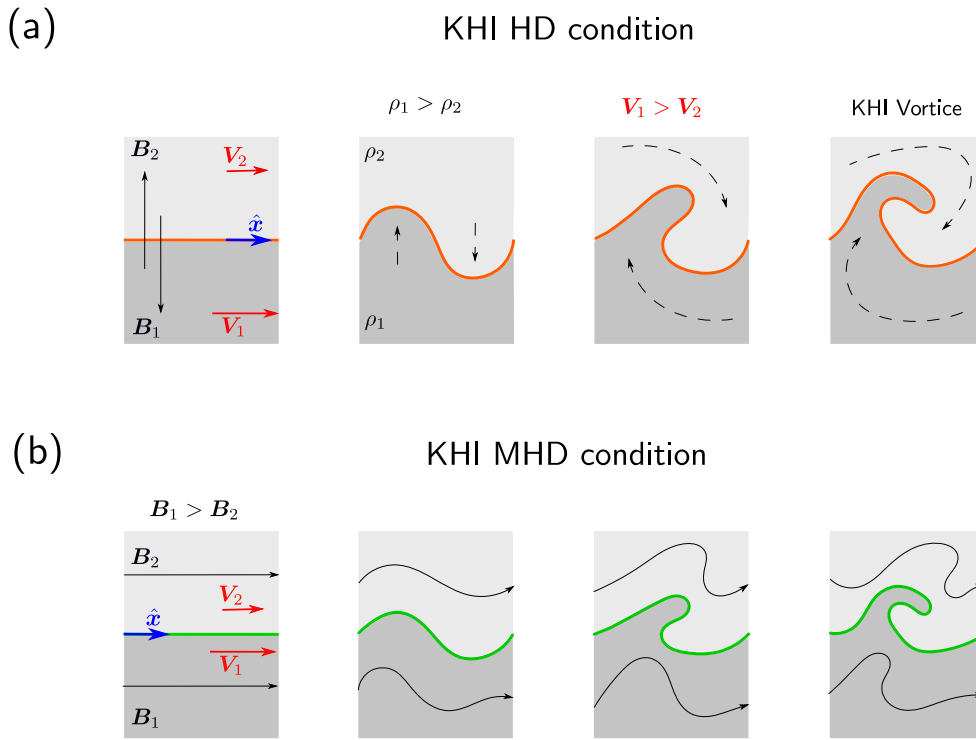


Figure 3.1: Schematic of the linear phase of the KHI between two plasmas indicated by subscripts 1 (higher gray shadow) and 2 (light gray shadow). Panel (a) indicates the hydrodynamical conditions of the KHI where the magnetic field \mathbf{B} is perpendicular to the shear flow \hat{x} (blue arrow) at the interface between fluids (orange line). The KHI vortices formation is indicated by the black dashed arrows. For two plasmas we consider: $V_1 > V_2$, $\rho_1 > \rho_2$, and $B_1 > B_2$, in order to illustrate the interface CME and SW. In panel (b), we present the MHD KHI case with the \mathbf{B} (black arrows) parallel to \hat{x} in the interface (green line). The KHI vortices size are shown larger in the HD case than in the MHD case, in order to emphasize the role of the magnetic field tension opposing to the KHI origin.

of a turbulent flow due to the saturation of the vortices and the transport of energy to smaller scales.

Figure 3.1 illustrates the linear KHI phase for two plasmas identified with the subscripts 1 and 2, with densities (ρ_1 , ρ_2 , with $\rho_1 > \rho_2$), magnetic fields (B_1 , B_2 , with $B_1 > B_2$, black arrows), and velocities (V_1 , V_2 , with $V_1 > V_2$, red arrows). Panel (a) indicates the magnetic field \mathbf{B} , perpendicular to the shear flow, \hat{x} (blue arrow) at the interface between fluids (orange line), this situation is equivalent to the HD case. In panel (b), we present the MHD KHI case, with the \mathbf{B} parallel to \hat{x} in the interface (green line). The KHI vortices formation is indicated by the black dashed arrows. The KHI vortices size are shown larger in the HD case than in the MHD case, in order to emphasize the role of the magnetic field tension opposing to the KHI evolution.

For the configuration shown in Figure 3.1, Chandrasekhar (1961) and Hasegawa (1975)

found the mathematical condition for the KHI formation. Their mathematical method is applied for a streaming flow (\mathbf{V}) along the interface between fluids ($\hat{\mathbf{x}}$), and parallel to the magnetic field (\mathbf{B}). Linearizing the MHD equations of continuity, motion and induction through the perturbations on quantities, i.e., $\mathbf{V} = \mathbf{V}_0 + \mathbf{v}$, $\rho = \rho_0 + \delta\rho$, $p = p_0 + \delta p$, and $\mathbf{B} = \mathbf{B}_0 + \mathbf{b}$, with the subscript 0 as the equilibrium, are considered solutions in normal modes, $\exp i(\mathbf{k} \cdot \mathbf{x} + nt)$. Calculating the dispersion relation n is finding the KHI condition, here shown for two fluid identified with subscripts 1 and 2,

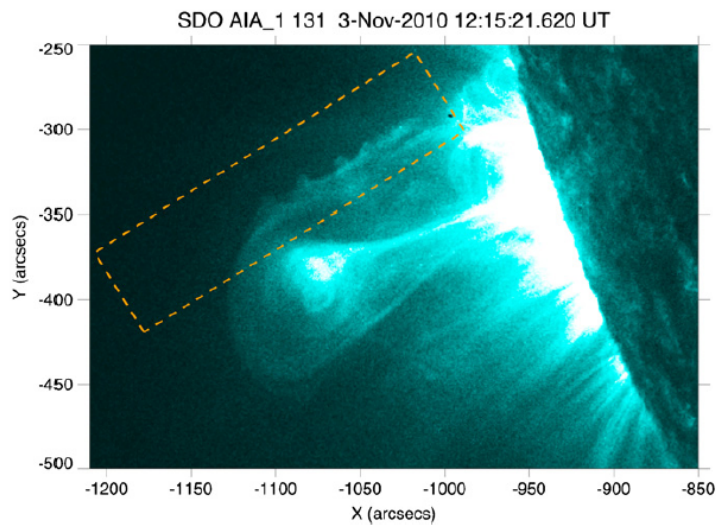
$$\left[\hat{\mathbf{k}} \cdot (\mathbf{V}_1 - \mathbf{V}_2) \right]^2 > \frac{\rho_1 + \rho_2}{\mu_0 \rho_1 \rho_2} \left[(\hat{\mathbf{k}} \cdot \mathbf{B}_1)^2 + (\hat{\mathbf{k}} \cdot \mathbf{B}_2)^2 \right]. \quad (3.1)$$

The condition (3.1) suggest some properties of the instability, e.g., that the KHI is consequence of a relative streaming $|\mathbf{V}_1 - \mathbf{V}_2|$ along the discontinuity between the fluids, and for traversal configuration the KHI react like a situation without magnetic field.

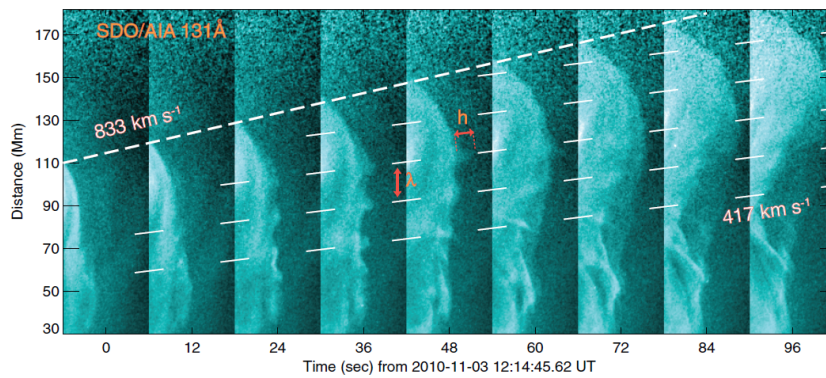
The KHI play an important role in the transport of energy and mass, and due to it the instability is an ubiquitous phenomenon in astrophysical plasmas. The KHI was detected in: stellar jets (Micono et al., 1998), nova explosions (Casanova et al., 2011), in the Orion molecular cloud (e.g., Berné et al., 2010) where was interpreted like turbulence and chemical mixing in the interstellar medium (e.g., Berné and Matsumoto, 2012), planetary environments (Hasegawa et al., 2004; Amerstorfer et al., 2007; Sundberg et al., 2010), magnetopause (Kivelson and Pu, 1984), and magnetosphere e.g., in Mercury (Slavin et al., 2010), and Saturn (Masters et al., 2010). In the solar corona, the KHI observations are focused on the coronal streamers (e.g., Feng et al., 2013), in twisted magnetic flux tubes in the solar wind (e.g., Zaqarashvili et al., 2014).

3.2 KHI in coronal mass ejections

In CME environments the KHI has been observed in three opportunities: 2010 November 3 (Foullon et al., 2011), 2010 April 8 (Ofman and Thompson, 2011), and on 2011 February 24 (Möstl et al., 2013). These events have been analyzed by complementary works, through analytical and computational models. The first detection on the ejecta of 2010 November 3, besides of clear KHI formation presents others features as, a flux rope structure from the impulsive acceleration phase of the CME (Cheng et al., 2011), shock formation together with electron acceleration suggested by type II radio burst observations



(a) The KHI vortices on the northern flank of CME of 2010 november 3.



(b) The illustrative images show the KHI evolution through the time and distance. Each one image is taken each 12 seconds.

Figure 3.2: First KHI observations in the CME environments. The image was observed in the AIA/SDO 131\AA (Fe XX). The X and Y (both in arcsecs) are orientated for the west and north, respectively. Source: [Foullon et al. \(2011\)](#).

(Bain et al., 2012), and flare-CME initiation (Mulay et al., 2014). Figure 3.2 shows the KHI observations analyzed by Foullon et al. (2011). Panel (a) shows the KHI formation in the superior flank of the CME. The images were acquired in the highest temperature channel 131Å (Fe XX) EUV bandpass at 11×10^6 K of the Atmospheric Imaging Assembly (AIA) on board SDO. In a similar panel (b) represent the image with which the authors evidence the evolution of the KHI along the CME flank. They show the sequence of snapshots of the KHI such as 12 seconds, these substructures or vortices maintain a separation of $\lambda = 18 \pm 0.4$ Mm. Foullon et al. (2011) indicate that vortices move with phase speed of $\sim 417 \pm 7$ km s⁻¹, and period of 43 ± 2 s.

The relevance of the first KHI observations enables new works focused to analyze this phenomenon. Foullon et al. (2013) made a spectral analysis to explore the KHI properties, CME plasma structure, and the surrounding environment in order to corroborate the features observed by Foullon et al. (2011). The authors found that the KHI evolution occurs on 150 Mm (10^3 km) from the solar surface when the shear velocity in CME flanks is ~ 680 km s⁻¹. They present some parameters of the CME and solar corona at KHI region as, electronic temperature $T_e = 11.6 \pm 3.8 \times 10^6$ K, density $n_e = 7.1 \pm 1.6 \times 10^8$ cm⁻³, and for the solar corona $T_e \sim 1 \times 10^6$ K, and density 2 to 1×10^8 cm⁻³ between 40 a 100 Mm or equivalent a 0.05 and 0.15 R_⊙ (Aschwanden and Acton, 2001). An additional study by Nykyri and Foullon (2013) structure an analysis through 2.5D MHD simulations with the CME magnetic field as a parameter. They mimic the KHI of Foullon et al. (2011) finding that a magnetic field of $B_{\text{ejecta}} \approx 8 - 9$ G, and $B_{\text{sheath}} \approx 10 - 11$ G and a shear of $\Delta V \approx 770$ km s⁻¹ may allow the KHI formation. The authors suggest that KHI formation can occur in only one flank due to the helical configuration of the CME structure, contrary to the magnetopause where the KHI is expected on both sides.

Contemporary to the KHI observations on 2010 November 3, Ofman and Thompson (2011) provide others KHI observations in the interface between CME and the solar corona on 2010 April 8. Figure 3.3 presents these observations in the 193 Å (Fe XII) waveband of the AIA/SDO, see the left side in figure. On the right side, the authors show the images of the temporal sequence evolution of KHI in the 211 Å (Fe XIV). They conclude that the vortices preserves ~ 7000 km in size and ~ 6 to 14 km s⁻¹ velocity of propagation from right to left. Finally, they affirm that KHI structures disappear on timescales of tens of minutes. Similarly, Möstl et al. (2013) add others KHI observations occurred in

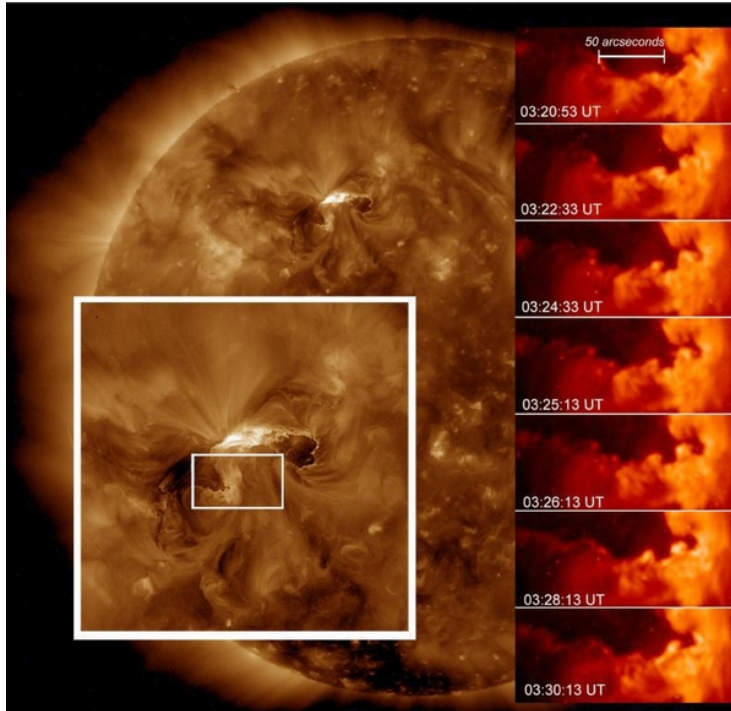
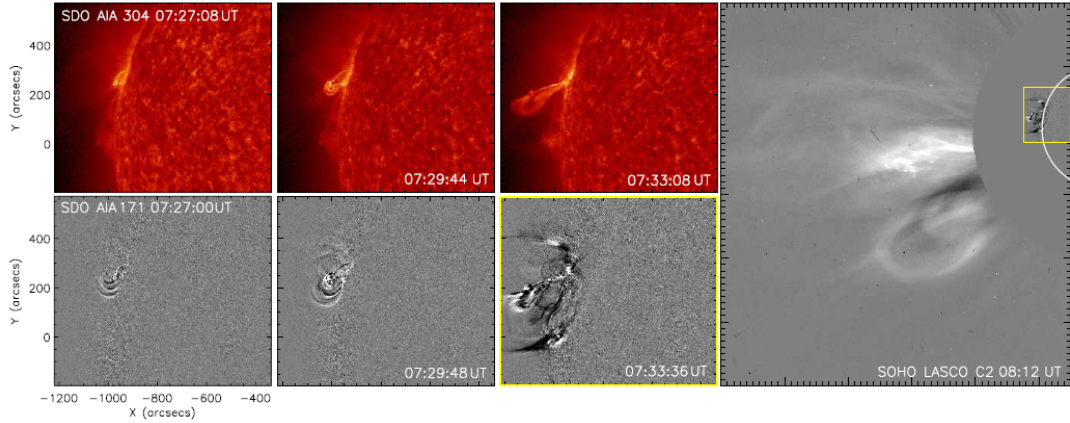
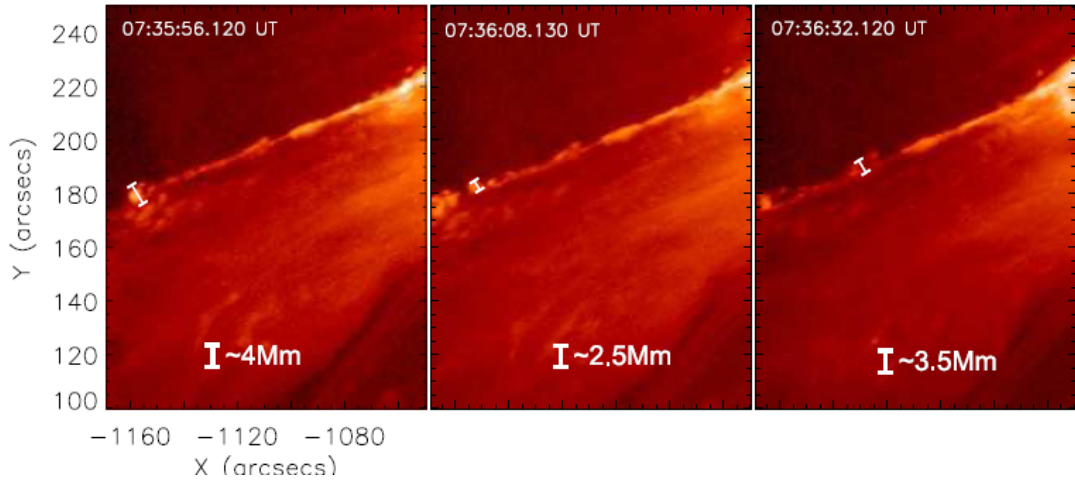


Figure 3.3: CME images of event occurred on 2010 April 8. This image corresponds to 193 \AA (Fe XII). The larger and small boxes correspond to CME and KHI observations, respectively. The columns of the frames in the right side correspond to the temporal evolution of the vortices in 211 \AA (Fe XIV) images. Source: [Ofman and Thompson \(2011\)](#).

the interface CME and solar corona on 2011 February 24. From two flanks of the CME, only the northern evidence the KHI formation as quasi-periodic vortices-like structures. Figure 3.4 shows the observations analyzed in [Möstl et al. \(2013\)](#). In panel (a), they show the AIA/SDO images in the 304 \AA (He II) in $5 \times 10^4 \text{ K}$ (orange images) and in the 171 \AA (Fe IX) in $6 \times 10^5 \text{ K}$ (gray images). The yellow square corresponds to the image 30 minutes before the LASCO observation (see right side). Panel (b), correspond to the zoom into the AIA 304 \AA (He II). The authors calculate the filament velocity as $\sim 470 \text{ km s}^{-1}$, and the height of the structures as 2.4 to 4 Mm, wavelength $\sim 14.4 \text{ Mm}$, and propagation velocity of $\sim 320 \text{ km s}^{-1}$. Complementary to the observations the author through 2.5D MHD simulations find that a parallel magnetic field of 2 G can stabilize the interface and inhibit the evolution of KHI.



(a) AIA/SDO images in 304 Å (He II) and 171 Å (Fe IX) channels. In right side LASCO/SOHO image of the CME.



(b) Boundary between CME and the solar corona. Images AIA/SDO in 304 Å (He II) channel.

Figure 3.4: Observations of the KHI by Möstl et al. (2013). In panel (a) the authors show the AIA/SDO images in 304 Å (He II) channel (orange images). The gray images corresponding to the AIA/SDO observations in 171 Å (Fe IX) channel. Source: Möstl et al. (2013).

The KHI observations mentioned above, have inspired some analytical studies of KHI instability. Zaqarashvili et al. (2010) analyzed the influence of mass flows on the KHI formation in twisted flux tubes. In a complementary way, Zaqarashvili et al. (2014) suggest the KHI formation in a twisted flux tube in the SW. Zaqarashvili et al. (2014) suggest the existence of the twisted flux tubes in the SW from total pressure observed. These twisted flux tubes may lead to KHI formation. Zhelyazkov et al. (2015) present a study of the KHI in a CME in the lower corona, for the conditions of the CME of 2010 November 3. These works analyze the balance of pressure in the twisted flux tube and conclude that KHI exists for some unstable harmonics.

Kelvin–Helmholtz instability at the CME–Sheath and Sheath–Solar Wind interfaces

A few years ago was observed some wave-like features CMEs associated with the presence of Kelvin–Helmholtz instability (KHI) in the low corona distances. As discussed in Chapter 2 in this range of distances the strength of the magnetic field is higher than in the outer corona. Besides, the geometry of the magnetic field lines is more complex and in this interval is where the reconnection process can succeed, together with the acceleration phase of the CME. Given above, we focused in to analyze the existence of the KHI in the kinematic propagation phase where geometry and the strength of the magnetic field is more adequate for the KHI formation. Our analysis study the existence of the KHI at the interface CME–Sheath (CME–Sh) and sheath–solar wind (SW) (Sh–SW) of two CMEs that propagate in the slow and fast SW. In this Chapter, we reproduce our study titled: “Kelvin–Helmholtz Instability at the CME–Sheath, and Sheath–Solar-wind Interfaces” published in [The Astrophysical Journal](#) volume 851 page 112¹, in collaboration with Professor Dr. Diego Falceta-Gonçalves and Professor Dr. Merav Opher ([Páez et al. \(2017\)](#), see Appendix A).

¹ <http://iopscience.iop.org/article/10.3847/1538-4357/aa9753/meta>

4.1 Methodology

The KHI was observed in the low corona distances during the early stages of formation of some CMEs (e.g., [Foullon et al., 2011](#); [Ofman and Thompson, 2011](#); [Möstl et al., 2013](#)). In the present work, we are motivated to discuss the possibility of the KHI formation in the outer corona between heliocentric distances from 4 to 30 R_{\odot} , unlike to previous works. Our study simplifies the large variety of regimes and the multiplicity of configurations of the environment that may affect the KHI. Here we only consider harmonics with the wave vector parallel to the flow that can be stabilized by flow-aligned magnetic field. We adopt the KHI magnetic condition proposed in [Chandrasekhar \(1961\)](#), along the shear flow, $\hat{\mathbf{k}}$, for an incompressible plasma, without viscosity and in a thin layer with an external magnetic field,

$$\left[\hat{\mathbf{k}} \cdot (\mathbf{V}_1 - \mathbf{V}_2) \right]^2 > \frac{\rho_1 + \rho_2}{\mu_0 \rho_1 \rho_2} \left[(\hat{\mathbf{k}} \cdot \mathbf{B}_1)^2 + (\hat{\mathbf{k}} \cdot \mathbf{B}_2)^2 \right], \quad (4.1)$$

where the \mathbf{V} are the velocities, ρ the densities, \mathbf{B} the magnetic field of the two plasma and μ_0 the permeability of free space ($\mu_{\text{solar}} \approx 1$). For this, we assume in the condition (4.1) an electron–proton plasma i.e., $\rho = \rho_e + \rho_p$, with, $\rho_e \approx n_e m_e$, $\rho_p \approx n_p m_p$ and quasi-neutrality MHD, $n_e \approx n_p \approx n$. With this in mind, the Equation (4.1) can be written as

$$\left[\hat{\mathbf{k}} \cdot (\mathbf{V}_1 - \mathbf{V}_2) \right]^2 > \frac{n_1 + n_2}{m_p n_1 n_2} \left[(\hat{\mathbf{k}} \cdot \mathbf{B}_1)^2 + (\hat{\mathbf{k}} \cdot \mathbf{B}_2)^2 \right]. \quad (4.2)$$

In order to study the condition (4.2) at the interfaces CME–Sh and Sh–SW, we model the velocities, densities, and magnetic field strengths for two CMEs propagating independently in the slow and fast SW during the minimum of the solar cycle. We neglect the CME deflection checking in [Kay et al. \(2013\)](#), the CME rotations considered in [Lynch et al. \(2009\)](#), or twisted magnetic flux tubes ([Zaqarashvili et al., 2010](#)), and effects of reconnection. Simulations in [Evans et al. \(2011\)](#) show how the relative orientations of the CME magnetic field with respect to global magnetic field can generate changes on CME–Pause morphology (here CME–Sh interface) in response to different balances of pressure.

We start analyzing the slow and fast SWs in subsection 4.1.1 and analyzing the CMEs and their sheaths structures in subsections 4.1.2 and 4.1.3, respectively. In Figure 4.1 we present the general scheme of our study at left for CME 1 and on the right for CME 2 environments. Figure 4.1 shows the general scheme of the KHI regions on CME flanks for

CME 1 and CME 2 that propagate in the slow and fast SWs, respectively. Panels (a) and (b) show the helical magnetic structures, $\mathbf{B}_{\text{CME}}^{\text{Helical}}$ of CME 1 and CME 2 evolved by the sheath magnetic field lines $\mathbf{B}_{\text{Sh}}^{\text{Slow}}$ (orange lines) and $B_{\text{Sh}}^{\text{Fast}}$ (green lines), and the magnetic field lines of the SW $\mathbf{B}_{\text{SW}}^{\text{Slow}}$ (purple lines) and fast SW $\mathbf{B}_{\text{SW}}^{\text{Fast}}$ (pink lines). The CME 1 and CME 2 sheaths are represented as the cyan and yellow shaded regions, respectively. We indicate the KHI region by dashed black line rectangle together with the shear flow, $\hat{\mathbf{k}}$, on CME flanks. The solid black point represents the Sun, and the solar rotation is assumed in the $\hat{\mathbf{z}}$ direction and we adopt an axial symmetry on the CME. We consider the vectors \mathbf{V}_{SW} , \mathbf{B}_{SW} , \mathbf{V}_{Sh} , and \mathbf{B}_{Sh} aligned with the $\hat{\mathbf{k}}$, but this text eventually write the magnitudes V_{SW} , B_{SW} , V_{Sh} , B_{Sh} .

4.1.1 Solar wind model

We use the bimodal pattern model for the SW, with the slow SW in the equator region and the fast SW close to the solar poles. For both types of winds we construct speed, density and magnetic field expressions dependent on the heliocentric distance, r . The velocity for the SWs (V_{SW}) is modeled using the hyperbolic tangent profile (e.g., [Coles et al., 1991](#); [Chen, 1996](#); [Borgazzi et al., 2009](#)),

$$V_{\text{SW}}(r) = a \tanh\left(\frac{r}{b}\right). \quad (4.3)$$

The slow and fast SW velocity profiles are defined adjusting the constants a and b using two pairs of values for the velocity and distance. From [Abbo et al. \(2010\)](#), we propose for the slow SW the velocity of 100 km s^{-1} at $3.5 R_{\odot}$. For the fast SW we assume the velocity of 200 km s^{-1} at $2.2 R_{\odot}$. We adopt the velocity of 400 km s^{-1} for the slow SW (e.g., [Chen, 1996](#)) and 700 km s^{-1} for the fast SW both at distance of $40 R_{\odot}$ (e.g., [Stakhiv et al., 2015](#)). We find the values $a = 402.7 \text{ km s}^{-1}$ and $b = 13.8$ for the slow SW, and $a = 700 \text{ km s}^{-1}$ and $b = 7.48$ for the fast SW. Figures 4.2 (a) and (b) show the velocity profiles in km s^{-1} ($V_{\text{SW}}^{\text{Slow, Fast}}$ in solid blue line), the density in cm^{-3} ($n_{\text{SW}}^{\text{Slow, Fast}}$ in dashed green line) and the magnetic field strength in G ($B_{\text{SW}}^{\text{Slow, Fast}}$ in dotted red line) of the slow and fast winds. The density and magnetic field strength are modeled using the Equation (4.4) and (4.5), respectively. Our slow SW velocity model is in agreement with [Quémerais et al. \(2007\)](#) and [Sheeley et al. \(1997\)](#).

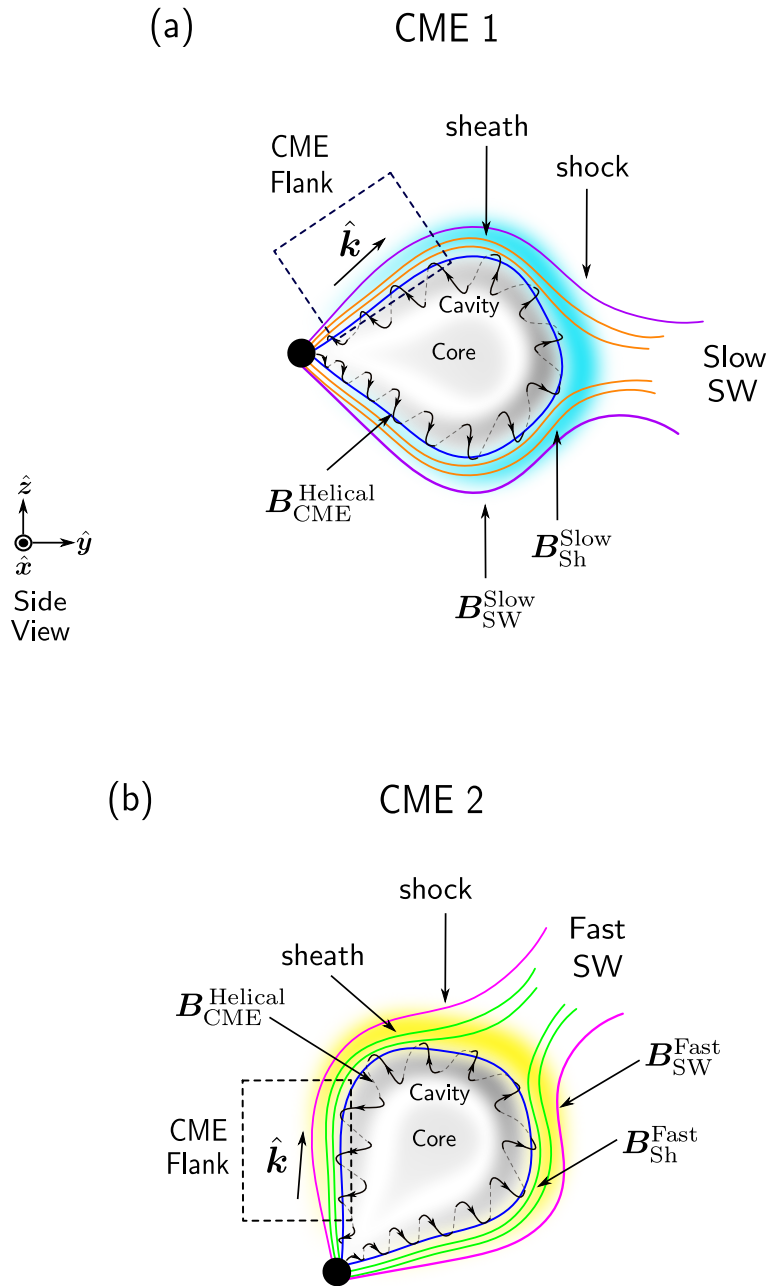


Figure 4.1: Illustrative two-dimensional scheme of the CME 1 (panel (a)) and CME 2 (panel (a)) propagating in the slow and fast solar wind (SW), respectively. The panels (a) and (b) show our zones proposed for the KHI formation on CME flanks. We also show the CMEs internal structure (core and cavity) and the presence of the external structures sheaths and shocks for both CMEs. The sheaths of the CME 1 and CME 2 are represented as the cyan and yellow shaded regions, respectively. We show the helical magnetic structures of both CMEs (curved black arrow, $B_{CME}^{Helical}$) evolved by the sheaths magnetic field lines shown B_{Sh}^{Slow} (orange lines) and B_{Sh}^{Fast} (green lines) lines and the magnetic field lines of the SW B_{SW}^{Slow} (purple lines) and fast SW B_{SW}^{Fast} (pink lines). We indicate the KHI region by dashed black line rectangle together with the shear flow, \hat{k} , on CME flanks. The solid black point represents the Sun. In our calculation we assume the solar rotation in \hat{z} direction. Source: Páez et al. (2017).

The numerical densities (n_{sw}) of the slow and fast SW were obtained using the conservation mass flux law according with the SW velocities, Equation (4.3),

$$n_{\text{sw}}(r) V_{\text{sw}}(r) r^2 = \text{constante.} \quad (4.4)$$

We take the electronic density values from [Abbo et al. \(2010\)](#) for the slow SW, $2.2 \times 10^5 \text{ cm}^{-3}$ at $3.5 R_{\odot}$, in the boundary of the streamer belt (hereafter SB). For the edge of a coronal hole (hereafter CH) we assume $1.5 \times 10^5 \text{ cm}^{-3}$ at $2.2 R_{\odot}$ (see [Figure 4.2](#) (a) and (b)).

The SW magnetic field profile is obtained from the conservation flux law assuming radial magnetic field lines,

$$B_{\text{sw}}(r) = \frac{B_{\text{sw}}(r_0)}{r^2}. \quad (4.5)$$

At the solar surface we use for the slow SW $B_{\text{sw}}(r_0) = 2.2 \text{ G}$ (e.g., [Mann et al., 2003](#)), and 6.0 G for the fast SW ([Manchester et al., 2004](#)) (see [Figure 4.2](#) (a) and (b)). [Figure 4.3](#) compares the magnetic field profile obtained with Equation (5), $B_{\text{sw}}^{\text{slow}}(r)$ (left side) and $B_{\text{sw}}^{\text{fast}}(r)$ (right side) with: (i) magnetic field profile proposed by [Dulk and McLean \(1978\)](#), $B(r) = 0.5 (r - 1)^{-1.5} \text{ G}$, for the $r \leq 10 R_{\odot}$; (ii) the profile proposed by [Patzold et al. \(1987\)](#) $B(r) = 6 r^{-3} + 1.18 r^{-2} \text{ G}$ between the heliocentric distances of $2 R_{\odot} \leq r \leq 15 R_{\odot}$; and finally (iii) with the [Gopalswamy and Yashiro \(2011\)](#) (G & Y 2011), $B(r) = 0.409 r^{-1.3} \text{ G}$, for the interval 6 to $23 R_{\odot}$. We can see from [Figure 4.3](#) that our slow SW magnetic field profile is in agreement with previous magnetic field models. [Gopalswamy and Yashiro \(2011\)](#) is the most profile-like to our fast SW magnetic profile. The disagreement between both, is due to the fact that [Gopalswamy and Yashiro \(2011\)](#) constructed the profile using a SW velocity model with terminal velocity of $\sim 400 \text{ km s}^{-1}$ ([Sheeley et al., 1997](#)).

In our calculation, we assume an error of $\pm 30\%$ on velocity, density and magnetic field strength of the SWs. In [section 4.2](#) we consider results with the error propagation from SW model ([subsection 4.1.1](#)).

4.1.2 Coronal mass ejection model

We analyze CMEs propagating in the slow and fast SW background. The interest is to construct different environments in order to identify the constraints for the KHI formation between 4 and $30 R_{\odot}$. We analyze two ejecta CME 1 and CME 2, these CMEs have the

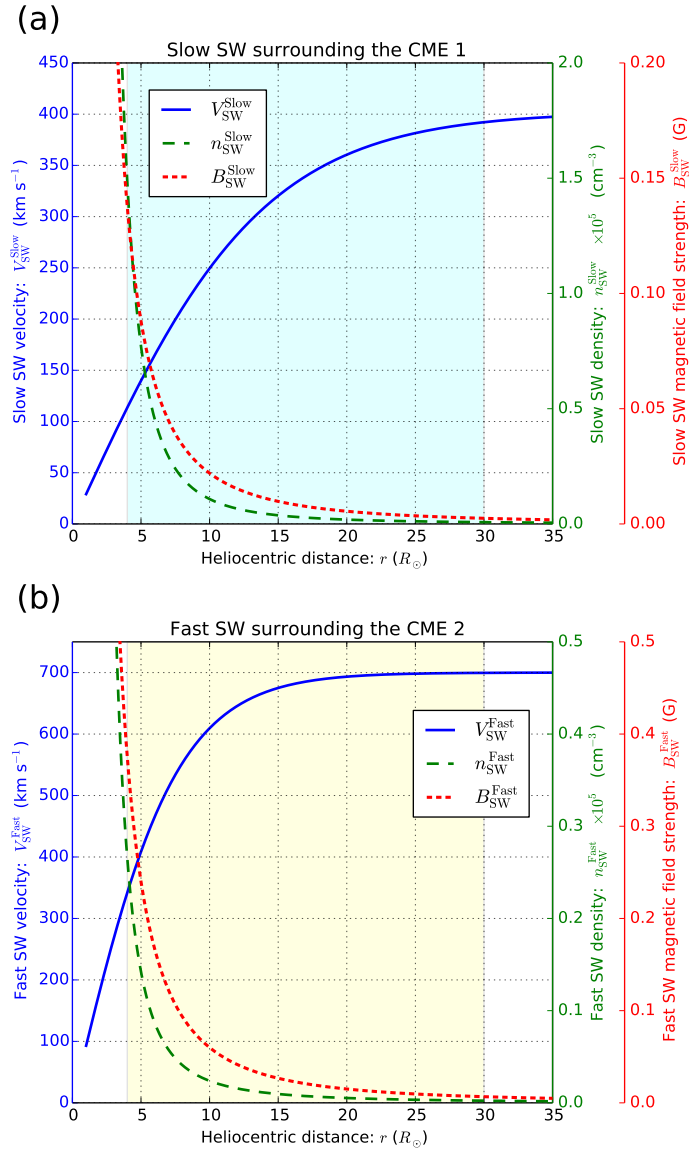


Figure 4.2: The panels show the SWs velocity, Equation (4.3) (km s^{-1} , solid blue line), SWs density Equation (4.4) (cm^{-3} , dashed green line) with the SWs magnetic field strength Equation (4.5) (G, dotted red line) of the slow (a) and fast (b) SW. The shadow cyan and yellow in background are intentional to empathize the sheath color of Figure 4.1. The axis show the color plot feature associated. Source: Páez et al. (2017).

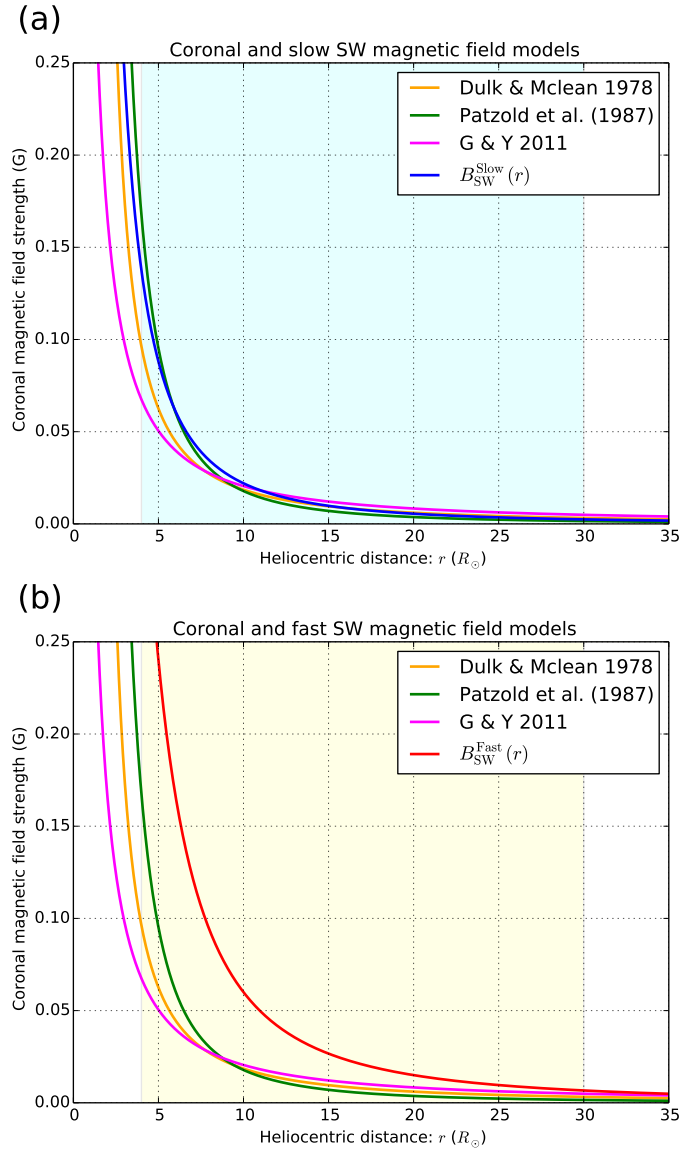


Figure 4.3: Comparative panels for the slow in (a), B_{SW}^{Slow} , Equation (4.5) and fast in (b), B_{SW}^{Fast} (red continuous line) SW (Equation (4.5)) and magnetic fields models. In orange Dulk and McLean (1978) profile. In green Patzold et al. (1987). In pink Gopalswamy and Yashiro (2011) profile (G & Y 2011). Source: Páez et al. (2017).

morphology like cone angle between opposing flanks, and structured in core, cavity and frontal loop (Illing and Hundhausen, 1985). The dynamic of the CMEs is assumed in the propagation phase, where the ejectas present a constant velocity and residual deceleration imposed by the drag force from the SW background.

The CME 1 is assumed propagating into slow SW in the SB region with a velocity 1000 km s^{-1} with residual acceleration of -4 m s^{-2} . In contrast, the CME 2 is established in an anemone active region (hereafter AR) (in the latitudes $\phi \sim 40^\circ$) evolved by fast SW in a CH within an AR (e.g. Lugaz et al., 2011; Asai et al., 2009; Liu, 2007; Liu and Hayashi, 2006). For CME 2 is adopted a propagation velocity of 1200 km s^{-1} and a residual acceleration of -2 m s^{-2} . The CH fictitious force on CME 2 (e.g. Cremades et al., 2006; Gopalswamy et al., 2009), and the effects of anemone AR on CME 2 evolution (e.g. Lugaz et al., 2011) are neglected. Figure 4.4 show the CME 1 (solid blue line) and CME 2 (solid red line) and shock 1 (dashed blue line) and shock 2 (dashed red line) velocities in the outer corona. The shock velocities are modeled in subsection 4.1.3. The limits of our interval are indicated by the vertical black lines at $4 R_\odot$ and $30 R_\odot$. The color shadows are related to sheath structure colors in Figure 4.1.

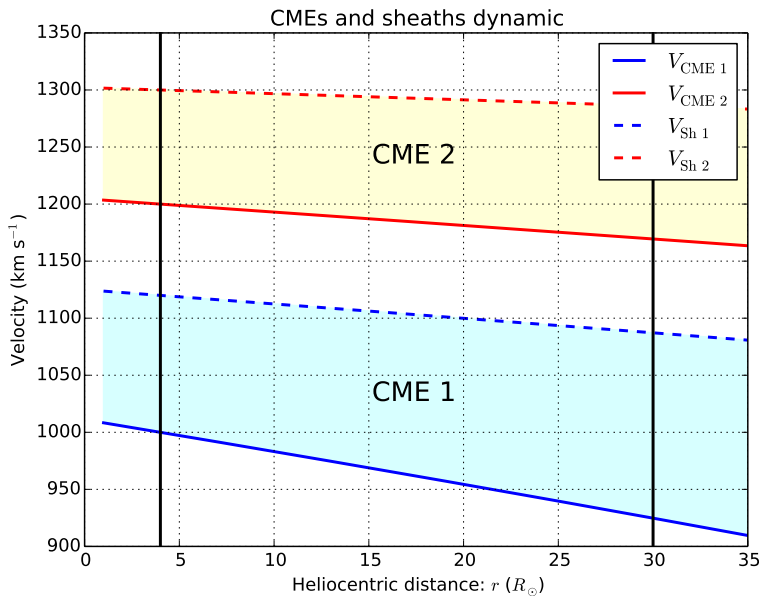


Figure 4.4: The figure shows the CME 1 velocity profile ($V_{\text{CME 1}}$, solid blue line) and sheath 1 ($V_{\text{Sh 1}}$, dashed blue line), together with the CME 2 velocity ($V_{\text{CME 2}}$, solid red line) and sheath 2 ($V_{\text{Sh 2}}$, dashed red line) in the outer corona between 4 to $30 R_\odot$ (solid black vertical lines). The shadows color are related to sheath structure colors in Figure 4.1. The cyan and yellow regions between solid and dashed blue and red lines represent the amplitude of the shear flow function, $S(r)$, Equation (4.15) for CME 1 and CME 2 cases, respectively. Source: Páez et al. (2017).

In order to solve the condition (4.2) for the KHI formation at the CME–Sh interface (in Equation (4.2) subscripts 1 and 2, respectively), we consider the CMEs densities lower than the sheath structures densities, i.e., $n_{\text{CME}} < n_{\text{sh}}$. With this, we avoid the susceptibility of our calculations to a unique CME density value. Our calculation is adapted for finding the CMEs magnetic fields strengths appropriated for the KHI formation with the propose of inquiring the reverse problem: calculate the CME magnetic fields from KHI observations. Thus, we do not model the CMEs magnetic field strengths, but we consider the CME helical magnetic field structure (Dere et al., 1999). In subsection 4.2.1 we modify our method in order to find the constraint for KHI formation. We propose as KHI regions the CME flanks (see Figure 4.1). These regions have been chosen because the magnetic field lines may be stretched by CME propagation i.e., the magnetic tension may be lower than in the curved magnetic field lines that evolve in the CME nose. Furthermore, these zones are chosen in the same way in the observational samples of Foullon et al. (2011).

4.1.3 Shock and sheath structures

To model the CMEs, we assume the formation of a parallel coronal shock in the low corona $< 2 R_{\odot}$ imposing that the ejecta velocities be faster than the magnetosonic background speed (e.g., Raymond et al., 2000; Mancuso et al., 2002). We take into account that the sheath structure becomes less dense and weaker with the increase of heliocentric distance. For this reason, we adopt a function for the sheath compression layer as the ratio between the downward and upward densities ($X = \rho_{\text{dw}}/\rho_{\text{up}}$) shown in Figure 4.1 panels (a) and (b). Bemporad and Mancuso (2011) and Bemporad et al. (2014) calculate the latitudinal plasma density compression ratio, X , in the event of the 1999 June 11 observed in C2 and C3 coronagraphs of LASCO. The authors reveal that the nose shock become from supercritical ($X \approx 3.0$) to subcritical ($X \approx 1.5$) from $\sim 2.5 R_{\odot}$ to $\sim 5.0 R_{\odot}$, respectively. However, they affirm that the CMEs flanks are subcritical ($X \approx 1.5$) in this interval. Here we propose a linear function for the compression ratio, X . We suggest that X decreases from 1.3 to 1.1 and 1.5 to 1.1 for the CME 1 and CME 2, respectively. The compression linear functions, $X_{\text{CME}}(r)$, for the CME 1 and CME 2 are given in Equations (4.6) and (4.7),

$$X_{\text{CME}_1}(r) = -0.007 r + 1.328, \quad (4.6)$$

and

$$X_{\text{CME } 2}(r) = -0.015 r + 1.56. \quad (4.7)$$

So the sheath structures densities are respectively,

$$n_{\text{Sh } 1}(r) = X_{\text{CME } 1}(r) n_{\text{SW}}^{\text{Slow}}(r), \quad (4.8)$$

and

$$n_{\text{Sh } 2}(r) = X_{\text{CME } 2}(r) n_{\text{SW}}^{\text{Fast}}(r), \quad (4.9)$$

where the slow and fast SW density, n_{SW} , correspond to the Equation (4.4).

In contrast to the asymmetrical velocities in the CME nose and CME flanks calculated in Bemporad et al. (2014), we assume that the sheath structure propagates with only latitudinal shock velocity. We propose that the shock velocities are slightly larger than CMEs velocities, but the shock accelerations are moderately lower than CME accelerations. For the shocks of the CME 1 and CME 2 we assume velocities of 1120 km s^{-1} and 1300 km s^{-1} and shock decelerations of -2 m s^{-2} and -1 m s^{-2} , respectively. Figure 4.4 shows the shock 1 (dashed blue line) and shock 2 (dashed red line) velocities in km s^{-1} between 4 to $30 R_{\odot}$, indicated in the plot by vertical black lines.

4.2 KHI formation in boundary layers

We analyze the KHI formation on the CME flanks of two ejecta propagating in the slow and fast SW. Our hypothesis considers that in these CME regions the magnetic field tension is less than in the nose of the CME region. Here, we assume axial symmetry in both CMEs. Figure 4.5 shows the general situation of the KHI regions. In panel (a) the CME, sheath, and SW plasmas are shown by gray shadows together with the CME–Sh (green shadow) and Sh–SW (orange shadow) interfaces. We show the helical magnetic field structure of the CME, $\mathbf{B}_{\text{CME}}^{\text{Helical}}$, by black arrow among the symbols \odot and \otimes , that represent the magnetic field polarities outward and inward, respectively. The sheaths (blue arrow, \mathbf{B}_{Sh}) and SW (green arrow, \mathbf{B}_{SW}) magnetic field lines are aligned with the interfaces and shear flow, $\hat{\mathbf{k}}$. In panel (b) we amplify the structure of CME–Sh interface. We decompose the $\mathbf{B}_{\text{CME}}^{\text{Helical}}$ in its poloidal ($\mathbf{B}_{\text{CME}}^{\text{Pol}}$, red arrow) and toroidal ($\mathbf{B}_{\text{CME}}^{\text{Tor}}$, blue arrow) components. Panel (c) shows the interface Sh–SW, than is less complex that the CME–Sh interface

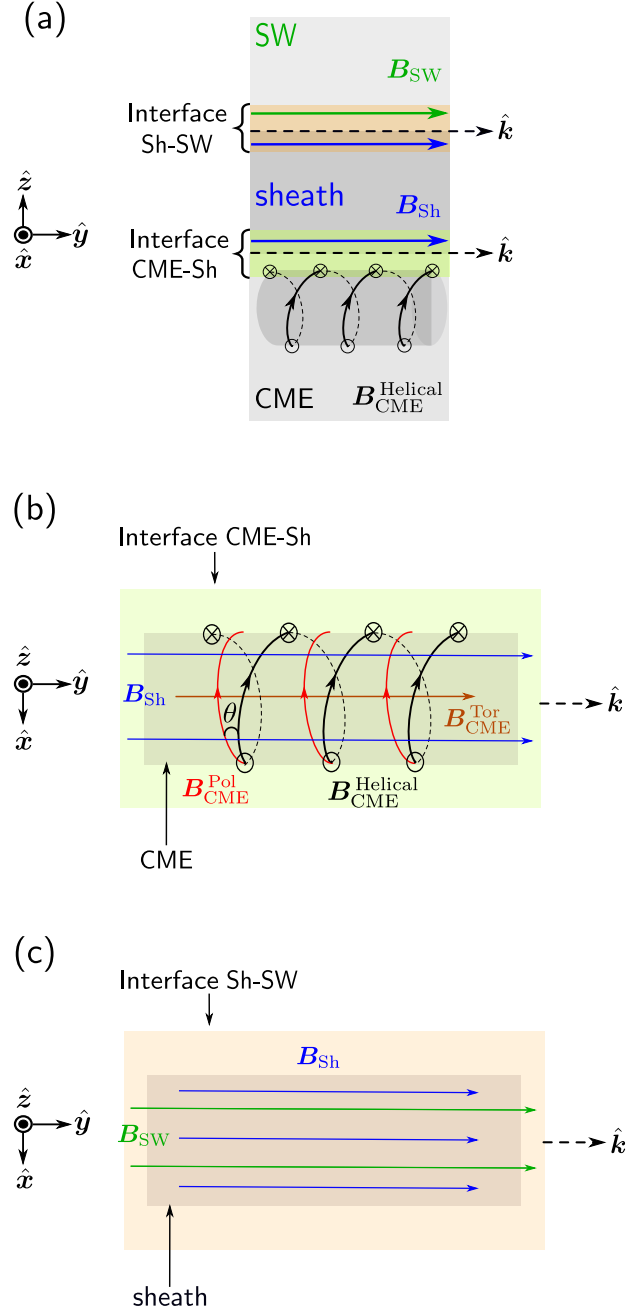


Figure 4.5: The schematic magnetic configuration of the KHI regions on the CME flanks. The panel (a) generalize the CME, sheath and SW plasmas by gray shadows and indicate the interfaces CME–Sh (green shadow), Sh–SW (orange shadow), and the shear flow, \hat{k} (dashed black arrows). We show the CME helical magnetic field $B_{CME}^{Helical}$ by black arrow among the symbols \odot and \otimes that represent the magnetic field polarities outward and inward, respectively. The sheaths (B_{Sh}) and SW (B_{SW}) magnetic field lines by blue and green arrows, respectively. In panel (b) we amplify the structure of interface CME–Sh. We decompose the $B_{CME}^{Helical}$ in its poloidal (B_{CME}^{Pol} , red arrow) and toroidal (B_{CME}^{Tor} , brown arrow) components. We simplify our calculation of these components by assuming θ angle for the stretch caused by propagation and expansion of the CME on the helical structure. We assume that B_{CME}^{Tor} affect the KHI formation while the B_{CME}^{Pol} not (Chandrasekhar, 1961). The panel (c) shows the interface Sh–SW. The structure of this boundary is less complex to CME–Sh interface due to the sheath structure is formatted by compression of the SW magnetic field lines. Source: Páez et al. (2017).

due to the sheath structure which is formatted by compression of the SW magnetic field lines. In this section, we adapt SW, CME and sheath modeling of section 4.1 in the KHI condition, Equation (4.2), in order to find constraints for KHI formation at the CME–Sh and Sh–SW interfaces for the two CME cases.

4.2.1 Interface between CME and its sheath structure

The density ratio in Equation (4.2) is simplified by assuming that the CME density (n_{CME}) is lower than the sheath density (n_{Sh}). In our calculation, we adopt that $n_{\text{CME}} < n_{\text{Sh}} \lesssim 2n_{\text{CME}}$, due to plasma accumulating in the sheaths due to propagation and expansion of the CMEs. Thus, the ratio density can be written as,

$$\frac{n_{\text{CME}} + n_{\text{Sh}}}{m_p n_{\text{CME}} n_{\text{Sh}}} \lesssim \frac{3}{m_p n_{\text{Sh}}}. \quad (4.10)$$

With this approximation, the calculation becomes independent of the CME density, n_{CME} .

We consider that $B_{\text{CME}} \gg B_{\text{Sh}}$ and so Equation (4.2) is independent of B_{Sh} ,

$$\left[\hat{\mathbf{k}} \cdot (\mathbf{V}_{\text{CME}} - \mathbf{V}_{\text{Sh}}) \right]^2 > \frac{3}{m_p n_{\text{Sh}}} (\hat{\mathbf{k}} \cdot \mathbf{B}_{\text{CME}})^2. \quad (4.11)$$

In order to solve the Equation (4.11), we analyze the term $\hat{\mathbf{k}} \cdot \mathbf{B}_{\text{CME}}$ through the poloidal, $\mathbf{B}_{\text{CME}}^{\text{Pol}}$, and toroidal, $\mathbf{B}_{\text{CME}}^{\text{Tor}}$ components of \mathbf{B}_{CME} ,

$$\hat{\mathbf{k}} \cdot \mathbf{B}_{\text{CME}}^{\text{Helical}} = \hat{\mathbf{k}} \cdot \mathbf{B}_{\text{CME}}^{\text{Pol}} + \hat{\mathbf{k}} \cdot \mathbf{B}_{\text{CME}}^{\text{Tor}}. \quad (4.12)$$

In Figure 4.5 (b) we show that $\mathbf{B}_{\text{CME}}^{\text{Pol}}$ is perpendicular to shear flow, $\hat{\mathbf{k}}$, so this component does not affect the KHI formation (Chandrasekhar, 1961). The $\mathbf{B}_{\text{CME}}^{\text{Tor}}$ is parallel to $\hat{\mathbf{k}}$, as a consequence, can influence the instability formation. We simplify the calculation of components $\mathbf{B}_{\text{CME}}^{\text{Pol}}$ and $\mathbf{B}_{\text{CME}}^{\text{Tor}}$ using the angle, θ , between the helical (black arrow) and poloidal (red arrow) magnetic field (see Figure 4.5). We interpret this angle like a measurement of the “stretch” on the helical magnetic field structure due to the propagation and expansion of the CME. We suggest that stronger stretch on the helical magnetic field may unbalance the magnetic components for larger values of θ . As first approximation, we use $\theta = 30^\circ$,

proposing a possible equipartition between the poloidal and toroidal components,

$$\hat{\mathbf{k}} \cdot \mathbf{B}_{\text{CME}} = \hat{\mathbf{k}} \cdot \mathbf{B}_{\text{CME}}^{\text{Tor}} = \sin \theta B_{\text{CME}} = \frac{1}{2} B_{\text{CME}}. \quad (4.13)$$

Using the Equation (4.13), the Equation (4.11) can be written as,

$$\hat{\mathbf{k}} \cdot \left(\mathbf{V}_{\text{CME}} - \mathbf{V}_{\text{Sh}} \right)^2 > \frac{3 B_{\text{CME}}^2}{4 m_p n_{\text{Sh}}(r)}. \quad (4.14)$$

Assuming the velocities \mathbf{V}_{CME} and \mathbf{V}_{Sh} parallel to the $\hat{\mathbf{k}}$, we define the left-side of Equation (4.14) as a shear function $S(r)$,

$$S(r) = \left| V_{\text{CME}}(r) - V_{\text{Sh}}(r) \right|. \quad (4.15)$$

The $S(r)$ function represents the shear flow between the CME and its sheath structure. Figure 4.4 shows the amplitude of the shear flow function, $S(r)$, corresponding to the cyan and yellow regions between solid and dashed blue and red lines for the CME 1 and CME 2 cases, respectively.

From Equation (4.14) we calculate the CME magnetic field appropriate for the KHI, $B_{\text{CME}}^{\text{KH}}(r)$,

$$B_{\text{CME}}^{\text{KH}}(r) < \sqrt{\frac{4 m_p n_{\text{Sh}}(r)}{3}} S(r), \quad (4.16)$$

with Equation (4.16), and it is possible to find the interval of the magnetic field strengths that allows the KHI formation between 4 and 30 R_{\odot} . In subsection 4.1.1 of the SW model we assume the $\pm 30\%$ of error in velocity, density and magnetic field strength of the SWs. For the $B_{\text{CME}}^{\text{KH}}(r)$, Equation (4.16), we assume an error of $\pm 34\%$ due to the error propagation.

Figure 4.6 shows the results of the KHI formation in the CME–Sh and Sh–SW interfaces. The CME 1 and CME 2 results are arranged in the left and right column, respectively. The superior panels show the KHI constraint at the CME–Sh interface and the inferior panels are linked to KHI constraints at the Sh–SW interface modeled in the next subsection 4.2.2. The results for both CME cases are summarized in Table 4.1. The panels (a) and (b) show the CME magnetic field strength appropriated for the KHI formation, Equation (4.16) ($B_{\text{CME}}^{\text{KH}}$, solid red line), the logarithm of the shear flow function $S(r)$, Equa-

tion (4.15) ($\log S(r)$, dashed black line). The cyan and yellow shadow in the plots represent the colors assumed in Figure 4.1 for the sheaths structures.

We find different results at CME–Sh interface for the two CMEs cases. Our results illustrate a notable decrease of the $B_{\text{CME}}^{\text{KH}}(r)$ due to the falling of the sheath density function consequence of the SW density (i.e., $n_{\text{sh}}(r) \propto n_{\text{sw}}(r)$). The $S(r)$ and $\log S(r)$ increasing by deceleration of the CME in the SW, see Figure 4.4. The differences of the $B_{\text{CME}}^{\text{KH}}(r)$ values for both CMEs cases, i.e., $B_{\text{CME 1}}^{\text{KH}}(r) > B_{\text{CME 2}}^{\text{KH}}(r)$, are consequence of the SW densities because the shear values are similar (see Table 4.1). The set values $B_{\text{CME 1}}^{\text{KH}}(r)$ are two times larger than $B_{\text{CME 2}}^{\text{KH}}(r)$. Due to reason we suppose that for the conditions assumed in this paper the CME 1 environment is more addequated for the KHI formation than the CME 2 environment. From the results, we conclude that the region close to $\gtrsim 4 R_{\odot}$ is more probable for KHI existence due to larger $B_{\text{CME}}^{\text{KH}}$ values comparative to others distances i.e., $\gtrsim 20 R_{\odot}$. With this, Figure 4.6 represent the quantitative KHI constraints that evidenced the susceptibility of the CME–Sh boundary layer to the KHI formation.

4.2.2 Interface between the sheath and solar wind

Using the same methodology as in subsection 4.2.1, we model the Sh–SW interface. Through the Equations (4.8) and (4.9), we can rewrite the term, $n_{\text{sw}} + n_{\text{sh}}$, equivalent to $(1 + X_{\text{CME}}) n_{\text{sw}}$. Thus, the densities ratio in (4.2) is simplified to,

$$\frac{n_{\text{sw}} + n_{\text{sh}}}{m_p n_{\text{sw}} n_{\text{sh}}} \approx \frac{(1 + X_{\text{CME}})}{m_p n_{\text{sh}}}. \quad (4.17)$$

Assuming the magnetic fields (\mathbf{B}_{sh} , \mathbf{B}_{sw}) and velocities (\mathbf{V}_{sh} , \mathbf{V}_{sw}) of the sheaths and SWs along the shear flow, $\hat{\mathbf{k}}$, we rewritten Equation 4.1 as,

$$(V_{\text{sh}} - V_{\text{sw}})^2 > \frac{(1 + X_{\text{CME}})}{m_p n_{\text{sh}}} (B_{\text{sh}}^2 + B_{\text{sw}}^2). \quad (4.18)$$

For Equation 4.18 we approximate the sheaths magnetic field strength like $B_{\text{sh}} < 2 B_{\text{sw}}$,

$$B_{\text{sh}}^2 + B_{\text{sw}}^2 \lesssim 5 B_{\text{sw}}^2. \quad (4.19)$$

Inserting the Equations (4.17) and (4.19) into Equation (4.18) we calculate the final con-

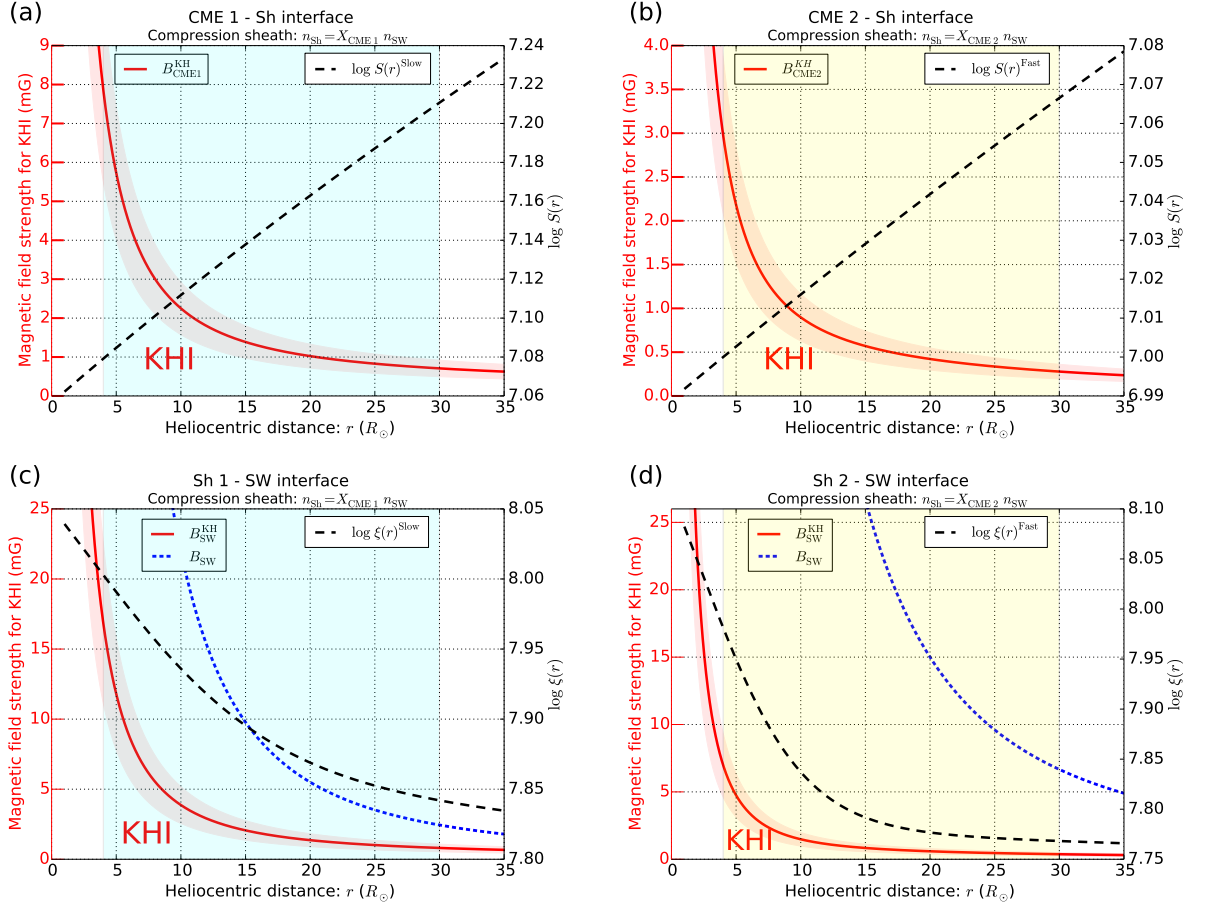


Figure 4.6: Plots for the KHI formation constraints. The panels (a) and (b) show the CME magnetic field, B_{CME}^{KH} , (Equation (4.16), solid red line) necessary for the KHI formation and the logarithm of the shear flow, $S(r)$, (Equation (4.15), dashed black line) for the interfaces CME 1–Sh and CME 2–Sh, respectively. The values below the B_{CME}^{KH} curve are the appropriate for KHI formation. The panels (c) and (d) show the SW magnetic field strength, B_{SW} , (Equation (4.5), dotted blue line), SW magnetic field strength for the KHI formation, B_{SW}^{KH} , (Equation (4.22), solid red line) and the shear flow, $\xi(r)$ (Equation (4.21), dashed black line). The values below the B_{SW}^{KH} curve are linked with KHI formation. The blue shadow along the B_{SW} represent the error of $\pm 30\%$ assumed in the SW model, while the red shadow along of B_{CME}^{KH} and B_{SW}^{KH} represent the error propagation of $\pm 34\%$. The cyan and yellow shadow represent the colors assumed in Figure 4.1 for the sheaths structure. We find CME and slow SW magnetic field values less than 7.9 ± 2.7 mG and 16.8 ± 5.7 mG, respectively, may allow the KHI in slow SW environment. While CME and fast SW magnetic field values less than 3.0 ± 1.0 and 7.0 ± 2.4 mG, respectively, allow the instability in fast SW environment. These results are summarized in Table 4.1. Our calculation show that KHI magnetic field strength of Sh–SW interfaces are larger than CME–Sh interfaces for both CMEs cases, in this way we comment that Sh–SW interface will be susceptible to the KHI formation. Source: Páez et al. (2017).

dition for the KHI formation at the Sh–SW interface,

$$(V_{\text{sh}} - V_{\text{sw}})^2 > \frac{5(1 + X_{\text{CME}})}{m_p n_{\text{sh}}} B_{\text{sw}}^2. \quad (4.20)$$

From the left-hand side of the Equation (4.20) we define the velocity shear function $\xi(r)$,

$$\xi(r) = \left| V_{\text{sh}}(r) - V_{\text{sw}}(r) \right|. \quad (4.21)$$

The SW magnetic field strength appropriate for the KHI formation is calculated from,

$$B_{\text{sw}}^{\text{KH}}(r) < \sqrt{\frac{m_p n_{\text{sh}}(r)}{5(1 + X_{\text{CME}})}} \xi(r). \quad (4.22)$$

In similar way to the $B_{\text{CME}}^{\text{KH}}(r)$, Equation (4.16), from the error assumed in the model of the SWs, i.e., $\pm 30\%$ (subsection 4.1.1), we assume an error propagation of $\pm 34\%$ in $B_{\text{sw}}^{\text{KH}}(r)$, Equation 4.22.

Table 4.1 - Results from Figure 4.6 for the CME 1 and CME 2 cases for 4 and 30 R_{\odot} at the CME–Sh and Sh–SW interfaces. Shear function S (km s^{-1}), the CME magnetic field strengths for the KHI existence $B_{\text{CME}}^{\text{KH}}$ (mG), the shear function ξ (km s^{-1}) and the SW magnetic field strengths for the KHI existence $B_{\text{sw}}^{\text{KH}}$ (mG).

r (R_{\odot})	Interface CME–Sh		Interface Sh–SW	
	S (km s^{-1})	$B_{\text{CME}}^{\text{KH}}$ (mG)	ξ (km s^{-1})	$B_{\text{sw}}^{\text{KH}}$ (mG)
CME 1				
4.0	120.0	7.9 \pm 2.7	1006.4	16.8 \pm 5.7
30.0	162.4	0.7 \pm 0.2	695.0	0.8 \pm 0.3
CME 2				
4.0	100.0	3.0 \pm 1.0	957.9	7.0 \pm 2.4
30.0	116.5	0.3 \pm 0.1	586.4	0.4 \pm 0.1

Figures 4.6 (c) and (d) show the SW magnetic field strength, $B_{\text{sw}}(r)$, (Equation (4.5), dotted blue line), the SW magnetic field strength appropriated for the KHI formation, $B_{\text{sw}}^{\text{KH}}(r)$, (Equation (4.22), solid red line), and the logarithm of the shear flow, $\log \xi(r)$, (Equation (4.21), dashed black line). The magnetic field strength less than $B_{\text{sw}}^{\text{KH}}(r)$ allow the KHI formation. In a similar way to the Figures 4.6 (a) and (b), the $B_{\text{sw}}^{\text{KH}}(r)$ decrease by effect of the SW density, n_{sw} , in the heliocentric distance, r . The shear functions in Sh–SW interface, $\xi(r)$ and $\log \xi(r)$, are larger than the shear function in CME–Sh interface, $S(r)$ and $\log S(r)$ and decrease in consequence of the shock deceleration the SWs, see Figure 4.4.

The values of the $B_{\text{SW}}^{\text{KH}}$ of the slow SW are approximately two times larger than $B_{\text{SW}}^{\text{KH}}$ of the fast SW. The results show that $B_{\text{SW}}^{\text{KH}}(r) < B_{\text{sw}}(r)$, but assuming the error propagation ($\pm 34\%$, red shadow) we suppose that the region appropriated for the KHI formation will be at larger distances i.e., $\gtrsim 20 R_{\odot}$, contrary to the CME–Sh interface. The panel (c) show larger $B_{\text{SW}}^{\text{KH}}$ than panel (d), in this way we consider the Sh–SW interface of the CME 1 more susceptible to the KHI formation than Sh–SW interface of the CME 2.

Our calculation is focused on quantitative requirements in order to understand if the interfaces are predisposed to the KHI formation. The results in Figure 4.6 indicate that CME 1 interfaces are more convenient for the KHI formation than the CME 2 interfaces, due to denser slow SW and the amplitude of the shear flows. In order to optimize both CMEs environments for the KHI formation we can increase the shear flow at the interfaces (i.e., analyze faster CMEs), or increase the density in the sheath structures (Zhelyazkov et al., 2015). These two options may be linked because the environments of faster CMEs can originate stronger shocks and consequently denser sheaths structures. In a complementary way, from Magdalenic et al. (2010), we indicate that the flare energy released associated to a CME may originate sheath denser structures, increasing the possibilities of the KHI formation. We find that the best CME environment according to the KHI formation consist in a faster CME with a flare associated that propagate into slow SW. These are exactly the CME features of CME that occurred on 2010 November 3 analyzed in Foullon et al. (2011), where was evidenced the KHI formation.

4.3 Discussion and conclusions

Previous works have shown KHI observations in low corona distances (e.g., Foullon et al., 2011; Ofman and Thompson, 2011; Möstl et al., 2013) in different CME events. In contrast, this paper shows the first discussion of KHI existence in the outer solar corona. Our work is focused on analyzing the boundary layers CME–Sh and Sh–SW between 4 to $30 R_{\odot}$, for two different CME cases. The interest in this interval is justified considering that the plasma magnetic field strengths decrease while the plasma velocities increase and this combination may optimize the CME environments for the KHI development.

Here, we define two CME-driven shock environments. In the first one, the CME propagates in the slow SW, and the second one, the CME propagates in the fast SW. The

velocities, densities, and magnetic field strengths of the CMEs, the sheaths and the SWs were modeled in order to solve the condition for the KHI existence proposed by Chandrasekhar (1961). For both CMEs and shock propagation is imposed a residual deceleration by drag force of the SW background. The geometrical disposition at the interfaces was simplified by assuming a parallel shock, and some variables that can affect the KHI existence e.g., compressibility and viscosity, were neglected. In this way, it is shown the most favorable ambient for the KHI development in order to understand a broadest set of the KHI constraints. In this work at the CME–Sh interface, we only consider the harmonics with wave vector parallel to the flow. These harmonics are stabilized by flow-aligned magnetic field. However, the harmonics that have wavenumbers perpendicular to the flow still could be unstable to KHI when there is small transverse component of magnetic field (Singh and Talwar, 1994; Zaqarashvili et al., 2010, 2014, 2015).

The functions $B_{\text{CME}}^{\text{KH}}(r)$, Equation (4.16), and $B_{\text{SW}}^{\text{KH}}(r)$, Equation (4.22), represent the maximum magnetic field intervals that allow the KHI formation at the CME–Sh and Sh–SW interfaces. The values here are equal and lower quantitative constraints for the KHI formation. We find that CME 1 and slow SW magnetic fields values lower than 7.9 ± 2.7 mG (10^{-3} G) and 16.8 ± 5.7 mG, respectively, may allow the instability formation. For the CME 2 and fast SW magnetic field values lower than 3.0 ± 1.0 mG and 7.0 ± 2.4 mG, respectively, are susceptible to the KHI existence (see Figure 4.6, Table 4.1). The calculations show that CME 1 environment is more susceptible to the KHI formation because the $B_{\text{CME}}^{\text{KH}}$ and $B_{\text{SW}}^{\text{KH}}$ are larger than the respective magnetic fields strengths in the CME 2 environment. We explain this fact by the different values of the SWs densities (i.e., $n_{\text{SW}}^{\text{Slow}}(r) > n_{\text{SW}}^{\text{Fast}}(r)$) and values of the shear functions (i.e., $S_{\text{CME 1}}(r) > S_{\text{CME 2}}(r)$ and $\xi_{\text{CME 1}}(r) > \xi_{\text{CME 2}}(r)$) shown by cyan and yellow shadow regions in Figure 4.4. We consider $\pm 30\%$ of error on the SW model due to the variable behavior of the SWs, this drives an error propagation in our results of $\pm 34\%$. We consider that for both CMEs cases the Sh–SW interface is more susceptible to the KHI formation due to larger magnetic field strength that allows the instability formation, in addition to the magnetic structure less complex than in the CME–Sh interfaces. Figure 4.6 shows that the slow Sh–SW interface close to the $26 R_{\odot}$ has the quantitative constraints for the KHI formation, but the fast SW interface does not. From our results, we can affirm that Sh–SW interface of the CME 1 case may be the best environment for KHI formation. So, our hypothesis shows that the best CME conditions

for the KHI formation are faster CMEs propagating in the solar equator region, features that are shown on the CME occurred on 2010 November 3 and analyzed in [Foullon et al. \(2011\)](#). We have some limitations to our model that are imposed by the complexity of the helical magnetic field structure of the CMEs. We consider the toroidal and poloidal components, by this, we find that the CME stretch may be a relevant parameter of the environment that may define the KHI formation in addition to the previous constraints like the ratio density checked by [Zhelyazkov et al. \(2015\)](#).

We emphasize that a flare associated to the CME release energy contributes to the formation of a denser sheath structure (e.g., [Magdalenic et al., 2010](#)). The Equations (4.16) and (4.22) express that increases in the density sheath, n_{sh} , amplify the threshold of the conditions for the KHI existence, i.e., $B_{\text{CME}}^{\text{KH}} \propto n_{\text{sh}}$. We conclude that a flare is a qualitative constraint of the CME environment appropriate for the KHI formation. On the other hand, under results of [Magdalenic et al. \(2010\)](#), may be possible to find the KHI formation in slow CMEs ($<500 \text{ km s}^{-1}$) due to energy liberation of associated flares. Finally, we indicate the results as sample of the predisposition of the CMEs environments to the instability. We interpret our calculations as forecast of the CME magnetic field measurements from KHI observations and vice versa.

We discuss two relevant points of the KHI phenomenon in CME-events and use the KHI observations as a tool to estimate the CME magnetic field strength. The seldom observations of the KHI may indicate two limitations associated with the KHI formation and evolution. The first may question whether the system (CME, sheath, shock, and SW) is predisposed to the KHI. The second is linked to the question if KHI evolution in CME-events may be result of the technological limitations of the instruments on board of the current solar spacecrafts. Our work shows the predisposition of the system to the KHI existence in outer solar corona distances. Our results show that KHI may be more frequent in the CMEs environments than the events registered. On this point, the features of the KHI evolution may be imperceptible, i.e., smaller vortice sizes or wavelength or growth-rate, these features may do not allow the instability to be monitored. In this way, we consider that new generation of spacecraft i.e., Parker Solar Probe, Solar Orbiter and Solar Sentinels may overcome these limitations and detect more frequently the KHI evolution in the outer corona distances. Finally, we think that our work can be interpreted like the first discussion on KHI formation in new solar corona environment, unlike the

discussions in previous works. We show that KHI may exist, that way, our work is the departure point for new studies on KHI formation and CME magnetic field strength.

Part II:

SEPs and self-turbulence regions
in corrugated CME-driven shocks

SEPs and self-turbulence regions in corrugated CME-driven shocks

The study of the solar energetic particles (SEPs) is an essential element of research in heliospheric science. We present a study where are analyzed the distributions of the regions of the particle acceleration and turbulence in the shock front with wave-like features, here called corrugated shocks. For this reason, we assume disturbances from medium and CMEs on the shock waves. We consider that accepting these features on shocks may be a start point for investigating some issues in the sheath and shock, as downstream-jets, instabilities, shock thermalization, shock stability, and injection particle process. In this Chapter, we present our manuscript titled “SEPs and self-generated turbulence regions in corrugated CME-driven shocks”, submitted to [The Astrophysical Journal](#) on 2018 May 19 and currently under revision. This study was constructed in collaboration with Professor Dr. Diego Falceta-Gonçalves and Professor Dr. Merav Opher ([Páez et al., 2018](#)).

3 SOLAR ENERGETIC PARTICLES AND SELF-GENERATED TURBULENCE REGIONS IN CORRUGATED
4 CME-DRIVEN SHOCKS

5 A. PÁEZ ¹, V. JATENCO-PEREIRA ¹, D. FALCETA-GONÇALVES ², & M. OPHER ³

6 ¹ Universidade de São Paulo, Instituto de Astronomia, Geofísica e Ciências Atmosféricas, Departamento de Astronomia, Rua do Matão
7 1226, São Paulo, SP, 05508-090, Brazil; andresspaez@usp.br

8 ² Universidade de São Paulo, Escola de Artes, Ciências e Humanidades, Rua Arlindo Bettio 1000, São Paulo, SP, 03828-000, Brazil

9 ³ Astronomy Department, Boston University, Boston, MA 02215, USA

Draft version 19th May, 2018

10 ABSTRACT

11 The study of the solar energetic particles (SEPs) is an essential element of research in the heliospheric
12 science. Here, we explore the distributions of particle acceleration and self-generated turbulence
13 regions around coronal mass ejections (CMEs)-driven shocks with corrugated wave-like features. We
14 adopt these attributes on shocks formed from disturbances due to the bimodal solar wind, CME
15 deflection, irregular CME expansion, and the ubiquitous fluctuations in the solar corona. In order to
16 understand the role of a wavy shock in SEPs and turbulence phenomena, we define three different
17 smooth shocks morphology each one associated with a fast CME. Using polar Gaussian profiles we
18 study these shocks in the low corona. We establish the corrugated appearance on smooth shock
19 by using combinations of wave-like functions that represent the disturbances of medium and CME
20 piston. For both shock types, we calculate the shock normal angles between the shock normal and the
21 radial upstream coronal magnetic field in order to classify the quasi-parallel and quasi-perpendicular
22 regions linked to the SEPs and turbulence regions, respectively. Our results show that corrugated
23 shocks present a predisposition to the SEPs phenomenon. We suggest that disturbances due to CME
24 irregular expansion may be a decisive factor in SEPs origin. Finally, we regard that accepting these
25 features on shocks may be the start point for investigating some questions in the sheath and shock, like
26 downstream-jets, instabilities, shock thermalization, shock stability, and injection particle process.

27 *Keywords:* shock waves - plasmas - Sun: coronal mass ejections (CMEs)- Sun: particle emission - Sun:
28 magnetic fields - turbulence

29 1. INTRODUCTION

30 Coronal mass ejections (CMEs) are the strongest phe-
31 nomena in solar surface that reconfigure notably the
32 global coronal magnetic field (e.g., [Low 2001](#); [Liu et al. 2009](#)). In the low corona distances the magnetic field
33 is affected by the early stages of CME evolution i.e.,
34 initiation and acceleration phases (e.g., [Zhang & Dere 2006](#) and references therein). The super-Alfvénic CMEs
35 (> 800 km s⁻¹) originate a coronal shock wave in dis-
36 tances of ~ 1.5 R_⊙ (e.g., [Ma et al. 2011](#); [Zucca et al. 2014](#); [Gopalswamy et al. 2016](#)), evidenced through the
37 radio Type II burst ([Wild & McCready 1950](#); [Uchida 1960](#)), and Moreton waves ([Moreton 1960](#); [Moreton & Ramsey 1960](#)). Together with the shock wave, the sheath
38 structure is established by accumulating coronal plasma
39 by the CME compression on medium. The shock and
40 sheath generate conditions appropriated for particle ac-
41 celeration (e.g., [Zank et al. 2000](#); [Manchester et al. 2005](#);
42 [Kozarev et al. 2013](#)). In the shock wave, the particles
43 are accelerated by first-order Fermi mechanism or diffuse
44 shock acceleration (e.g., [Bell 1978a,b](#); [Blandford & Ostriker 1978](#)). This type of particles are known as gradual
45 solar energetic particles (electrons, protons, ions, here-
46 after SEPs, [Reames 1999, 2013](#)).

47 Some CMEs exhibit the shock signatures in the CME
48 flanks or in the CME nose regions (e.g., [Ontiveros & Vourlidis 2009](#)), consequently some events show the ori-
49 gin of SEPs in shock flanks (e.g., [Kahler 2016](#)), or in at
50 shock nose (e.g., [Reames et al. 1997](#); [Reames 1999](#)). In

51 large SEPs events, fastest CMEs (~ 2000 km s⁻¹) associ-
52 ated with the Ground Level Enhancement (GLE) events,
53 the particle acceleration can occur from ~ 2.0 to ~ 4.0 R_⊙,
54 with average in ~ 3.0 R_⊙ (e.g., [Reames 2009](#); [Gopal-
55 swamy et al. 2012](#)). The SEPs are accelerated in the
56 shock supercritical regions. In these regions the down-
57 stream Alfvénic Mach number, M_A , is larger than the
58 critical Mach number, M_A^{crit} , which the flows and sound
59 velocities are equivalent (e.g., [Edmiston & Kennel 1984](#)).
60 According to the shock normal angle, θ_{Bn} , between the
61 shock normal and the upstream magnetic field, the su-
62 percritical shock can be manifested by two phases: the
63 quasi-parallel ($0 \leq \theta_{\text{Bn}} \leq \pi/4$) and quasi-perpendicular
64 ($\pi/4 \leq \theta_{\text{Bn}} \leq \pi/2$) ([Balogh & Treumann 2013](#) page 28).
65 Recently, [Bemporad & Mancuso \(2011\)](#) and [Bemporad
66 et al. \(2014\)](#) analyzed the CME-driven shock occurred
67 in 1999 June 11, that showed supercritical and subcritical
68 conditions in the shocks nose and flank, respectively,
69 at distances of ~ 2.6 R_⊙. The authors affirm that their
70 results are important to locate the zones of particle ac-
71 celeration. On the other hand, others explore the ubiqui-
72 tous properties of CMEs and the solar corona that may
73 influence the SEPs origin. [Schwadron et al. \(2015\)](#) ana-
74 lyze the role of expansion and acceleration of a CME on
75 particle acceleration. The authors suggest the existence
76 of a rigidity regime and shocks compression ratio appro-
77 priated for SEPs origin. [Petukhova et al. \(2017\)](#) explore
78 the dependence of the particle spectra with the initial
79 CME radius. [Kong et al. \(2017\)](#) show that shocks can
80 accelerate particles more efficiently when propagating in

5.1 Methodology

Recently, some works evidenced the importance of taking in account realistic properties of the solar corona and the CMEs in the origin and transport of the SEPs as bimodal SW (Manchester et al., 2005), supercritical regions (Bemporad and Mancuso, 2011), expansion and acceleration of the CMEs (Schwadron et al., 2015), particle spectra dependence with the CME radius (Petukhova et al., 2017), among others. In a similar way, we propose an analysis of the predisposition of the wavy or corrugated shocks to the SEPs and turbulence phenomena. These shocks maintain wave-like features due to the disturbances from the solar corona, SW, CME piston. Susino et al. (2015) show the CME-driven shock of 2011 June 7 between heliocentric distances from 2 to 12 R_{\odot} and angular width of 110° by images of coronagraphs C2 and C3 of LASCO/SOHO. The authors show the shock front location with the irregular shock shape features, see Figure 5 in Susino et al. (2015). Similar irregular shock front also are observed in the CME-driven shock that occurred on at 1999 June 11 Bemporad and Mancuso (2011), Bemporad and Mancuso (2013), and Bemporad et al. (2014).

In order to understand the relevance of the corrugated shocks, we compare two shock morphology types: smooth and corrugated shocks. Our methodology is structured in two steps. First, in subsection 5.1.1, we model the smooth shocks. Second, in subsection 5.1.2, we impose fluctuations on smooth shock, assuming ubiquitous disturbances from medium on the shock wave. Figure 5.1 shows the side view configurations of the six CME-driven shocks analyzed in this paper. We consider three CMEs: CME 1, CME 2, and CME 3 and their shocks waves in different latitudinal locations (green, blue, and orange thick lines, these color features are used through the paper). Panels (a), (b), and (c) show the smooth shocks. These shocks morphology have similar features to the events of 1999 September 11 (here assumed in the equator region), 1997 November 6, and 1998 June 4 analyzed in Ontiveros and Vourlidas (2009). For these CMEs, we consider velocities larger than 1000 km s^{-1} , and cone-like structure core, cavity and frontal loop (Illing and Hundhausen, 1985). The CME-pause and coronal magnetic field lines (MFL) are indicated by red and black thin lines, respectively. In all cases, the sheath structure (yellow shadow) is assumed and the CME magnetic reconnection is neglected. Panels (d), (e), and (f) illustrate our propose of corrugated CME pistons and shocks. For the six cases, we analyze the shock

width in order to provide a general diagnostic. But particularly, we adopt the supercritical shocks conditions at the convex regions (rounded) indicated by the green, blue, and orange transverse lines (e.g., [Bemporad and Mancuso, 2011](#); [Bemporad et al., 2014](#)).

5.1.1 Coronal smooth shocks model

We model the smooth shock surface by polar Gaussian plots, $S_m(\phi)$, as function of latitude coordinate, ϕ (e.g., [Wood and Howard, 2009](#); [Wood et al., 2010, 2011](#)). The subscript m with values $m = 1, 2, 3$ identify the shock morphology associated to each CME, see [Figure 5.1](#). The shocks location is adjusted close to $\sim 3.0 R_\odot$ according to the coronal distances of shock formation at $\sim 1.5 R_\odot$ (e.g., [Ma et al., 2011](#); [Zucca et al., 2014](#); [Gopalswamy et al., 2016](#)), SEPs onset between ~ 2.0 to $\sim 4.0 R_\odot$ (e.g., [Reames, 2009](#); [Gopalswamy et al., 2012](#)), and supercritical shock detections $\sim 2.5 R_\odot$ (e.g., [Bemporad and Mancuso, 2011](#); [Bemporad et al., 2014](#)).

We construct the shocks shape, $S_m(\phi)$, from an initial parabolic-like shape profile,

$$h(\phi) = \exp\left(-\frac{\phi^2}{2}\right). \quad (5.1)$$

From CMEs observation is possible to consider that these parabolic-like shape can be more realistic than circular profiles due to the nonuniform ejecta driver. Close to the SEPs onset, we define the first shock surface, $S_1(\phi)$ as multiple of $h(\phi)$,

$$S_1(\phi) = 2.8 h(\phi). \quad (5.2)$$

This shock is the simplest CME-driven shock morphology. We assume $S_1(\phi)$ in order to represent the CME event of 1999 September 11 studied in [Ontiveros and Vourlidis \(2009\)](#) (here consider in the equator region).

The shocks $S_2(\phi)$ and $S_3(\phi)$, [Figure 5.1\(b\)](#) and (c), keep a more complex morphology than the $S_1(\phi)$. In order to establish these shocks, we use an auxiliary function structured as the sum of polar Gaussian functions,

$$p_m(\phi) = \sum_{i=-9}^9 a_i \exp\left[-b_i \left(\phi - \frac{i\pi}{20}\right)^2\right]. \quad (5.3)$$

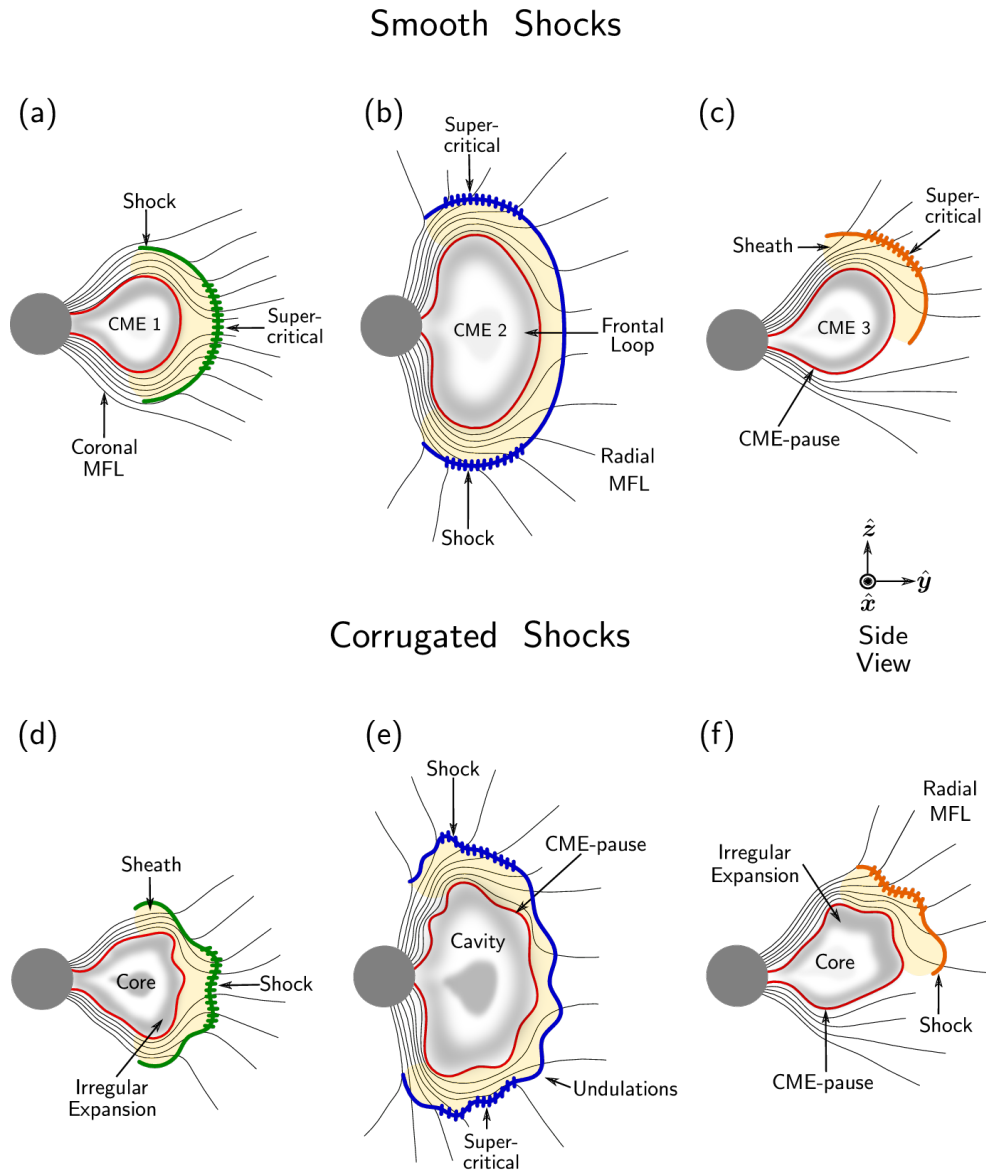


Figure 5.1: Schematic view of a meridional view of CME 1, CME 2, and CME 3 and their shocks. We show three different CMEs structures: core; cavity; and frontal loop (Illing and Hundhausen, 1985). For all situations we considered a sheath structure (yellow shadow) formed behind the shocks. The CME-pause and coronal magnetic field lines (MFL) are indicated by the red and black thin lines, respectively. Panels (a), (b), and (c) indicate the smooth shocks. For the three CME cases, the shock signatures (green, blue, and orange thick lines) are assumed in different latitude locations. The shock morphology preserve similar features to the events of 1999 September 11 (here assumed in the equator region), 1997 November 6, and 1998 June 4 studied in Ontiveros and Vourlidis (2009). Panels (d), (e), and (f) show our proposed corrugated shocks. We assume this type of shock by imposing wave-like features from bimodal SW (e.g., Manchester et al., 2005), CME deflection (e.g., Kay et al., 2013, 2015), CME irregular expansions (e.g., Evans et al., 2011), and ubiquitous fluctuations of density and magnetic field of the solar corona (e.g., Warmuth and Mann, 2005; Evans et al., 2008; Zucca et al., 2014). For the six cases, we analyze throughout the shock width in order to provide a general diagnostic. But particularly, we adopt the supercritical shocks conditions at the convex regions (rounded) indicated by the green, blue, and orange transverse lines (e.g., Bemporad and Mancuso, 2011; Bemporad et al., 2014). Source: Páez et al. (2018).

The mathematical flexibility of the $p_m(\phi)$ function through its parameters of amplitude (a_i), width (b_i), and locations ($i\pi/20$), and the range positive (≥ 0) of the Gaussian profiles, allow to generate the $S_2(\phi)$ and $S_3(\phi)$ in combination of $h(\phi)$ with $p_m(\phi)$,

$$S_2(\phi) = 1.5 h(\phi) + p_2(\phi), \quad (5.4)$$

and

$$S_3(\phi) = 2.3 h(\phi) + p_3(\phi). \quad (5.5)$$

Table 5.1 shows the positive constants a_i and b_i . These are adjusted in order to the shocks $S_2(\phi)$ and $S_3(\phi)$ to be latitudinally symmetric and mimic the shock shape of 1999 May 27, and 1998 June 4 (Ontiveros and Vourlidas, 2009), respectively.

Figure 5.2(a) shows the profiles, $h(\phi)$ (black dashed line), and the shock functions $S_1(\phi)$ (green line), $S_2(\phi)$ (blue line), and $S_3(\phi)$ (orange line). Panel (b) shows the plots of the corrugated shocks construct in subsection 5.1.2. In plots the gray shadow from $2.0 R_\odot$ to $4.0 R_\odot$ indicate the interval where we analyze the shocks. The green, blue, and orange transverse lines at the shocks convex regions indicate our initials zones with supercritical shock conditions.

5.1.2 Coronal corrugated shocks model

During the early evolution stages of the CME in the low corona, the ejecta suffers several disturbances from medium that causes non-uniform expansion and deflection of the CME. We consider that these disturbances impose wave-like features on the CME piston. Consequently, we assume these type of wavy features on the shock front. These perturbations to the shape and velocity of the shock front are known as corrugation instability (e.g., Gardner and Kruskal 1964 and Landau and Lifshitz 1987). Also we consider that shock disturbances may be consequence of the CME driver evolution, and one reason could be internal reconnection as suggested by Fermo et al. (2014).

Among factors that may affect the shock morphology in a relative large scale are the types of SW and the CME deflection. The SW affect the CME due to the difference of velocities between the slow and fast wind (e.g., Manchester et al., 2005; Savani et al., 2010), as also its boundary wind (Stakhiv et al., 2015). On the other hand, the CME deflection is consequence of the magnetic forces of tension and pressure gradient, together to the non-

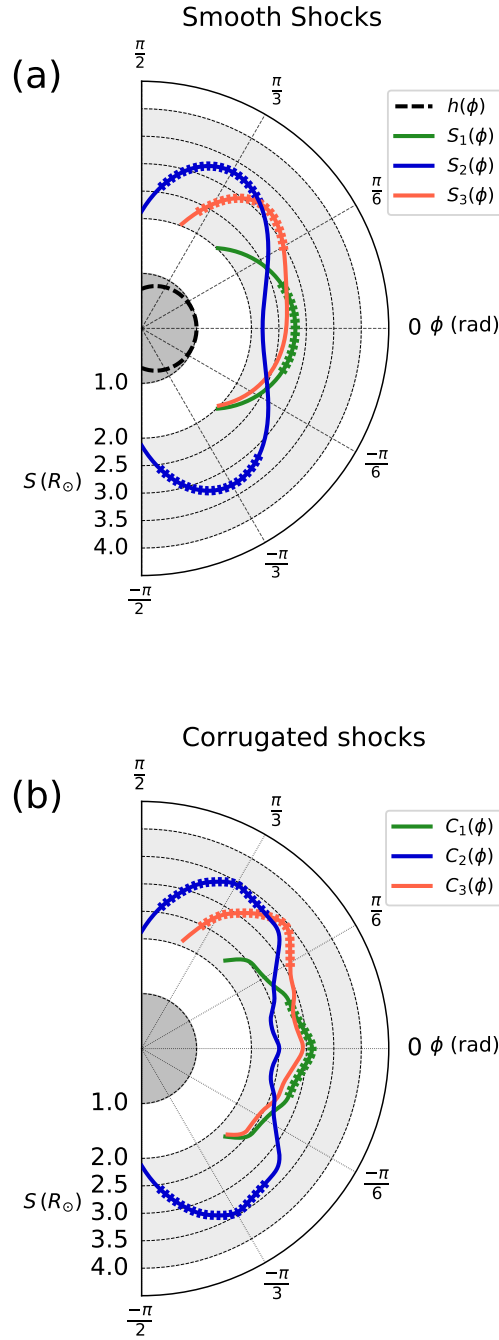


Figure 5.2: Reconstruction of the shocks shapes presented in Figure 5.1. Panel (a) shows the function $h(\phi)$ (black dashed line) Equation (5.1), together with the smooth shocks $S_1(\phi)$ (green line), $S_2(\phi)$ (blue line), and $S_3(\phi)$ (orange line), Equations (5.2), (5.4), and (5.5), respectively. In panel (b) we show the corrugated shocks $C_1(\phi)$ (green line), $C_2(\phi)$ (blue line) and $C_3(\phi)$ (orange line), Equation (5.6). The gray shadow between 2.0 to 4.0 R_\odot corresponds to the region where the shock are analyzed. In this interval we considerate the shock formation ($\sim 1.5 R_\odot$, e.g., Ma et al. 2011; Zucca et al. 2014; Gopalswamy et al. 2016) and particle acceleration ($\sim 3.0 R_\odot$, e.g., Reames 2009; Gopalswamy et al. 2012). For both shocks types we classify the quasi-parallel and quasi-perpendicular regions in order to understand the shock predisposition for particle acceleration and turbulence in the upstream shock region. The green, blue, and orange transverse lines at convex (rounded) regions indicate the locations where we assumed the supercritical shock conditions (e.g., Bemporad and Mancuso, 2011; Bemporad et al., 2014). The gray half-circle represents the Sun. Source: Páez et al. (2018).

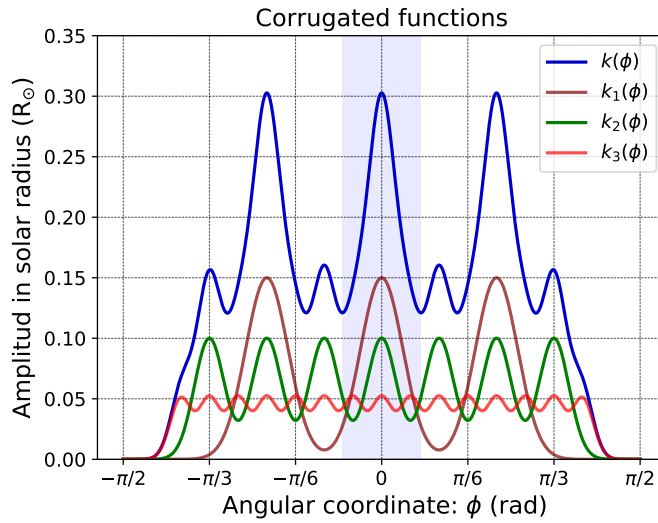


Figure 5.3: Corrugated function $k(\phi)$ (R_{\odot}), Equation (5.7) (blue line), and its contributions $k_1(\phi)$, Equation (5.8) (maroon line), $k_2(\phi)$, Equation (5.9) (green line); and $k_3(\phi)$, Equation (5.10) (red line) as function of polar angle coordinate, ϕ . The $k(\phi)$ function is imposed on smooth shocks $S_m(\phi)$, Equations (5.2), (5.4), and (5.5), in order to construct the corrugated shock, $C_m(\phi)$, Equation (5.6). The blue shadow indicate the amplitude of $0.3 R_{\odot}$ and angular width $\sim \pi/6$ rad ($\sim 30^\circ$) of the larger undulations. Source: Páez et al. (2018).

radial drag force of the SW background allow latitudinal and longitudinal CME deflections Kay et al. (2013, 2015). The CME deflection and rotations are established from $2.0 R_{\odot}$, early CME evolution stages (Kay and Opher, 2015). Present-day works evidence that fast CMEs are less deflected than the slow CMEs (e.g., Xie et al., 2009), and explained the CME deflection is consistent with the strength and direction with the gradient of magnetic energy density (e.g., Shen et al., 2011; Gui et al., 2011). Thus, the SW and CME deflections effects on ejecta may be, large angular undulations, possibly imposed by the decentralization of the shock with respect to the CME, or to the shock deformation comparable to the showed in Wood et al. (2012) and Kozarev et al. (2013).

Certainly, the shock preserve the most relevant features of the ejecta piston, which can be due to magnetic configurations and irregular CME expansions. Evans et al. (2011) show how the CME-pause that represent the boundary in equilibrium between CME and shocked coronal plasma can maintain an irregular shape. The authors explained it through of two different ways. First, they affirm that may be the result of magnetic field relative configurations among CME and the coronal and active region magnetic fields. Second, they suggest that may be due to the deflected flows in the downstream region, similarly to the heliosheath (e.g., Opher et al., 2007, 2009). The CMEs can be affected by their irregular expansion due to the imbalance among internal magnetic and gas pressure, together

Table 5.1 - Values of the constants a_i (R_\odot), and b_i (dimensionless) of the $p_m(\phi)$ function, Equation (5.3), in order to constructed the symmetric shocks 2 and 3.

i	0	1	2	3	4	5	6	7	8	9
shock 2										
a_i	0.0	0.0	0.0	0.0	0.0	0.0	0.6	1.0	0.7	0.3
b_i	0.0	0.0	0.0	0.0	0.0	0.0	2.1	3.0	0.7	5.0
shock 3										
a_i	0.0	0.0	0.0	0.3	0.2	0.4	0.7	0.0	0.0	0.0
b_i	0.0	0.0	0.0	0.0	7.0	5.0	7.0	0.0	0.0	0.0

to external pressures of solar corona. It may allow that some CME regions expanded more rapidly than others by dynamical pressure effects. Besides of the previous assumptions, the ubiquitous irregularities of the density and magnetic field in the solar corona allow fluctuations in the Alfvén velocity, therefore the shock front may be modified (e.g., Warmuth and Mann, 2005; Evans et al., 2008; Zucca et al., 2014).

In this paper we do not take into account the CMEs rotations (e.g., Lynch et al., 2009; Yurchyshyn et al., 2009) in order of guarantee the shock coplanarity hypothesis (e.g., Balogh and Treumann, 2013). Also we neglected the CMEs interactions (e.g., Lugaz et al. 2017 and references therein), but we highlight that these may affect substantially the shock fronts as well.

The nature of the CMEs, solar corona, and SW, allow that disturbances on shock to be completely aleatory. Here, as a first approximation we model these disturbances through wave functions. Mathematically we define the corrugated shocks, $C_m(\phi)$, imposing tenuous undulations on smooth shocks $S_m(\phi)$ by addition of a supplementary function $k(\phi)$,

$$C_m(\phi) = S_m(\phi) + k(\phi). \quad (5.6)$$

The $k(\phi)$ is defined as the sum of smaller corrugated functions,

$$k(\phi) = k_1(\phi) + k_2(\phi) + k_3(\phi), \quad (5.7)$$

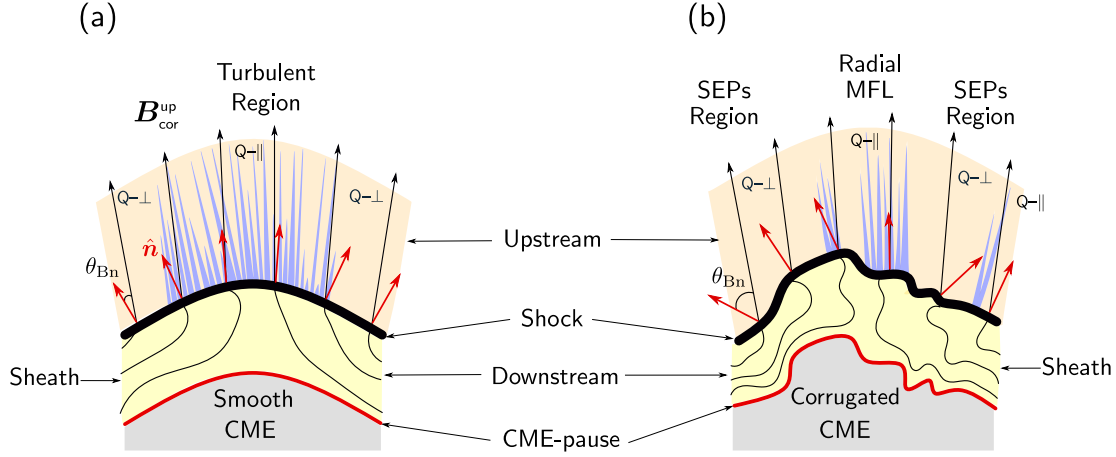


Figure 5.4: Schematic comparison between smooth, panel (a), and corrugated shocks, panel (b). We indicate the differences between CME piston (gray shadow), CME-pause (red line), downstream or sheath (yellow shadow), upstream (orange shadow) of the shock (black thick arrows), and distribution of the shock normal vectors (\hat{n} , red arrows). For both cases we assume the coronal magnetic field lines (MFL) (black thin arrows) turbulent disposed in the sheath region and radially in the upstream region. We classify the quasi-parallel (Q-||) and quasi-perpendicular (Q-⊥) regions by calculation of the shock normal angle, θ_{Bn} , between shock normal, \hat{n} , and the radial upstream coronal magnetic field, (B_{cor}^{up}). Our results for the smooth and corrugated shock in Figure 5.5 are illustrated by irregular distributions filamentary structures (blue structures) in the Q-|| upstream regions. Source: Páez et al. (2018).

where,

$$k_1(\phi) = \sum_{i=-1}^1 0.15 \exp \left[-30 \left(\phi - \frac{2i\pi}{9} \right)^2 \right], \quad (5.8)$$

$$k_2(\phi) = \sum_{i=-3}^3 0.1 \exp \left[-60 \left(\phi - \frac{i\pi}{9} \right)^2 \right], \quad (5.9)$$

and,

$$k_3(\phi) = \sum_{i=-7}^7 0.05 \exp \left[-120 \left(\phi - \frac{i\pi}{18} \right)^2 \right]. \quad (5.10)$$

Figure 5.3 shows the function $k(\phi)$ (blue line), $k_1(\phi)$ (maroon line), $k_2(\phi)$ (green line), and the $k_3(\phi)$ (red line). The $k_1(\phi)$ function, Equation (5.8), is intentionally structured with three wave crest, in order to assume the disturbances on shock caused by the SW interfaces together with the fast and slow SW. With $k_2(\phi)$ function, Equation (5.9),

we represent the disturbances due to the irregular CME expansion. In $k_3(\phi)$ function, Equation (5.10), we have into account the minor disturbances in the shock induced by fluctuations in the density, Alfvén velocity or magnetic field strength of the solar corona. The amplitudes of the $k_1(\phi)$ ($\sim 15\% R_\odot$), $k_2(\phi)$ ($\sim 10\% R_\odot$), and $k_3(\phi)$ ($\sim 5\% R_\odot$) compose a corrugated function $k(\phi)$ with maximum amplitude of $30\% R_\odot$ and crest angular width of the $\sim \pi/6$ rad ($\sim 30^\circ$) indicated by the blue shadow. In Figure 5.2(b) we show the $C_1(\phi)$ (green line), $C_2(\phi)$ (blue line) and $C_3(\phi)$ (orange line).

5.2 Calculation

In order to understand the shock predisposition to particle acceleration and turbulent phenomena, we compare the distributions of quasi-parallel and quasi-perpendicular regions along of the smooth and corrugated shocks, see Figures 5.1 and 5.2. We identify these regions by calculating the shock normal angle, θ_{Bn} , between the shock normal, $\hat{\mathbf{n}}$, and the upstream coronal magnetic field, \mathbf{B}^{up} . We assume a steady global coronal magnetic field with open magnetic field lines in the polar regions and closed field lines in the low latitudes of the equator, besides we consider the bimodal structure of the SW (e.g., Manchester et al., 2004). For distances larger than the source surface radius, in our calculation at $2.5 R_\odot$ (e.g., Altschuler and Newkirk, 1969), we consider the \mathbf{B}^{up} disposed radially in the pre-shock or upstream region (e.g., Bemporad et al. 2014 and references therein).

In Figures 5.4(a) and (b) we compare the smooth and corrugated shocks (black thick lines) and CMEs piston (gray shadow), CME-pause (red line), sheath or downstream (yellow shadow), upstream (orange shadow), and the angles θ_{Bn} , between $\hat{\mathbf{n}}$ (red arrows), and \mathbf{B}^{up} (black thin arrows). In the corrugated shock, we characterize the undulations with a lower amplitude than in the CME piston, and illustrate the turbulent sheath by the irregular downstream magnetic field lines. The unlike distribution of regions quasi-parallel (blue upstream filamentary structures) and quasi-perpendicular regions illustrating our results are shown in Figure 5.5 for both shocks types.

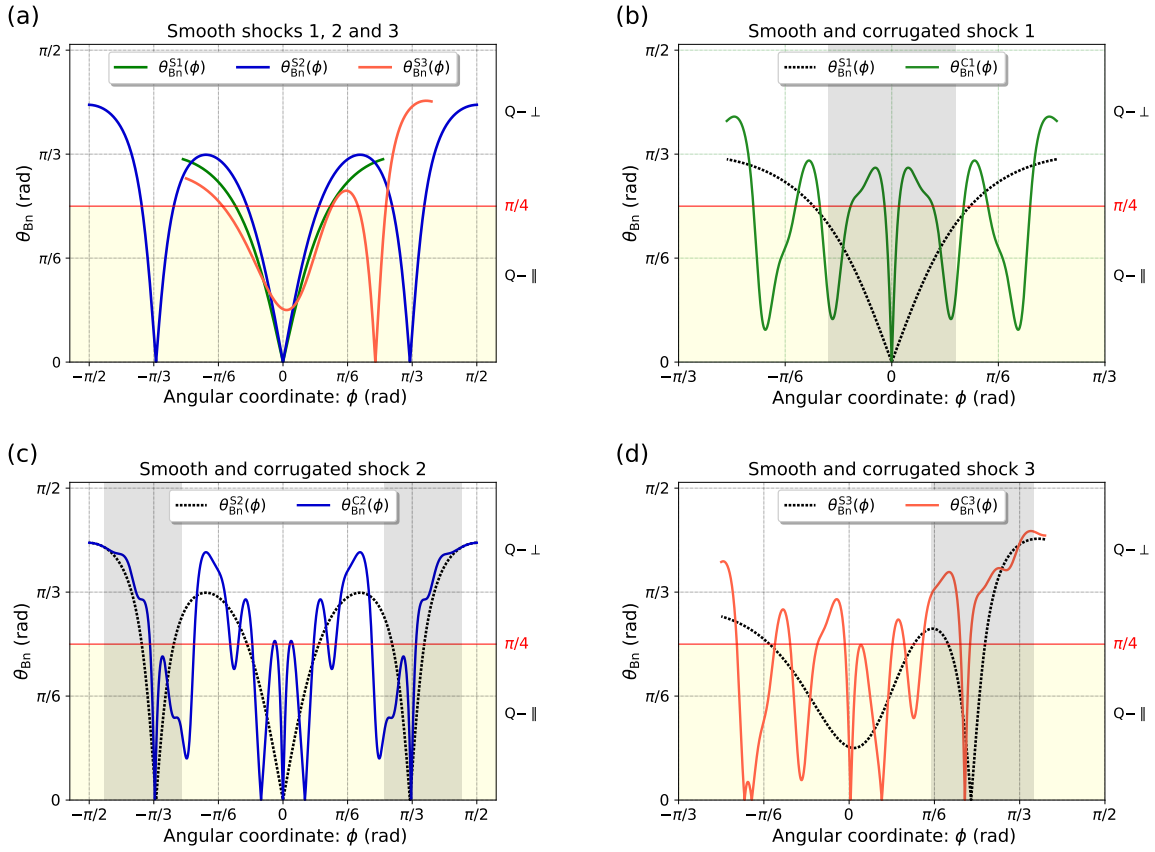


Figure 5.5: Plots of shock normal angles for smooth, $\theta_{Bn}^{Sm}(\phi)$, and corrugated $\theta_{Bn}^{Cm}(\phi)$ shocks, with $m = 1, 2, 3$, see Figure 5.2. Panel (a) shows the θ_{Bn} values for the three smooth shocks, and panels (b), (c) and (d) show separately the $\theta_{Bn}^{Sm}(\phi)$ (black dotted line), and $\theta_{Bn}^{Cm}(\phi)$ (color continuous line) values for each one of the shocks. The plots are associated to the color features in Figures 5.1 and 5.2, i.e., the shocks 1, 2, 3 in green, blue and orange, respectively. The quasi-parallel (Q-||, $0 \leq \theta_{Bn} < \pi/4$) and quasi-perpendicular (Q-⊥, $\pi/4 \leq \theta_{Bn} < \pi/2$) regions around the shocks are indicated by yellow and white background shadow colors separated by red line of $\theta = \pi/4$ rad. The gray shadows in the plots indicate the initial supercritical regions assumed from Figure 5.2. The results between smooth and corrugated shocks are illustrated in the Figure 5.4 by distributions of filamentary structures in the upstream regions for quasi-parallel θ_{Bn} values. Source: Páez et al. (2018).

5.2.1 Shock normal angles calculation

We calculated the angles, θ_{Bn} between the normal of the shock, $\hat{\mathbf{n}}$, and radial magnetic field, $\mathbf{B}^{\text{up}} = \|\mathbf{B}^{\text{up}}\| \hat{\mathbf{r}}$, along the shock,

$$\cos \theta_{\text{Bn}} = \frac{\hat{\mathbf{n}} \cdot \mathbf{B}^{\text{up}}}{\|\mathbf{B}^{\text{up}}\|} = \hat{\mathbf{n}} \cdot \hat{\mathbf{r}}. \quad (5.11)$$

We introduce $\hat{\mathbf{n}}$, by rotating the tangential vector to the shock, $\boldsymbol{\tau}$. This process consists of three steps: first, we define the shock surface, $S(\phi)$ (also corrugated shocks, $C_m(\phi)$ Equation (5.6)), as a parametric function ($\langle \rangle$) of ϕ , i.e.,

$$S(\phi) = \langle \phi, S \rangle. \quad (5.12)$$

Second, we calculate the tangential vector, in polar components ($, \hat{\mathbf{r}}$),

$$\boldsymbol{\tau} = +S_\phi \hat{\mathbf{r}}, \quad (5.13)$$

with $S_\phi = \frac{dS}{d\phi}$. Third, we rotate $\pi/2$ rad, in order to find the unitary normal vector ($\hat{\mathbf{n}}$),

$$\hat{\mathbf{n}} = \frac{-S_\phi + \hat{\mathbf{r}}}{(S_\phi^2 + 1)^{\frac{1}{2}}}. \quad (5.14)$$

With Equations (5.11) and (5.14), we find the angle θ_{Bn} ,

$$\theta_{\text{Bn}} = \arccos (S_\phi^2 + 1)^{-\frac{1}{2}} \text{ rad}. \quad (5.15)$$

Figure 5.5 shows the shock normal angles plots for the smooth, $\theta_{\text{Bn}}^{\text{Sm}}(\phi)$, and the corrugated $\theta_{\text{Bn}}^{\text{Cm}}(\phi)$ shocks, with $m = 1, 2, 3$, see Figure 5.2. Panel (a) shows the θ_{Bn} values for the three smooth shocks, and panels (b), (c) and (d) show separately the $\theta_{\text{Bn}}^{\text{Sm}}(\phi)$ (black dotted line), and $\theta_{\text{Bn}}^{\text{Cm}}(\phi)$ (colored continuous line) plots. The color plots are associated with the color feature presented in this paper, i.e., the shock 1, 2, 3 in green, blue and orange, respectively. The yellow and white background shadows indicate the quasi-parallel (Q-||, $0 \leq \theta_{\text{Bn}} \leq \pi/4$) and quasi-perpendicular (Q-⊥, $\pi/4 \leq \theta_{\text{Bn}} \leq \pi/2$) ranges of θ_{Bn} .

In Figure 5.5(a), the angle $\theta_{\text{Bn}}^{\text{S1}}(\phi)$ (green line) oscillates from quasi-perpendicular to parallel angles between flanks to the nose of the $S_1(\phi)$ (green line in Figure 5.2). In this

case there is only one point where the shock is completely parallel, i.e., $\theta_{\text{Bn}} = 0$ rad. The $\theta_{\text{Bn}}^{\text{S}2}(\phi)$ (blue line) varies from quasi-perpendicular in shock flanks to the quasi-parallel values through the shock width. Unlike of the $\theta_{\text{Bn}}^{\text{S}1}(\phi)$, the $\theta_{\text{Bn}}^{\text{S}2}(\phi)$ presents three points where the shock is parallel. The $\theta_{\text{Bn}}^{\text{S}3}(\phi)$ (orange line) preserve similar features to the $\theta_{\text{Bn}}^{\text{S}1}(\phi)$, and shows a similar behavior to the $\theta_{\text{Bn}}^{\text{S}2}(\phi)$ in latitudes $> \pi/6$, the differences are consequence of their unlike shock surfaces. For the three shock cases we do not find θ_{Bn} angles of perpendicular cases, i.e., $\theta_{\text{Bn}} = \pi/2$ rad.

From previous remarks two findings can be considered between $S_m(\phi)$ and $\theta_{\text{Bn}}^{\text{S}m}(\phi)$. The first, suggest that shock shape may be interpreted as a composition of convex (outward curve) and concave (inward curve) regions like $S_1(\phi)$, consequently its $\theta_{\text{Bn}}^{\text{S}m}(\phi)$ profiles also may be a composition of $\theta_{\text{Bn}}^{\text{S}1}(\phi)$. This can be inferred by comparing the shock 1 and shock 2. The $S_1(\phi)$ profile shows a convex profile and consequently its $\theta_{\text{Bn}}^{\text{S}1}(\phi)$ exhibit a plot a “V” shape. In the same way, the $S_2(\phi)$ may be interpreted like a composition of convex and concave regions of $\sim \pi/3$ rad width each one. Consequently the $\theta_{\text{Bn}}^{\text{S}2}(\phi)$ is structured through three “V” profiles in $\pm\pi/3$ and 0 rad. As given above, $\theta_{\text{Bn}}^{\text{S}2}(\phi)$ may be assumed like a composition of $\theta_{\text{Bn}}^{\text{S}1}(\phi)$, where the differences are imposed from different angular width in the convex and concave regions of $S_2(\phi)$. The second finding, is an interesting behavior between shock 1 and shock 3. Figure 5.2(a) shows the $S_3(\phi)$ like a deflection of the $S_1(\phi)$. This like-deflection effect may be consider in Figure 5.5(a) likes an angular translation of $\theta_{\text{Bn}}^{\text{S}3}(\phi)$ with respect to $\theta_{\text{Bn}}^{\text{S}1}(\phi)$. The $\theta_{\text{Bn}}^{\text{S}3}(\phi)$ shows some differences for $\phi < \pi/6$ rad due to the variations in amplitude of the convex region of $S_3(\phi)$ with respect to $S_1(\phi)$.

Figures 5.5(b), (c) and (d) show the effects of the wave-like features of $k(\phi)$, Equation (5.7), on the smooth shocks by comparing the $\theta_{\text{Bn}}^{\text{C}m}(\phi)$ (colored continuous lines) and $\theta_{\text{Bn}}^{\text{S}m}(\phi)$ (black dotted lines). The $C_m(\phi)$ and $\theta_{\text{Bn}}^{\text{C}m}(\phi)$ do not show constraints similar to the previous affirmations for the smooth shock. Besides, the small amplitude of $k(\phi)$, i.e., $\leq 0.3 R_{\odot}$, affect drastically to the θ_{Bn} values. The most visible differences between $\theta_{\text{Bn}}^{\text{S}m}(\phi)$ and $\theta_{\text{Bn}}^{\text{C}m}(\phi)$ are the consecutive changes of θ_{Bn} and extreme values in $\theta_{\text{Bn}}^{\text{C}m}(\phi)$. The undulations notably multiply the parallel angles, i.e., $\theta_{\text{Bn}} \approx 0$ rad, along the shocks width, but do not allow the existence of the perpendicular angles, the last similar to the smooth shocks.

5.3 Discussion and conclusions

The CME-driven shock formation in the low corona is a phenomenon that involves several physical processes as particle acceleration (e.g., Manchester et al., 2005; Kozarev et al., 2013), and turbulence. Recently, some works show the relevance of including realistic features of the solar corona and CMEs in studies of SEPs (e.g., Schwadron et al., 2015; Petukhova et al., 2017; Kong et al., 2017). In this work, we discuss the SEPs and turbulence regions on shocks with wave-like features imposed from ubiquitous disturbances of the solar corona, SW, and the corrugated CME piston. These wavy shocks are known as corrugated shocks (e.g., Gardner and Kruskal, 1964; Landau and Lifshitz, 1987). This paper was motivated from observations showed in Susino et al. (2015), where the authors show an irregular shock front between 2 to 12 R_{\odot} and 110° angular width. Also, a similar shock front is evidenced in Bemporad and Mancuso (2011), Bemporad and Mancuso (2013), and Bemporad et al. (2014) at $\sim 2.5 R_{\odot}$ distance, in the CME event of 1999 June 11. Our calculations are focused on the shock normal angle, θ_{Bn} , between the shock normal, $\hat{\mathbf{n}}$, Equation (5.14), and radial upstream coronal magnetic field lines, \mathbf{B}^{up} . The θ_{Bn} is the parameter that controls the physical process in the shock (e.g., Balogh and Treumann, 2013). With θ_{Bn} , we identify the quasi-parallel ($0 \leq \theta_{\text{Bn}} \leq \pi/4$) and the quasi-perpendicular ($\pi/4 \leq \theta_{\text{Bn}} \leq \pi/2$) regions, associated to particle acceleration and turbulence, respectively. We do not study the evolutionary process in the shock, in contrast, we analyze the shock at $\sim 3.0 R_{\odot}$, in order to understand the predisposition of injection of particles through θ_{Bn} , during the early stages of the shock.

In this paper, we analyze three different CME-driven shock morphologies from Ontiveros and Vourlidis (2009). In Figure 5.1, we show CME 1, CME 2 and CME 3, with respective shocks located in different latitudes i.e., CME nose (CME 1), both CMEs flanks (CME 2), and superior CME flank (CME 3). We define the smooth shocks $S_m(\phi)$, with $m = 1, 2, 3$, Equation (5.2), (5.4) and (5.5) through polar Gaussian plots as functions of the polar angular coordinate, ϕ , see Figure 5.2(a). The corrugated shock $C_m(\phi)$, Equation (5.6), showed in Figure 5.2(b), are defined from $S_m(\phi)$ in addition with a complementary function $k(\phi)$, Equation (5.7), shown in Figure 5.3. Our study is focused in $\sim 3.0 R_{\odot}$, according to the shock formation, i.e., $\sim 1.5 R_{\odot}$ (e.g., Ma et al., 2011; Zucca et al., 2014; Gopalswamy et al., 2016), and SEPs onset $\sim 3.0 R_{\odot}$ (e.g., Reames, 2009; Gopalswamy et al., 2012).

For this reason we assume an amplitude less than 30% R_{\odot} in $k(\phi)$. We consider that wavy features in shocks are consequence of the disturbances from SW medium and CME deflection ($k_1(\phi)$, Equation (5.8)), irregular CME expansions or initial configuration of the CME ($k_2(\phi)$, Equation (5.9)), and minor disturbances from the solar corona, e.g., due to the fluctuation of density and Alfvén speed ($k_3(\phi)$, Equation (5.10)).

For the case of the smooth shocks, we find constraints between the shocks surfaces and their θ_{Bn} angles. Shock shape can be written like a sum of convex and concave contributions, i.e., like a compound of the profile of shock 1, $S_1(\phi)$, Equation 5.2. Consequently its θ_{Bn} profile may be a combination of $\theta_{\text{Bn}}^{\text{S1}}(\phi)$. For a situation similar to the shock decentralization, possibly due to deflection of CME or effect of external factors like coronal hole (e.g., Wood et al., 2012), the θ_{Bn} can be written as the shock normal angles of shock non-decentralized, i.e., the maximum and minimum θ_{Bn} values may be preserved. Thereby the morphology of the $S_1(\phi)$ turns a crucial element for interpreting others complex shocks like shock 2, $S_2(\phi)$ Equation (5.4), and shock 3, $S_3(\phi)$ Equation (5.5). The main diagnostic in the corrugated shocks is the strong oscillation of θ_{Bn} through the polar angle ϕ . Figure 5.5 shows how the $\theta_{\text{Bn}}^{\text{Cm}}(\phi)$ changes drastically compared to the smooth shocks. The different amplitude and frequency in the components of $k(\phi)$ i.e., $k_1(\phi)$, $k_2(\phi)$ and $k_3(\phi)$, modify the θ_{Bn} profile of the smooth shocks. From Figure 5.3, the $k_2(\phi)$ function may be the most relevant source of disturbances in the shock. This function preserves intermediate amplitude and frequency values that $k_1(\phi)$ and $k_3(\phi)$, besides that represent the irregular shock features due to initial CMEs magnetic configurations and imbalance of magnetic pressures between CME and corona. Our results of $\theta_{\text{Bn}}^{\text{Cm}}(\phi)$ do not evidence some constraint similar to the smooth shock case. For the six shocks cases analyzed in this paper, we do not find perpendicular shock conditions i.e., $\theta_{\text{Bn}} = \pi/2$.

In this work, we do not study the evolution of the shock morphology, but Susino et al. (2015) observations, suggest that shock morphology evolution preserve the initial irregularities. In this way, the initial profile is a start point for analyzing the shock evolution. Moreover, if the most notable shock attributes are preserved, the quasi-parallel and quasi-perpendicular regions will also be conserved. With this hypothesis, the SEPs and turbulence region in the shock may be maintained in the shock front, possibly with exception in the angular width. Our idea of corrugated shocks evidence that the injection of particles through the shock may be complex due to the dependence of injection velocity

with θ_{Bn} (e.g., [Li et al., 2012](#); [Balogh and Treumann, 2013](#)). In this way, the disturbances from coronal medium and corrugated CME piston may modify completely the SEPs production along the shock.

We understand that the physics of the corrugated CME-driven shocks is more sophisticated than described here. The disturbances studied in this paper are aleatory phenomena that depend on several factors, as ubiquitous fluctuations of the CME and solar corona properties, or even solar cycle phase. Therefore, the perturbations on CME piston and shock, may be more complex than showed here. Adopting these wave-like features on the shocks, may be the started point for new research topics, in the sheath region, e.g., like the downstream-jets and secondary shock, similar to the detected in the magnetosheath ([Hietala et al., 2009](#); [Hietala and Plaschke, 2013](#)); sheath evolution process, e.g., like density variations and flows, e.g., Kelvin–Helmholtz instability ([Manchester et al., 2005](#)); particle acceleration in sheath region in high density regions (pile-up regions in [Das et al. 2011](#)) (e.g., [Kozarev et al., 2013](#)), shock thermalization, shock stability, injection particle process.

Conclusions and perspectives

In this thesis, we presented two studies related to coronal mass ejections (CMEs). In the first one, we studied the Kelvin–Helmholtz instability (KHI) at the CME–Sheath and Sheath–solar wind (SW) interfaces for two faster CMEs that propagate in the slow and fast SW. Unlike to the KHI observations in CMEs, we presented an analysis of the KHI in the outer corona distances between 4 to 30 R_{\odot} . This region may be more suitable for KHI, in comparison to the low corona, due to the lower magnetic field strength, larger velocities of the SW and CME, and simpler magnetic field configurations. In our study were mapped the densities, magnetic fields strength, and velocities of the slow and fast SW, and the sheath structure. With help of the [Chandrasekhar](#) and [Hasegawa](#) condition for magnetic KHI, we identify the suitable CME environment for KHI existence. Our results suggest that the CME propagating in the slow SW may be suitable for KHI formation due to larger shear velocities than in the fast SW. From two interfaces, we found that the interface between the sheath and SW can be even more proper for KHI formation than the interface between ejecta and sheath. We emphasized that flare associated to the CME may develop a crucial role in the KHI formation. The flare energy released can establish a denser sheath, or even to allow the shock and sheath formation in slow CMEs, in this sense the flare optimizes the CME environment toward the KHI.

The few KHI observations in CMEs can indicate two goals on the knowledge of this phenomenon. The first consist to know if the CME environments are predisposed to the KHI, and the second is related to the KHI evolution. Our work, evidenced the susceptibility to the KHI existence, particularly in regions of the slow SW, i.e., the KHI may be more common than the CME events registered. On the other hand, the KHI evolution may be imperceptible due to the limitations of the current technology, i.e., it would still not be

adequate for KHI detection. In order to improve the understanding of the KHI in the CMEs, it turns important further works with more CME parameters, and to take into account the flare associated to CME, and possible evolution of the KHI. We expect that through incoming instruments it can be acquired new KHI observations.

In the second study, we check the distribution of particle acceleration and turbulence regions on corrugated CME-driven shocks. These shocks maintain wavy features due to the disturbances from the solar corona, SW, CME deflection, irregular CME expansion, and minor disturbances due to fluctuations in density and magnetic field strength in corona. In this work, we analyzed the role of these features on the particle acceleration and turbulence process. For this reason, are modeled three different shocks morphology, where we imposed the undulations. We estimated the shock normal angle between the shock normal and upstream radial magnetic field. With this, is possible to interpret the shocks predisposition to particle acceleration. We found that for cases of shocks complex morphology the shock normal angles can be calculated from the most simple shock shape. In a similar way, the shock normal angles of the shocks decentralized, possibly due to the CME deflection, can be inferred of the shocks non-decentralized. The results show that wave-like features allow drastic oscillations of the shock normal angles which modify the physical process at the shock front. Our results suggest that the irregular expansion of the CMEs may be determinant in defining the physical process at the shock front.

We do not analyze the shock evolution, but through the observations, we consider that the irregular shock morphology can maintain the initial features. The disturbances in the shock formation range are totality aleatory, these even may depend on the solar cycle. In this way, the physical process involved in the corrugated shocks may be more complex that our description. We consider that to assume these irregularities on the CME-driven shocks may be the first step in order to solve questions related to instabilities, shock thermalization, acceleration of particles or even injection particles. In a future analysis of the corrugated shocks, we consider appropriate to reconstructed the shock morphology from low to outer corona. It may help to know the role of shock morphology and changes in supercritical and subcritical phases during shock propagation.

Bibliography

- Abbo L., Antonucci E., Mikić Z., Linker J. A., Riley P., Lionello R., Characterization of the slow wind in the outer corona, *Advances in Space Research*, 2010, vol. 46, p. 1400
- Altschuler M. D., Newkirk G., Magnetic Fields and the Structure of the Solar Corona. I: Methods of Calculating Coronal Fields, *Sol. Phys.*, 1969, vol. 9, p. 131
- Amerstorfer U. V., Erkaev N. V., Langmayr D., Biernat H. K., On Kelvin Helmholtz instability due to the solar wind interaction with unmagnetized planets, *Planet. Space Sci.*, 2007, vol. 55, p. 1811
- Asai A., Shibata K., Ishii T. T., Oka M., Kataoka R., Fujiki K., Gopalswamy N., Evolution of the anemone AR NOAA 10798 and the related geo-effective flares and CMEs, *Journal of Geophysical Research (Space Physics)*, 2009, vol. 114, p. A00A21
- Aschwanden M. J., Acton L. W., Temperature Tomography of the Soft X-Ray Corona: Measurements of Electron Densities, Temperatures, and Differential Emission Measure Distributions above the Limb, *ApJ*, 2001, vol. 550, p. 475
- Bain H. M., Krucker S., Glesener L., Lin R. P., Radio Imaging of Shock-accelerated Electrons Associated with an Erupting Plasmoid on 2010 November 3, *ApJ*, 2012, vol. 750, p. 44
- Balogh A., Treumann R. A., *Physics of Collisionless Shocks*, 2013
- Bell A. R., The acceleration of cosmic rays in shock fronts. I, *MNRAS*, 1978a, vol. 182, p. 147

- Bell A. R., The acceleration of cosmic rays in shock fronts. II, *MNRAS*, 1978b, vol. 182, p. 443
- Bemporad A., Mancuso S., Identification of Super- and Subcritical Regions in Shocks Driven by Coronal Mass Ejections, *ApJ*, 2011, vol. 739, p. L64
- Bemporad A., Mancuso S., Super- and sub-critical regions in shocks driven by radio-loud and radio-quiet CMEs, *JAdR*, 2013, vol. 4, p. 287
- Bemporad A., Susino R., Lapenta G., Plasma Physical Parameters along Coronal-mass-ejection-driven Shocks. I. Ultraviolet and White-light Observations, *ApJ*, 2014, vol. 784, p. 102
- Berné O., Marcelino N., Cernicharo J., Waves on the surface of the Orion molecular cloud, *Nature*, 2010, vol. 466, p. 947
- Berné O., Matsumoto Y., The Kelvin-Helmholtz Instability in Orion: A Source of Turbulence and Chemical Mixing, *ApJ*, 2012, vol. 761, p. L4
- Blandford R. D., Ostriker J. P., Particle acceleration by astrophysical shocks, *ApJ*, 1978, vol. 221, p. L29
- Borgazzi A., Lara A., Echer E., Alves M. V., Dynamics of coronal mass ejections in the interplanetary medium, *A&A*, 2009, vol. 498, p. 885
- Brueckner G. E., Howard R. A., Koomen M. J., Korendyke C. M., Michels D. J., Moses J. D., Socker D. G., Dere K. P., Lamy P. L., Llebaria A., Bout M. V., Schwenn R., Simnett G. M., Bedford D. K., Eyles C. J., The Large Angle Spectroscopic Coronagraph (LASCO), *Sol. Phys.*, 1995, vol. 162, p. 357
- Cargill P. J., On the Aerodynamic Drag Force Acting on Interplanetary Coronal Mass Ejections, *Sol. Phys.*, 2004, vol. 221, p. 135
- Carrington R. C., Description of a Singular Appearance seen in the Sun on September 1, 1859, *MNRAS*, 1859, vol. 20, p. 13
- Casanova J., José J., García-Berro E., Shore S. N., Calder A. C., Kelvin-Helmholtz instabilities as the source of inhomogeneous mixing in nova explosions, *Nature*, 2011, vol. 478, p. 490

-
- Cavus H., Kazkapan D., Magnetic Kelvin-Helmholtz instability in the solar atmosphere, *New A*, 2013, vol. 25, p. 89
- Chandrasekhar S., *Hydrodynamic and hydromagnetic stability*, 1961
- Chen J., Theory of prominence eruption and propagation: Interplanetary consequences, *J. Geophys. Res.*, 1996, vol. 101, p. 27499
- Chen J., Howard R. A., Brueckner G. E., Santoro R., Krall J., Paswaters S. E., St. Cyr O. C., Schwenn R., Lamy P., Simnett G. M., Evidence of an Erupting Magnetic Flux Rope: LASCO Coronal Mass Ejection of 1997 April 13, *ApJ*, 1997, vol. 490, p. L191
- Chen Y., Song H. Q., Li B., Xia L. D., Wu Z., Fu H., Li X., Streamer Waves Driven by Coronal Mass Ejections, *ApJ*, 2010, vol. 714, p. 644
- Cheng X., Zhang J., Liu Y., Ding M. D., Observing Flux Rope Formation During the Impulsive Phase of a Solar Eruption, *ApJ*, 2011, vol. 732, p. L25
- Coles W. A., Esser R., LÃvhaug U.-P., Markkanen J., Comparison of solar wind velocity measurements with a theoretical acceleration model, *J. Geophys. Res.*, 1991, vol. 96, p. 13849
- Collier Cameron A., Duncan D. K., Ehrenfreund P., Foing B. H., Kuntz K. D., Penston M. V., Robinson R. D., Soderblom D. R., Fast Spectroscopic Variations on Rapidly Rotating Cool Dwarfs - Part Three - Masses of Circumstellar Absorbing Clouds on Ab-Doradus, *MNRAS*, 1990, vol. 247, p. 415
- Cremades H., Bothmer V., On the three-dimensional configuration of coronal mass ejections, *A&A*, 2004, vol. 422, p. 307
- Cremades H., Bothmer V., Tripathi D., Properties of structured coronal mass ejections in solar cycle 23, *Advances in Space Research*, 2006, vol. 38, p. 461
- Das I., Opher M., Evans R., Loesch C., Gombosi T. I., Evolution of Piled-up Compressions in Modeled Coronal Mass Ejection Sheaths and the Resulting Sheath Structures, *ApJ*, 2011, vol. 729, p. 112
- Davenport J. R. A., The Kepler Catalog of Stellar Flares, *ApJ*, 2016, vol. 829, p. 23

- Dere K. P., Brueckner G. E., Howard R. A., Michels D. J., Delaboudiniere J. P., LASCO and EIT Observations of Helical Structure in Coronal Mass Ejections, *ApJ*, 1999, vol. 516, p. 465
- Desai M., Giacalone J., Large gradual solar energetic particle events, *Living Reviews in Solar Physics*, 2016, vol. 13, p. 3
- Ding L., Jiang Y., Zhao L., Li G., The “Twin-CME” Scenario and Large Solar Energetic Particle Events in Solar Cycle 23, *ApJ*, 2013, vol. 763, p. 30
- Domingo V., Fleck B., Poland A. I., The SOHO Mission: an Overview, *Sol. Phys.*, 1995, vol. 162, p. 1
- Dulk G. A., McLean D. J., Coronal magnetic fields, *Sol. Phys.*, 1978, vol. 57, p. 279
- Echer E., Gonzalez W. D., Guarnieri F. L., Lago A. D., Vieira L. E. A., Introduction to space weather, *Advances in Space Research*, 2005, vol. 35, p. 855
- Edmiston J. P., Kennel C. F., A parametric survey of the first critical Mach number for a fast MHD shock, *Journal of Plasma Physics*, 1984, vol. 32, p. 429
- Emslie A. G., Kucharek H., Dennis B. R., Gopalswamy N., Holman G. D., Share G. H., Vourlidas A., Forbes T. G., Gallagher P. T., Mason G. M., Metcalf T. R., Mewaldt R. A., Murphy R. J., Schwartz R. A., Zurbuchen T. H., Energy partition in two solar flare/CME events, *Journal of Geophysical Research (Space Physics)*, 2004, vol. 109, p. A10104
- Estrela R., Valio A., Stellar Magnetic Cycles in the Solar-like Stars Kepler-17 and Kepler-63, *ApJ*, 2016, vol. 831, p. 57
- Evans R. M., Opher M., Gombosi T. I., Learning from the Outer Heliosphere: Interplanetary Coronal Mass Ejection Sheath Flows and the Ejecta Orientation in the Lower Corona, *ApJ*, 2011, vol. 728, p. 41
- Evans R. M., Opher M., Manchester IV W. B., Gombosi T. I., Alfvén Profile in the Lower Corona: Implications for Shock Formation, *ApJ*, 2008, vol. 687, p. 1355
- Feng L., Inhester B., Gan W. Q., Kelvin-Helmholtz Instability of a Coronal Streamer, *ApJ*, 2013, vol. 774, p. 141

-
- Fermo R. L., Opher M., Drake J. F., Magnetic Reconnection in the Interior of Interplanetary Coronal Mass Ejections, *Physical Review Letters*, 2014, vol. 113, p. 031101
- Forbes T. G., A review on the genesis of coronal mass ejections, *J. Geophys. Res.*, 2000, vol. 105, p. 23153
- Forbush S. E., Three Unusual Cosmic-Ray Increases Possibly Due to Charged Particles from the Sun, *Physical Review*, 1946, vol. 70, p. 771
- Foullon C., Verwichte E., Nakariakov V. M., Nykyri K., Farrugia C. J., Magnetic Kelvin-Helmholtz Instability at the Sun, *ApJ*, 2011, vol. 729, p. L8
- Foullon C., Verwichte E., Nykyri K., Aschwanden M. J., Hannah I. G., Kelvin-Helmholtz Instability of the CME Reconnection Outflow Layer in the Low Corona, *ApJ*, 2013, vol. 767, p. 170
- Fox N. J., Velli M. C., Bale S. D., Decker R., Driesman A., Howard R. A., Kasper J. C., Kinison J., Kusterer M., Lario D., Lockwood M. K., McComas D. J., Raouafi N. E., Szabo A., The Solar Probe Plus Mission: Humanity's First Visit to Our Star, *Space Sci. Rev.*, 2016, vol. 204, p. 7
- Galarza J. Y., Meléndez J., Cohen J. G., Serendipitous discovery of the faint solar twin Inti 1, *A&A*, 2016, vol. 589, p. A65
- Gardner C. S., Kruskal M. D., Stability of Plane Magnetohydrodynamic Shocks, *Physics of Fluids*, 1964, vol. 7, p. 700
- Gary G. A., Plasma Beta above a Solar Active Region: Rethinking the Paradigm, *Sol. Phys.*, 2001, vol. 203, p. 71
- Gilbert H. R., Serex E. C., Holzer T. E., MacQueen R. M., McIntosh P. S., Narrow Coronal Mass Ejections, *ApJ*, 2001, vol. 550, p. 1093
- Gillon M., Triaud A. H. M. J., Demory B.-O., Jehin E., Agol E., Deck K. M., Lederer S. M., de Wit J., Burdanov A., Ingalls J. G., Bolmont E., Leconte J., Raymond S. N., Selsis F., Turbet M., Barkaoui K., Burgasser A., et al. Seven temperate terrestrial planets around the nearby ultracool dwarf star TRAPPIST-1, *Nature*, 2017, vol. 542, p. 456

- Gopalswamy N., Mäkelä P., Xie H., Akiyama S., Yashiro S., CME interactions with coronal holes and their interplanetary consequences, *JGRA*, 2009, vol. 114, p. A00A22
- Gopalswamy N., Mäkelä P., Xie H., Akiyama S., Yashiro S., Solar Sources of “Driverless” Interplanetary Shocks, Twelfth International Solar Wind Conference, 2010, vol. 1216, p. 452
- Gopalswamy N., Xie H., Yashiro S., Akiyama S., Mäkelä P., Usoskin I. G., Properties of Ground Level Enhancement Events and the Associated Solar Eruptions During Solar Cycle 23, *Space Sci. Rev.*, 2012, vol. 171, p. 23
- Gopalswamy N., Yashiro S., The Strength and Radial Profile of the Coronal Magnetic Field from the Standoff Distance of a Coronal Mass Ejection-driven Shock, *ApJ*, 2011, vol. 736, p. L17
- Gopalswamy N., Yashiro S., Kaiser M. L., Howard R. A., Bougeret J.-L., Radio Signatures of Coronal Mass Ejection Interaction: Coronal Mass Ejection Cannibalism?, *ApJ*, 2001, vol. 548, p. L91
- Gopalswamy N., Yashiro S., Krucker S., Stenborg G., Howard R. A., Intensity variation of large solar energetic particle events associated with coronal mass ejections, *Journal of Geophysical Research (Space Physics)*, 2004, vol. 109, p. A12105
- Gopalswamy N., Yashiro S., Thakur N., Mäkelä P., Xie H., Akiyama S., The 2012 July 23 Backside Eruption: An Extreme Energetic Particle Event?, *ApJ*, 2016, vol. 833, p. 216
- Gui B., Shen C., Wang Y., Ye P., Liu J., Wang S., Zhao X., Quantitative Analysis of CME Deflections in the Corona, *Sol. Phys.*, 2011, vol. 271, p. 111
- Hasegawa A., Plasma Instabilities and Nonlinear Effects, *Physics and Chemistry in Space*, 1975, vol. 8
- Hasegawa H., Fujimoto M., Phan T.-D., Rème H., Balogh A., Dunlop M. W., Hashimoto C., TanDokoro R., Transport of solar wind into Earth’s magnetosphere through rolled-up Kelvin-Helmholtz vortices, *Nature*, 2004, vol. 430, p. 755

- Hietala H., Laitinen T. V., Andréevová K., Vainio R., Vaivads A., Palmroth M., Pulkkinen T. I., Koskinen H. E. J., Lucek E. A., Rème H., Supermagnetosonic Jets behind a Collisionless Quasiparallel Shock, *Physical Review Letters*, 2009, vol. 103, p. 245001
- Hietala H., Plaschke F., On the generation of magnetosheath highspeed jets by bow shock ripples, *Journal of Geophysical Research (Space Physics)*, 2013, vol. 118, p. 7237
- Hundhausen A. J., Sawyer C. B., House L., Illing R. M. E., Wagner W. J., Coronal mass ejections observed during the solar maximum mission - Latitude distribution and rate of occurrence, *J. Geophys. Res.*, 1984, vol. 89, p. 2639
- Illing R. M. E., Hundhausen A. J., Observation of a coronal transient from 1.2 to 6 solar radii, *J. Geophys. Res.*, 1985, vol. 90, p. 275
- Innes D. E., Cameron R. H., Fletcher L., Inhester B., Solanki S. K., Break up of returning plasma after the 7 June 2011 filament eruption by Rayleigh-Taylor instabilities, *A&A*, 2012, vol. 540, p. L10
- Isavnin A., Vourlidas A., Kilpua E. K. J., Three-Dimensional Evolution of Erupted Flux Ropes from the Sun ($2 - 20 R_{\odot}$) to 1 AU, *Sol. Phys.*, 2013, vol. 284, p. 203
- Isobe H., Miyagoshi T., Shibata K., Yokoyama T., Filamentary structure on the Sun from the magnetic Rayleigh-Taylor instability, *Nature*, 2005, vol. 434, p. 478
- Johns M., McCarthy P., Raybould K., Bouchez A., Farahani A., Filgueira J., Jacoby G., Shtetman S., Sheehan M., Giant Magellan Telescope: overview. In *Ground-based and Airborne Telescopes IV*, vol. 8444 of *Proc. SPIE*, 2012, p. 84441H
- Kahler S. W., The correlation between solar energetic particle peak intensities and speeds of coronal mass ejections: Effects of ambient particle intensities and energy spectra, *J. Geophys. Res.*, 2001, vol. 106, p. 20947
- Kahler S. W., Solar Energetic Particle Event Onsets: Far Backside Solar Sources and the East-West Hemispheric Asymmetry, *ApJ*, 2016, vol. 819, p. 105
- Kaiser M. L., Kucera T. A., Davila J. M., St. Cyr O. C., Guhathakurta M., Christian E., The STEREO Mission: An Introduction, *Space Sci. Rev.*, 2008, vol. 136, p. 5

- Karpen J. T., Dahlburg R. B., Davila J. M., The effects of Kelvin-Helmholtz instability on resonance absorption layers in coronal loops, *ApJ*, 1994, vol. 421, p. 372
- Kay C., dos Santos L. F. G., Opher M., Constraining the Masses and the Non-radial Drag Coefficient of a Solar Coronal Mass Ejection, *ApJ*, 2015, vol. 801, p. L21
- Kay C., Opher M., The Heliocentric Distance where the Deflections and Rotations of Solar Coronal Mass Ejections Occur, *ApJ*, 2015, vol. 811, p. L36
- Kay C., Opher M., Evans R. M., Forecasting a Coronal Mass Ejection's Altered Trajectory: ForeCAT, *ApJ*, 2013, vol. 775, p. 5
- Kay C., Opher M., Evans R. M., Global Trends of CME Deflections Based on CME and Solar Parameters, *ApJ*, 2015, vol. 805, p. 168
- Kilpua E. K. J., Pomoell J., Vourlidis A., Vainio R., Luhmann J., Li Y., Schroeder P., Galvin A. B., Simunac K., STEREO observations of interplanetary coronal mass ejections and prominence deflection during solar minimum period, *AnGeo*, 2009, vol. 27, p. 4491
- Kivelson M. G., Pu Z.-Y., The Kelvin-Helmholtz instability on the magnetopause, *Planet. Space Sci.*, 1984, vol. 32, p. 1335
- Kivelson M. G., Russell C. T., *Introduction to Space Physics*, 1995, 586
- Kong X., Guo F., Giacalone J., Li H., Chen Y., The Acceleration of High-energy Protons at Coronal Shocks: The Effect of Large-scale Streamer-like Magnetic Field Structures, *ApJ*, 2017, vol. 851, p. 38
- Kozarev K. A., Evans R. M., Schwadron N. A., Dayeh M. A., Opher M., Korreck K. E., van der Holst B., Global Numerical Modeling of Energetic Proton Acceleration in a Coronal Mass Ejection Traveling through the Solar Corona, *ApJ*, 2013, vol. 778, p. 43
- Landau L. D., Lifshitz E. M., *Fluid mechanics*, 1987
- Lemen J. R., Title A. M., Akin D. J., Boerner P. F., Chou C., Drake J. F., Duncan D. W., Edwards C. G., Friedlaender F. M., Heyman G. F., Hurlburt N. E., Katz N. L., Kushner G. D., Levay M., Lindgren R. W., Mathur D. P., et al. *The Atmospheric Imaging*

- Assembly (AIA) on the Solar Dynamics Observatory (SDO), *Sol. Phys.*, 2012, vol. 275, p. 17
- Li G., Moore R., Mewaldt R. A., Zhao L., Labrador A. W., A Twin-CME Scenario for Ground Level Enhancement Events, *Space Sci. Rev.*, 2012, vol. 171, p. 141
- Li G., Shalchi A., Ao X., Zank G., Verkhoglyadova O. P., Particle acceleration and transport at an oblique CME-driven shock, *AdSpR*, 2012, vol. 49, p. 1067
- Li G., Zank G. P., Mixed particle acceleration at CME-driven shocks and flares, *Geophys. Res. Lett.*, 2005, vol. 32, p. L02101
- Lin J., CME-Flare Association Deduced from Catastrophic Model of CMEs, *Sol. Phys.*, 2004, vol. 219, p. 169
- Lites B. W., Akin D. L., Card G., Cruz T., Duncan D. W., Edwards C. G., Elmore D. F., Hoffmann C., Katsukawa Y., Katz N., Kubo M., Ichimoto K., Shimizu T., Shine R. A., Streander K. V., Suematsu A., Tarbell T. D., Title A. M., Tsuneta S., The Hinode Spectro-Polarimeter, *Sol. Phys.*, 2013, vol. 283, p. 579
- Liu C., Lee J., Karlický M., Prasad Choudhary D., Deng N., Wang H., Successive Solar Flares and Coronal Mass Ejections on 2005 September 13 from NOAA AR 10808, *ApJ*, 2009, vol. 703, p. 757
- Liu Y., Halo Coronal Mass Ejections and Configuration of the Ambient Magnetic Fields, *ApJ*, 2007, vol. 654, p. L171
- Liu Y., Hayashi K., The 2003 October-November Fast Halo Coronal Mass Ejections and the Large-Scale Magnetic Field Structures, *ApJ*, 2006, vol. 640, p. 1135
- Liu Y., Luhmann J. G., Lin R. P., Bale S. D., Vourlidas A., Petrie G. J. D., Coronal Mass Ejections and Global Coronal Magnetic Field Reconfiguration, *ApJ*, 2009, vol. 698, p. L51
- Liu Y., Richardson J. D., Belcher J. W., A statistical study of the properties of interplanetary coronal mass ejections from 0.3 to 5.4 AU, *Planet. Space Sci.*, 2005, vol. 53, p.

- Low B. C., Coronal mass ejections, magnetic flux ropes, and solar magnetism, *J. Geophys. Res.*, 2001, vol. 106, p. 25141
- Lugaz N., Downs C., Shibata K., Roussev I. I., Asai A., Gombosi T. I., Numerical Investigation of a Coronal Mass Ejection from an Anemone Active Region: Reconnection and Deflection of the 2005 August 22 Eruption, *ApJ*, 2011, vol. 738, p. 127
- Lugaz N., Temmer M., Wang Y., Farrugia C. J., The Interaction of Successive Coronal Mass Ejections: A Review, *Sol. Phys.*, 2017, vol. 292, p. 64
- Lynch B. J., Antiochos S. K., Li Y., Luhmann J. G., DeVore C. R., Rotation of Coronal Mass Ejections during Eruption, *ApJ*, 2009, vol. 697, p. 1918
- Ma S., Raymond J. C., Golub L., Lin J., Chen H., Grigis P., Testa P., Long D., Observations and Interpretation of a Low Coronal Shock Wave Observed in the EUV by the SDO/AIA, *ApJ*, 2011, vol. 738, p. 160
- MacQueen R. M., Hundhausen A. J., Conover C. W., The propagation of coronal mass ejection transients, *J. Geophys. Res.*, 1986, vol. 91, p. 31
- Magdalenic J., Marqué C., Zhukov A. N., Vršnak B., Žic T., Origin of Coronal Shock Waves Associated with Slow Coronal Mass Ejections, *ApJ*, 2010, vol. 718, p. 266
- Magdalenic J., Vršnak B., Pohjolainen S., Temmer M., Aurass H., Lehtinen N. J., A Flare-Generated Shock during a Coronal Mass Ejection on 24 December 1996, *Sol. Phys.*, 2008, vol. 253, p. 305
- Manchester W. B., Gombosi T. I., Roussev I., de Zeeuw D. L., Sokolov I. V., Powell K. G., Tóth G., Opher M., Three-dimensional MHD simulation of a flux rope driven CME, *J. Geophys. Res.*, 2004, vol. 109, p. 1102
- Manchester IV W. B., Gombosi T. I., De Zeeuw D. L., Sokolov I. V., Roussev I. I., Powell K. G., Kóta J., Tóth G., Zurbuchen T. H., Coronal Mass Ejection Shock and Sheath Structures Relevant to Particle Acceleration, *ApJ*, 2005, vol. 622, p. 1225
- Mancuso S., Raymond J. C., Kohl J., Ko Y.-K., Uzzo M., Wu R., UVCS/SOHO observations of a CME-driven shock: Consequences on ion heating mechanisms behind a coronal shock, *A&A*, 2002, vol. 383, p. 267

-
- Mann G., Klassen A., Aurass H., Classen H.-T., Formation and development of shock waves in the solar corona and the near-Sun interplanetary space, *A&A*, 2003, vol. 400, p. 329
- Maričić D., Vršnak B., Stanger A. L., Veronig A. M., Temmer M., Roša D., Acceleration Phase of Coronal Mass Ejections: II. Synchronization of the Energy Release in the Associated Flare, *Sol. Phys.*, 2007, vol. 241, p. 99
- Markevitch M., Gonzalez A. H., David L., Vikhlinin A., Murray S., Forman W., Jones C., Tucker W., A Textbook Example of a Bow Shock in the Merging Galaxy Cluster 1E 0657-56, *ApJ*, 2002, vol. 567, p. L27
- Martínez-Núñez S., Kretschmar P., Bozzo E., Oskinova L. M., Puls J., Sidoli L., Sundqvist J. O., Blay P., Falanga M., Fürst F., et al. Towards a Unified View of Inhomogeneous Stellar Winds in Isolated Supergiant Stars and Supergiant High Mass X-Ray Binaries, *Space Sci. Rev.*, 2017, vol. 212, p. 59
- Masters A., Achilleos N., Kivelson M. G., Sergis N., Dougherty M. K., Thomsen M. F., Arridge C. S., Krimigis S. M., McAndrews H. J., Kanani S. J., Krupp N., Coates A. J., Cassini observations of a Kelvin-Helmholtz vortex in Saturn's outer magnetosphere, *Journal of Geophysical Research (Space Physics)*, 2010, vol. 115, p. A07225
- Mather J. C., The James Webb Space Telescope Mission. In *American Institute of Physics Conference Series* , vol. 1294 of *American Institute of Physics Conference Series*, 2010, p. 1
- Mays M. L., Taktakishvili A., Pulkkinen A., MacNeice P. J., Rastätter L., Odstrcil D., Jian L. K., Richardson I. G., LaSota J. A., Zheng Y., Kuznetsova M. M., Ensemble Modeling of CMEs Using the WSA-ENLIL+Cone Model, *Sol. Phys.*, 2015, vol. 290, p. 1775
- McComas D. J., Elliott H. A., Schwadron N. A., Gosling J. T., Skoug R. M., Goldstein B. E., The three-dimensional solar wind around solar maximum, *Geophys. Res. Lett.*, 2003, vol. 30, p. 1517
- Mewaldt R. A., Looper M. D., Cohen C. M. S., Haggerty D. K., Labrador A. W., Leske R. A., Mason G. M., Mazur J. E., von Roseninge T. T., Energy Spectra, Composition,

- and Other Properties of Ground-Level Events During Solar Cycle 23, *Space Sci. Rev.*, 2012, vol. 171, p. 97
- Micono M., Massaglia S., Bodo G., Rossi P., Ferrari A., Kelvin-Helmholtz instabilities in stellar jets. III. Evolution of spatial perturbations, *A&A*, 1998, vol. 333, p. 989
- Moreton G. E., $H\alpha$ Observations of Flare-Initiated Disturbances with Velocities ~ 1000 km/sec., *AJ*, 1960, vol. 65, p. 494
- Moreton G. E., Ramsey H. E., Recent Observations of Dynamical Phenomena Associated with Solar Flares, *PASP*, 1960, vol. 72, p. 357
- Möstl U. V., Temmer M., Veronig A. M., The Kelvin-Helmholtz Instability at Coronal Mass Ejection Boundaries in the Solar Corona: Observations and 2.5D MHD Simulations, *ApJ*, 2013, vol. 766, p. L12
- Mulay S., Subramanian S., Tripathi D., Isobe H., Glesener L., Initiation of Coronal Mass Ejection Event Observed on 2010 November 3: Multi-wavelength Perspective, *ApJ*, 2014, vol. 794, p. 78
- Müller D., Marsden R. G., St. Cyr O. C., Gilbert H. R., Solar Orbiter . Exploring the Sun-Heliosphere Connection, *Sol. Phys.*, 2013, vol. 285, p. 25
- Na H., Moon Y.-J., Lee H., Development of a Full Ice-cream Cone Model for Halo Coronal Mass Ejections, *ApJ*, 2017, vol. 839, p. 82
- Nykyri K., Foullon C., First magnetic seismology of the CME reconnection outflow layer in the low corona with 2.5-D MHD simulations of the Kelvin-Helmholtz instability, *Geophys. Res. Lett.*, 2013, vol. 40, p. 4154
- Odert P., Leitzinger M., Hanslmeier A., Lammer H., Stellar coronal mass ejections - I. Estimating occurrence frequencies and mass-loss rates, *MNRAS*, 2017, vol. 472, p. 876
- Ofman L., Thompson B. J., SDO/AIA Observation of Kelvin-Helmholtz Instability in the Solar Corona, *ApJ*, 2011, vol. 734, p. L11
- Oh S. Y., Yi Y., Kim Y. H., Solar Cycle Variation of the Interplanetary Forward Shock Drivers Observed at 1 AU, *Sol. Phys.*, 2007, vol. 245, p. 391

-
- Ontiveros V., Vourlidas A., Quantitative Measurements of Coronal Mass Ejection-Driven Shocks from LASCO Observations, *ApJ*, 2009, vol. 693, p. 267
- Opher M., Bibi F. A., Toth G., Richardson J. D., Izmodenov V. V., Gombosi T. I., A strong, highly-tilted interstellar magnetic field near the Solar System, *Nature*, 2009, vol. 462, p. 1036
- Opher M., Stone E. C., Gombosi T. I., The Orientation of the Local Interstellar Magnetic Field, *Science*, 2007, vol. 316, p. 875
- Páez A., Jatenco-Pereira V., Falceta-Gonçalves D., Opher M., Kelvin–Helmholtz Instability at the CME–Sheath and Sheath–Solar-wind Interfaces, *ApJ*, 2017, vol. 851, p. 112
- Páez A., Jatenco-Pereira V., Falceta-Gonçalves D., Opher M., SEPs and self–turbulence region in corrugated CME-driven shocks, *Submitted ApJ 2018 May*, 2018, vol. 000, p. 000
- Parker E. N., Hydromagnetic Dynamo Models., *ApJ*, 1955, vol. 122, p. 293
- Parker E. N., Dynamics of the Interplanetary Gas and Magnetic Fields., *ApJ*, 1958, vol. 128, p. 664
- Parker E. N., Comments on the reconnection rate of magnetic fields, *Journal of Plasma Physics*, 1973, vol. 9, p. 49
- Parker E. N., Nanoflares and the solar X-ray corona, *ApJ*, 1988, vol. 330, p. 474
- Parker E. N., Solar and stellar magnetic fields and atmospheric structures - Theory, *Sol. Phys.*, 1989, vol. 121, p. 271
- Parker E. N., Heating solar coronal holes, *ApJ*, 1991, vol. 372, p. 719
- Parker E. N., A solar dynamo surface wave at the interface between convection and nonuniform rotation, *ApJ*, 1993, vol. 408, p. 707
- Patzold M., Bird M. K., Volland H., Levy G. S., Seidel B. L., Stelzried C. T., The mean coronal magnetic field determined from HELIOS Faraday rotation measurements, *Sol. Phys.*, 1987, vol. 109, p. 91

- Pesnell W. D., Thompson B. J., Chamberlin P. C., The Solar Dynamics Observatory (SDO), *Sol. Phys.*, 2012, vol. 275, p. 3
- Petukhova A. S., Petukhov I. S., Petukhov S. I., Ksenofontov L. T., Solar Energetic Particle Acceleration by a Shock Wave Accompanying a Coronal Mass Ejection in the Solar Atmosphere, *ApJ*, 2017, vol. 836, p. 36
- Priest E., *Magnetohydrodynamics of the Sun*, 2014
- Quémerais E., Lallement R., Koutroumpa D., Lamy P., Velocity Profiles in the Solar Corona from Multi-Instrument Observations, *ApJ*, 2007, vol. 667, p. 1229
- Raymond J. C., Thompson B. J., St. Cyr O. C., Gopalswamy N., Kahler S., Kaiser M., Lara A., Ciaravella A., Romoli M., O'Neal R., SOHO and radio observations of a CME shock wave, *Geophys. Res. Lett.*, 2000, vol. 27, p. 1439
- Reames D. V., Coronal abundances determined from energetic particles, *Advances in Space Research*, 1995, vol. 15
- Reames D. V., Particle acceleration at the Sun and in the heliosphere, *Space Sci. Rev.*, 1999, vol. 90, p. 413
- Reames D. V., Solar Energetic-Particle Release Times in Historic Ground-Level Events, *ApJ*, 2009, vol. 706, p. 844
- Reames D. V., The Two Sources of Solar Energetic Particles, *Space Sci. Rev.*, 2013, vol. 175, p. 53
- Reames D. V., Kahler S. W., Ng C. K., Spatial and Temporal Invariance in the Spectra of Energetic Particles in Gradual Solar Events, *ApJ*, 1997, vol. 491, p. 414
- Reames D. V., Ng C. K., Heavy-Element Abundances in Solar Energetic Particle Events, *ApJ*, 2004, vol. 610, p. 510
- Reiner M. J., Kaiser M. L., Gopalswamy N., Aurass H., Mann G., Vourlidas A., Maksimovic M., Statistical analysis of coronal shock dynamics implied by radio and white-light observations, *J. Geophys. Res.*, 2001, vol. 106, p. 25279

-
- Savani N. P., Owens M. J., Rouillard A. P., Forsyth R. J., Davies J. A., Observational Evidence of a Coronal Mass Ejection Distortion Directly Attributable to a Structured Solar Wind, *ApJ*, 2010, vol. 714, p. L128
- Schmelz J. T., Reames D. V., von Steiger R., Basu S., Composition of the Solar Corona, Solar Wind, and Solar Energetic Particles, *ApJ*, 2012, vol. 755, p. 33
- Schwadron N. A., Lee M. A., Gorby M., Lugaz N., Spence H. E., Desai M., Török T., Downs C., Linker J., Lionello R., Mikić Z., Riley P., Giacalone J., Jokipii J. R., Kota J., Kozarev K., Particle Acceleration at Low Coronal Compression Regions and Shocks, *ApJ*, 2015, vol. 810, p. 97
- Sheeley Jr. N. R., Wang Y.-M., Hawley S. H., Brueckner G. E., Dere K. P., Howard R. A., Koomen M. J., Korendyke C. M., et al. Measurements of Flow Speeds in the Corona between 2 and 30 R sub sun, *ApJ*, 1997, vol. 484, p. 472
- Shen C., Wang Y., Gui B., Ye P., Wang S., Kinematic Evolution of a Slow CME in Corona Viewed by STEREO-B on 8 October 2007, *Sol. Phys.*, 2011, vol. 269, p. 389
- Singh A. P., Talwar S. P., Hydromagnetic stability of a plasma jet, *Sol. Phys.*, 1994, vol. 149, p. 331
- Slavin J. A., Anderson B. J., Baker D. N., Benna M., Boardsen S. A., Gloeckler G., Gold R. E., Ho G. C., Korth H., Krimigis S. M., McNutt R. L., Nittler L. R., Raines J. M., Sarantos M., Schriver D., et al. MESSENGER Observations of Extreme Loading and Unloading of Mercurys Magnetic Tail, *Science*, 2010, vol. 329, p. 665
- Stakhiv M., Landi E., Lepri S. T., Oran R., Zurbuchen T. H., On the Origin of Mid-latitude Fast Wind: Challenging the Two-state Solar Wind Paradigm, *ApJ*, 2015, vol. 801, p. 100
- Sterling A. C., Hudson H. S., Yohkoh SXT Observations of X-Ray “Dimming” Associated with a Halo Coronal Mass Ejection, *ApJ*, 1997, vol. 491, p. L55
- Sundberg T., Boardsen S. A., Slavin J. A., Blomberg L. G., Korth H., The Kelvin-Helmholtz instability at Mercury: An assessment, *Planet. Space Sci.*, 2010, vol. 58, p. 1434

- Susino R., Bemporad A., Mancuso S., Physical Conditions of Coronal Plasma at the Transit of a Shock Driven by a Coronal Mass Ejection, *ApJ*, 2015, vol. 812, p. 119
- Tappin S. J., The Deceleration of an Interplanetary Transient from the Sun to 5 Au, *Sol. Phys.*, 2006, vol. 233, p. 233
- Tian H., McIntosh S. W., Xia L., He J., Wang X., What can We Learn about Solar Coronal Mass Ejections, Coronal Dimmings, and Extreme-ultraviolet Jets through Spectroscopic Observations?, *ApJ*, 2012, vol. 748, p. 106
- Tousey R., The solar corona.. In *Space Research Conference* , 1973, p. 713
- Tsuneta S., Acton L., Bruner M., Lemen J., Brown W., Carvalho R., Catura R., Freeland S., Jurcevich B., Morrison M., Ogawara Y., Hirayama T., Owens J., The Soft X-ray Telescope for the SOLAR-A Mission, *Sol. Phys.*, 1991, vol. 136, p. 37
- Uchida Y., On the Exciters of Type II and Type III Solar Radio Bursts, *PASJ*, 1960, vol. 12, p. 376
- Žic T., Vršnak B., Temmer M., Jacobs C., Cylindrical and Spherical Pistons as Drivers of MHD Shocks, *Sol. Phys.*, 2008, vol. 253, p. 237
- Vernin J., Muñoz-Tuñón C., Sarazin M., Vazquez Ramió H., Varela A. M., Trinquet H., Delgado J. M., Jiménez Fuensalida J., et al. European Extremely Large Telescope Site Characterization I: Overview, *PASP*, 2011, vol. 123, p. 1334
- Villarreal D'Angelo C., Jardine M., See V., Prominence formation and ejection in cool stars, *MNRAS*, 2018, vol. 475, p. L25
- Vršnak B., Cliver E. W., Origin of Coronal Shock Waves. Invited Review, *Sol. Phys.*, 2008, vol. 253, p. 215
- Vršnak B., Maričić D., Stanger A. L., Veronig A. M., Temmer M., Roša D., Acceleration Phase of Coronal Mass Ejections: I. Temporal and Spatial Scales, *Sol. Phys.*, 2007, vol. 241, p. 85
- Vršnak B., Žic T., Falkenberg T. V., Möstl C., Vennerstrom S., Vrbanec D., The role of aerodynamic drag in propagation of interplanetary coronal mass ejections, *A&A*, 2010, vol. 512, p. A43

-
- Wang Y.-M., Sheeley Jr. N. R., Socker D. G., Howard R. A., Brueckner G. E., Michels D. J., Moses D., St. Cyr O. C., Llebaria A., Delaboudinière J.-P., Observations of Correlated White-Light and Extreme-Ultraviolet Jets from Polar Coronal Holes, *ApJ*, 1998, vol. 508, p. 899
- Warmuth A., Mann G., A model of the Alfvén speed in the solar corona, *A&A*, 2005, vol. 435, p. 1123
- Webb D. F., Howard R. A., The solar cycle variation of coronal mass ejections and the solar wind mass flux, *J. Geophys. Res.*, 1994, vol. 99, p. 4201
- Wild J. P., McCready L. L., Observations of the Spectrum of High-Intensity Solar Radiation at Metre Wavelengths. I. The Apparatus and Spectral Types of Solar Burst Observed, *AuSRA*, 1950, vol. 3, p. 387
- Wood B. E., Howard R. A., An Empirical Reconstruction of the 2008 April 26 Coronal Mass Ejection, *ApJ*, 2009, vol. 702, p. 901
- Wood B. E., Howard R. A., Socker D. G., Reconstructing the Morphology of an Evolving Coronal Mass Ejection, *ApJ*, 2010, vol. 715, p. 1524
- Wood B. E., Wu C.-C., Howard R. A., Socker D. G., Rouillard A. P., Empirical Reconstruction and Numerical Modeling of the First Geoeffective Coronal Mass Ejection of Solar Cycle 24, *ApJ*, 2011, vol. 729, p. 70
- Wood B. E., Wu C.-C., Rouillard A. P., Howard R. A., Socker D. G., A Coronal Hole's Effects on Coronal Mass Ejection Shock Morphology in the Inner Heliosphere, *ApJ*, 2012, vol. 755, p. 43
- Xie H., Ofman L., Lawrence G., Cone model for halo CMEs: Application to space weather forecasting, *Journal of Geophysical Research (Space Physics)*, 2004, vol. 109, p. A03109
- Xie H., St. Cyr O. C., Gopalswamy N., Yashiro S., Krall J., Kramar M., Davila J., On the Origin, 3D Structure and Dynamic Evolution of CMEs Near Solar Minimum, *Sol. Phys.*, 2009, vol. 259, p. 143

- Yashiro S., Gopalswamy N., Michalek G., St. Cyr O. C., Plunkett S. P., Rich N. B., Howard R. A., A catalog of white light coronal mass ejections observed by the SOHO spacecraft, *Journal of Geophysical Research (Space Physics)*, 2004, vol. 109, p. 7105
- Yurchyshyn V., Abramenko V., Tripathi D., Rotation of White-light Coronal Mass Ejection Structures as Inferred from LASCO Coronagraph, *ApJ*, 2009, vol. 705, p. 426
- Yurchyshyn V., Yashiro S., Abramenko V., Wang H., Gopalswamy N., Statistical Distributions of Speeds of Coronal Mass Ejections, *ApJ*, 2005, vol. 619, p. 599
- Zank G. P., Rice W. K. M., Wu C. C., Particle acceleration and coronal mass ejection driven shocks: A theoretical model, *J. Geophys. Res.*, 2000, vol. 105, p. 25079
- Zaqarashvili T. V., Díaz A. J., Oliver R., Ballester J. L., Instability of twisted magnetic tubes with axial mass flows, *A&A*, 2010, vol. 516, p. A84
- Zaqarashvili T. V., Vörös Z., Narita Y., Bruno R., Twisted Magnetic Flux Tubes in the Solar Wind, *ApJ*, 2014, vol. 783, p. L19
- Zaqarashvili T. V., Vörös Z., Zhelyazkov I., Kelvin-Helmholtz instability of twisted magnetic flux tubes in the solar wind, *A&A*, 2014, vol. 561, p. A62
- Zaqarashvili T. V., Zhelyazkov I., Ofman L., Stability of Rotating Magnetized Jets in the Solar Atmosphere. I. Kelvin-Helmholtz Instability, *ApJ*, 2015, vol. 813, p. 123
- Zhang J., Dere K. P., A Statistical Study of Main and Residual Accelerations of Coronal Mass Ejections, *ApJ*, 2006, vol. 649, p. 1100
- Zhang J., Dere K. P., Howard R. A., Kundu M. R., White S. M., On the Temporal Relationship between Coronal Mass Ejections and Flares, *ApJ*, 2001, vol. 559, p. 452
- Zhang J., Dere K. P., Howard R. A., Vourlidas A., A Study of the Kinematic Evolution of Coronal Mass Ejections, *ApJ*, 2004, vol. 604, p. 420
- Zhelyazkov I., Zaqarashvili T. V., Chandra R., Kelvin-Helmholtz instability in coronal mass ejecta in the lower corona, *A&A*, 2015, vol. 574, p. A55
- Zucca P., Carley E. P., Bloomfield D. S., Gallagher P. T., The formation heights of coronal shocks from 2D density and Alfvén speed maps, *A&A*, 2014, vol. 564, p. A47

Appendix

Appendix A



Kelvin–Helmholtz Instability at the CME–Sheath and Sheath–Solar-wind Interfaces

A. Páez¹ , V. Jatenco-Pereira¹, D. Falceta-Gonçalves², and M. Opher³ 

¹ Instituto de Astronomia, Geofísica e Ciências Atmosféricas, Universidade de São Paulo, Rua do Matão 1226, São Paulo, SP, 05508-090, Brazil; andresspaez@usp.br

² Escola de Artes, Ciências e Humanidades, Universidade de São Paulo, Rua Arlindo Bettio 1000, São Paulo, SP, 03828-000, Brazil

³ Astronomy Department, Boston University, Boston, MA 02215, USA

Received 2017 April 7; revised 2017 October 27; accepted 2017 October 29; published 2017 December 18

Abstract

Wave-like features recently observed in some coronal mass ejections (CMEs) have been associated with the presence of Kelvin–Helmholtz instability (KHI) in the low corona. Previous works found observational evidence of KHI in a CME; this was followed by numerical simulations in order to determine the magnetic field strength allowing for its existence. Here, we present the first discussion of KHI formation in the outer corona at heliocentric distances from $4 R_{\odot}$ to $30 R_{\odot}$. We study separately the CME–sheath and sheath–solar-wind (Sh–SW) interfaces of two CMEs that propagated in the slow and fast SWs. Mapping the velocities, densities, and magnetic field strengths of the CMEs, sheaths, and SWs in the CME’s flanks, we solve the Chandrasekhar condition for KHI formation. Calculations show that KHI formation is more likely in a CME propagating in a slow SW (CME 1) than that propagating in a fast SW due to the large shear flow between the CME and the slow SW. Comparing the interfaces for both CME cases, we note that the Sh–SW interface of CME 1 is more conducive to the instability because of the similar strengths of the magnetic field necessary for KHI formation and of the SW magnetic field.

Key words: instabilities – plasmas – solar wind – Sun: coronal mass ejections (CMEs) – Sun: magnetic fields

1. Introduction

Coronal mass ejections (CMEs) are the strongest solar ejections of plasma and magnetic field propagating into the solar wind (hereafter SW), releasing the stored energy into SW (Emslie et al. 2004). CME propagation can be divided into three dynamical phases: initiation, acceleration, and propagation (Zhang & Dere 2006). The first two phases occur in the low corona ($<2 R_{\odot}$) and the third one at distances $>2 R_{\odot}$. The CMEs that expand and propagate with a velocity ($>800 \text{ km s}^{-1}$) greater than the magnetosonic medium velocity can drive shock waves ahead of the ejecta and the sheath structure behind the shock through SW plasma compression (e.g., Bacchini et al. 2015 and references therein). Raymond et al. (2000) and Mancuso et al. (2002) show the shock formation in the low corona in heliocentric distances less than $2 R_{\odot}$. The most notable evidence of shock formation are the onset of type II radio bursts and the acceleration of solar energetic particles (e.g., Gosling 1993; Reames 1999).

At the interfaces between the CME, sheath, and SW, shear flows that allow conditions appropriate for the formation of the Kelvin–Helmholtz instability (hereafter KHI; e.g., Manchester et al. 2005) may exist. This instability is a hydrodynamical phenomenon that occurs in fluids and plasmas as rotating regions known as vortices. KHI is affected by the geometry and strength of the magnetic field parallel to the interface of the shear flow, because the magnetic field tension opposes the growth of the vortices (Chandrasekhar 1961). KHI can be found in many astrophysical environments, such as planetary environments (Hasegawa et al. 2004; Amerstorfer et al. 2007; Sundberg et al. 2010), stellar jets (Micono et al. 1998), solar atmosphere and coronal streamer (Cavus & Kazkapan 2013; Feng et al. 2013), among others.

The first observational KHI features in CMEs were associated with the CME of 2010 November 3 by Foullon et al. (2011). The authors perform temporal and spatial analyses of the KHI evolution at the northern CME flank at distances

less than 150 Mm (10^3 km) from the solar surface. Foullon et al. (2013) performed a spectral analysis on the same CME to explore the CME plasma structure to corroborate the features observed by Foullon et al. (2011). An additional study by Nykyri & Foullon (2013) demonstrates the development of KHI through compressible 2.5D magnetohydrodynamic (MHD) simulations using the conditions of the ejecta of 2010 November 3. Supplementary observations of the KHI formation are presented by Ofman & Thompson (2011) and Möstl et al. (2013) for the events of 2010 April 8 and 2011 February 24, respectively. Their observations are supported by 2.5D MHD simulations, where different physical properties of the KHI in both events were estimated. Some analytical studies of KHI formation in environments with flux tubes are shown by Zaqarashvili et al. (2010, 2014a, 2014b, 2015) and Zhelyazkov et al. (2015). These works analyze the balance of pressure in the twisted flux tube and conclude that KHI exists for some unstable harmonics.

Motivated by previous observations of KHI features in some CMEs in low-corona distances, we present a study in which we discuss KHI formation in the outer corona. This paper is focused on the CME–sheath (CME–Sh) and sheath–SW (Sh–SW) boundary layers of two CME-driven SWs that propagate in the slow and fast SWs. We are interested in these different environments to understand the conditions suitable for KHI formation. The central problem is to model the velocities, densities, and magnetic field strengths of the CMEs, sheaths, and SWs in order to solve the condition for KHI formation proposed by Chandrasekhar (1961).

This paper is organized as follows: in Section 2, we present the model for the slow and fast SWs and the CMEs with their sheaths and shocks. In Section 3, we show the calculus at the boundary layers of the CME and its sheath, and the sheaths and SW for the two CMEs studied, and we describe some conditions suitable for KHI formation. Finally, in Section 4, we present the discussion and the conclusions of our work.

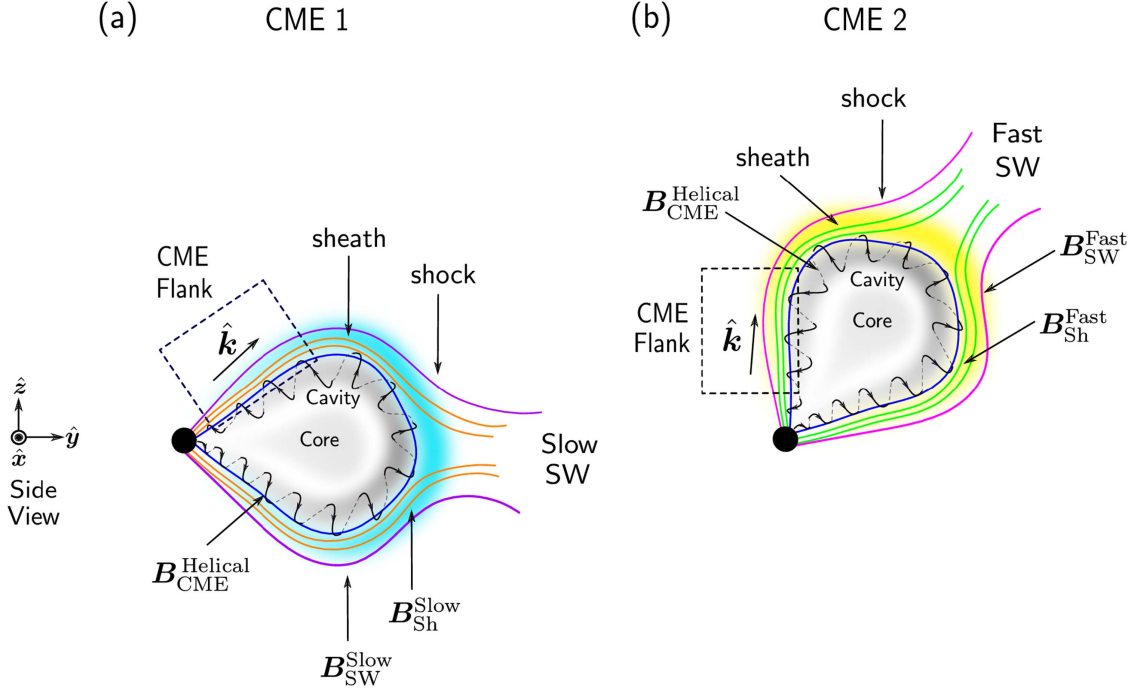


Figure 1. Illustrative 2D scheme of CME 1 (left side) and CME 2 (right side) propagating in the slow and fast solar winds (SWs), respectively. Panels (a) and (b) show our proposed zones for KHI formation on the CME flanks. We also show the CMEs' internal structure (core and cavity) and the presence of external structures, the sheaths and shocks, for both CMEs. The sheaths of CME 1 and CME 2 are represented by the cyan and yellow shaded regions, respectively. We show the helical magnetic structures of both CMEs (curved black arrow, $B_{\text{CME}}^{\text{Helical}}$) evolved by the sheaths' magnetic field lines, shown by the $B_{\text{Sh}}^{\text{Slow}}$ (orange lines) and $B_{\text{Sh}}^{\text{Fast}}$ (green lines) lines, and the magnetic field lines of the SW, $B_{\text{SW}}^{\text{Slow}}$ (purple lines) and fast SW $B_{\text{SW}}^{\text{Fast}}$ (pink lines). We indicate the KHI region, together with the shear flow, \hat{k} , on the CME flanks, by the dashed black rectangle. The solid black point represents the Sun. In our calculation, we assume the solar rotation to be in \hat{z} direction.

2. Methodology

KHI has been observed in low-corona distances during the early stages of formation of some CMEs (e.g., Foullon et al. 2011; Ofman & Thompson 2011; Möstl et al. 2013). In the present work, we are motivated to discuss the possibility of KHI formation in the outer corona between heliocentric distances $4 R_{\odot}$ to $30 R_{\odot}$, unlike previous works. Our study simplifies the large variety of regimes and the multiplicity of configurations of the environment that may affect KHI formation, and we only consider the harmonics with the wave vector parallel to the flow that can be stabilized by a flow-aligned magnetic field. We adopt the KHI magnetic condition proposed in Chandrasekhar (1961), which is along the shear flow, \hat{k} , for an incompressible plasma without viscosity and in a thin layer with an external magnetic field,

$$[\hat{k} \cdot (\mathbf{V}_1 - \mathbf{V}_2)]^2 > \frac{\rho_1 + \rho_2}{\mu_0 \rho_1 \rho_2} [(\hat{k} \cdot \mathbf{B}_1)^2 + (\hat{k} \cdot \mathbf{B}_2)^2], \quad (1)$$

where the \mathbf{V} are the velocities, ρ the densities, \mathbf{B} the magnetic field of the two plasmas, and μ_0 the permeability of free space ($\mu_{\text{solar}} \approx 1$). For this, we assume in condition (1) an electron-proton plasma, i.e., $\rho = \rho_e + \rho_p$, with the approximations $\rho_e \approx n_e m_e$ and $\rho_p \approx n_p m_p$, and quasi-neutrality MHD, $n_e \approx n_p \approx n$. Thus, Equation (1) can be written as

$$[\hat{k} \cdot (\mathbf{V}_1 - \mathbf{V}_2)]^2 > \frac{n_1 + n_2}{m_p n_1 n_2} [(\hat{k} \cdot \mathbf{B}_1)^2 + (\hat{k} \cdot \mathbf{B}_2)^2]. \quad (2)$$

In order to study condition (2) at the CME–Sh and Sh–SW interfaces, we model the velocities, densities, and magnetic

field strengths for two CMEs propagating independently in the slow and fast SWs during the solar cycle minimum. We ignore the CME deflection checked in Kay et al. (2013), the CME rotations considered in Lynch et al. (2009), the twisted magnetic flux tubes (Zaqarashvili et al. 2010), and the effects of reconnection. The simulations in Evans et al. (2011) show how the orientations of the CME magnetic field with respect to the global magnetic field can generate changes on the CME–Pause morphology (hereafter the CME–Sh interface) in response to different balances of pressure.

We start analyzing the slow and fast SWs in Section 2.1 and the CMEs and their sheath structures in Sections 2.2 and 2.3, respectively. In Figure 1, on the left, we present the general scheme of our study of the CME 1 environment, and on the right, of the CME 2 environment. Figure 1 shows the general scheme of the KHI regions on the CME flanks for CME 1 and CME 2, which propagate in the slow and fast SWs, respectively. Panels (a) and (b) show the helical magnetic structures, $B_{\text{CME}}^{\text{Helical}}$, of CME 1 and CME 2 evolved by the sheath's magnetic field lines, $B_{\text{Sh}}^{\text{Slow}}$ (orange lines) and $B_{\text{Sh}}^{\text{Fast}}$ (green lines), and the magnetic field lines of the SW, $B_{\text{SW}}^{\text{Slow}}$ (purple lines) and fast SW $B_{\text{SW}}^{\text{Fast}}$ (pink lines). The sheaths of CME 1 and CME 2 are represented by the cyan and yellow shaded regions, respectively. We indicate the KHI region together with the shear flow, \hat{k} , on CME flanks by the dashed black rectangle. The solid black point represents the Sun, and solar rotation is assumed to be in the \hat{z} direction. We assume an axial symmetry on the CME. We consider the vectors \mathbf{V}_{SW} , \mathbf{B}_{SW} , \mathbf{V}_{Sh} , and \mathbf{B}_{Sh} to be aligned with \hat{k} ; in this text, we write the magnitudes as V_{SW} , B_{SW} , V_{Sh} , and B_{Sh} .

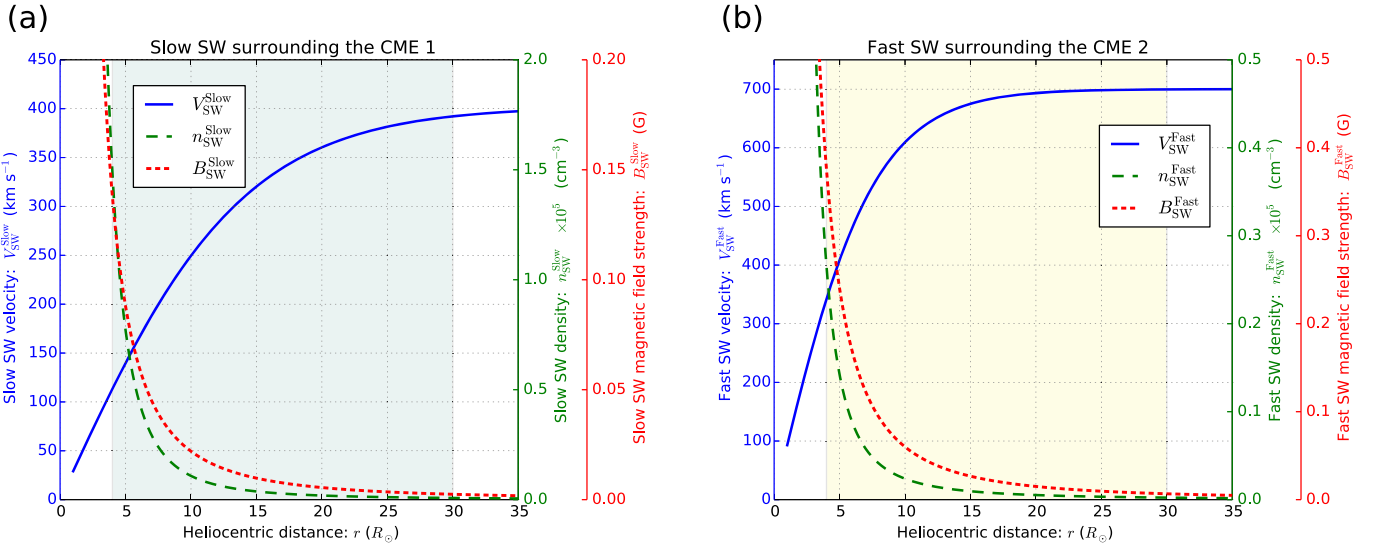


Figure 2. Panels show the SW velocities, Equation (3) (km s^{-1} , solid blue line); SW densities, Equation (4) (cm^{-3} , dashed green line); and SW magnetic field strengths, Equation (5) (Gauss, dotted red line) of the (a) slow and (b) fast SWs. The cyan and yellow shadows in the background are placed intentionally to emphasize the sheath color of Figure 1. The axis shows associated the color plot feature.

2.1. Solar Wind Model

In this paper, we use the bimodal pattern model for the SW, with the slow SW in the equator region and the fast SW close to the solar poles. For both types of winds, we construct the speed, density, and magnetic field expressions dependent on the heliocentric distance, r . The velocity for the SWs (V_{SW}) is modeled using the hyperbolic tangent profile (e.g., Coles et al. 1991; Chen 1996; Borgazzi et al. 2009),

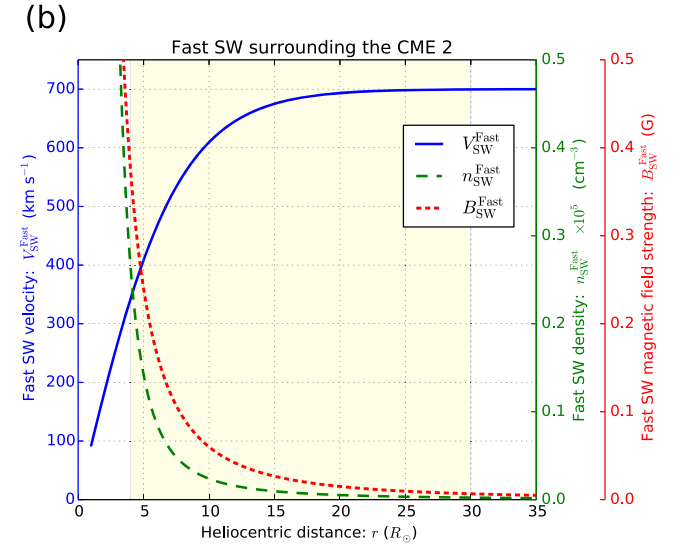
$$V_{\text{SW}}(r) = a \tanh\left(\frac{r}{b}\right). \quad (3)$$

The slow and fast SW velocity profiles are defined by adjusting the constants a and b using two pairs of values for the velocity and distance. From Abbo et al. (2010), we propose for the slow SW the velocity of 100 km s^{-1} at $3.5 R_{\odot}$. For the fast SW, we assume the velocity of 200 km s^{-1} at $2.2 R_{\odot}$. We adopt the velocity of 400 km s^{-1} for the slow SW (e.g., Chen 1996) and 700 km s^{-1} for the fast SW (e.g., Stakhiv et al. 2015), both at distances of $40 R_{\odot}$. We find the values $a = 402.7 \text{ km s}^{-1}$ and $b = 13.8$ for the slow SW, and $a = 700 \text{ km s}^{-1}$ and $b = 7.48$ for the fast SW. Figures 2(a) and (b) show the velocity profiles in km s^{-1} ($V_{\text{SW}}^{\text{Slow, Fast}}$, solid blue line), the density in cm^{-3} ($n_{\text{SW}}^{\text{Slow, Fast}}$, dashed green line), and the magnetic field strength in Gauss ($B_{\text{SW}}^{\text{Slow, Fast}}$, dotted red line) of the slow and fast winds. The density and magnetic field strength are modeled using Equations (4) and (5), respectively. Our slow SW velocity model is in agreement with that of Quémerais et al. (2007) and Sheeley et al. (1997).

The numerical densities (n_{SW}) of the slow and fast SWs were obtained using the conservation of mass flux law with the SW velocities, Equation (3),

$$n_{\text{SW}}(r) V_{\text{SW}}(r) r^2 = \text{constant}. \quad (4)$$

We take the electronic density values from Abbo et al. (2010) for the slow SW, $2.2 \times 10^5 \text{ cm}^{-3}$ at $3.5 R_{\odot}$, in the boundary of the streamer belt (hereafter SB). For the edge of a coronal hole (hereafter CH), we assume $1.5 \times 10^5 \text{ cm}^{-3}$ at $2.2 R_{\odot}$; see Figures 2(a) and (b).



The SW magnetic field profile is obtained from the flux conservation law assuming radial magnetic field lines,

$$B_{\text{SW}}(r) = \frac{B_{\text{SW}}(r_0)}{r^2}. \quad (5)$$

At the solar surface, we use $B_{\text{SW}}(r_0) = 2.2 \text{ G}$ for the slow SW (e.g., Mann et al. 2003) and 6.0 G for the fast SW (Manchester et al. 2004; see Figures 2(a) and (b)). In Figure 3, we compare the magnetic field profile obtained with Equation (5), $B_{\text{SW}}^{\text{Slow}}(r)$ (left side) and $B_{\text{SW}}^{\text{Fast}}(r)$ (right side), with (i) the magnetic field profile proposed by Dulk & McLean (1978), $B(r) = 0.5 (r - 1)^{-1.5} \text{ G}$, for $r \leq 10 R_{\odot}$; (ii) the profile proposed by Patzold et al. (1987), $B(r) = 6 r^{-3} + 1.18 r^{-2}$ between the heliocentric distances of $2 R_{\odot} \leq r \leq 15 R_{\odot}$; and finally, (iii) with the Gopalswamy & Yashiro (2011, hereafter G&Y2011) profile, $B(r) = 0.409 r^{-1.3}$, for the interval 6 to $23 R_{\odot}$. We can see from Figure 3 that our slow SW magnetic field profile is in agreement with previous magnetic field models. G&Y2011 is the profile most like our fast SW magnetic profile ($> 8 R_{\odot}$). The disagreement between the two is due to the fact that G&Y2011 constructed the profile using a SW velocity model with a terminal velocity of $\sim 400 \text{ km s}^{-1}$ (Sheeley et al. 1997).

In our calculation, we assume an error of $\pm 30\%$ on the velocity, density, and magnetic field strength of the SWs. In Section 3, we consider in the results the error propagation from the SW model (Section 2.1).

2.2. Coronal Mass Ejection Model

We analyze CMEs propagating in the slow and fast SW background. We are interested in constructing different environments in order to identify the constraints for KHI formation between $4 R_{\odot}$ and $30 R_{\odot}$. In this work, we assume the ejectas CME 1 and CME 2. These CMEs exhibit a morphology like the cone angle between opposing flanks, and are structured in three parts: the core, cavity, and frontal loop (Illing & Hundhausen 1985). The dynamics of the CMEs are restricted to the propagation phase with a constant velocity and

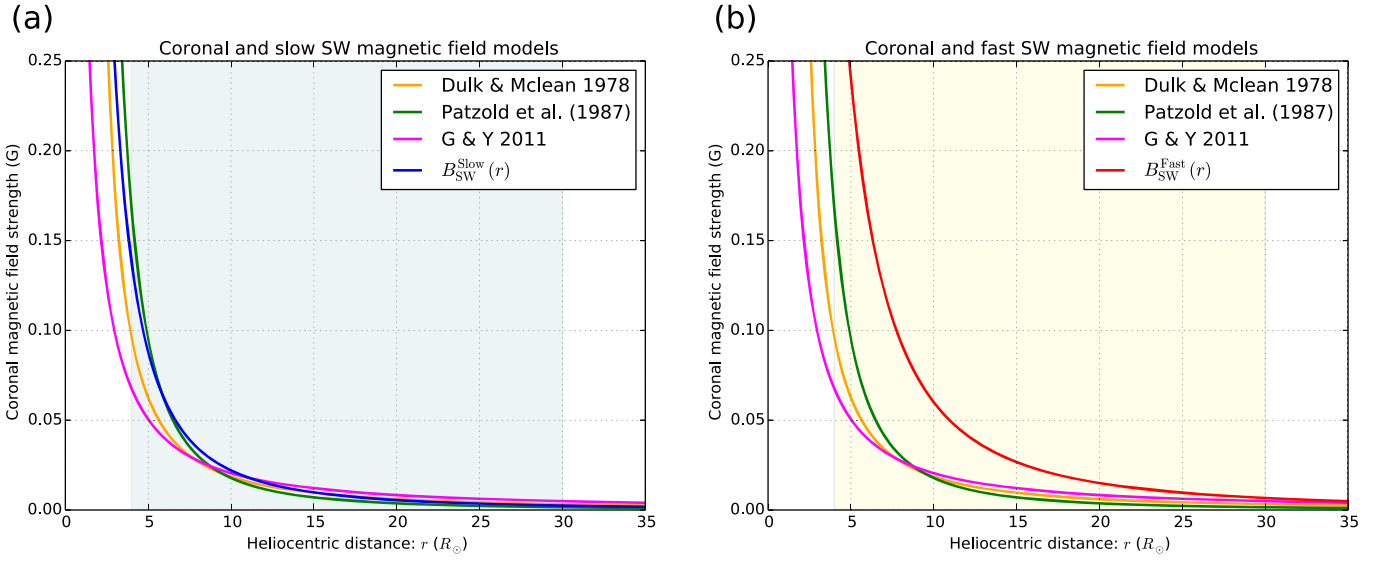


Figure 3. Panels comparing the (a) slow SW, $B_{\text{SW}}^{\text{Slow}}$, equation (blue continuous line) and (b) fast, $B_{\text{SW}}^{\text{Fast}}$, SW (Equation (5)) with the magnetic fields models. In orange, the Dulk & McLean (1978) profile. In green, the Patzold et al. (1987) profile. In pink, the Gopalswamy & Yashiro (2011) profile (G&Y2011).

residual deceleration imposed by the drag force from the SW background.

CME 1 is assumed to be propagating into the slow SW in the SB region with a velocity of 1000 km s^{-1} and residual acceleration of -4 m s^{-2} . In contrast, CME 2 is established in an anemone active region (hereafter AR; in the latitude $\phi \sim 40^\circ$) and evolved by a fast SW in a CH within an AR (e.g., Liu & Hayashi 2006; Liu 2007; Asai et al. 2009; Lugaz et al. 2011). For CME 2, a propagation velocity of 1200 km s^{-1} and a residual acceleration of -2 m s^{-2} are adopted. The fictitious CH force on CME 2 (e.g., Cremades et al. 2006; Gopalswamy et al. 2009) and the effects of the anemone AR on the evolution of CME 2 (e.g., Lugaz et al. 2011) are ignored. Figure 4 shows the velocities of CME 1 (solid blue line), CME 2 (solid red line), sheath 1 (dashed blue line), and sheath 2 (dashed red line) in the outer corona. The sheath velocities are modeled in Section 2.3. The limits of our interval are indicated by the vertical black lines at $4 R_\odot$ and $30 R_\odot$. The colored shadows are related to the sheath structure colors in Figure 1.

In order to solve condition (2) for KHI formation at the CME–Sh interface (in Equation (2), indexes 1 and 2, respectively), we consider the CMEs’ densities to be lower than the sheath structures’ densities, i.e., $n_{\text{CME}} < n_{\text{Sh}}$. With this approximation, we avoid the susceptibility of our calculations arriving at a unique CME density value. Our calculation is adapted to find the magnetic field strengths of the CMEs appropriate for KHI formation, with the purpose of solving the reverse problem: calculate the CME magnetic fields from KHI observations. In this way, we do not model the CMEs’ magnetic field strengths, but we consider the CMEs’ helical magnetic field structure (Dere et al. 1999). In Section 3.1, we modify our method in order to find the constraint for KHI formation. We propose the CME flanks to be KHI regions (see Figure 1). These regions were chosen because the magnetic field lines may be stretched by CME propagation, i.e., the magnetic tension here may be lower than in the curved magnetic field lines that evolve in the CME nose. Furthermore, these zones are chosen in the same way as in the observational samples of Foullon et al. (2011).

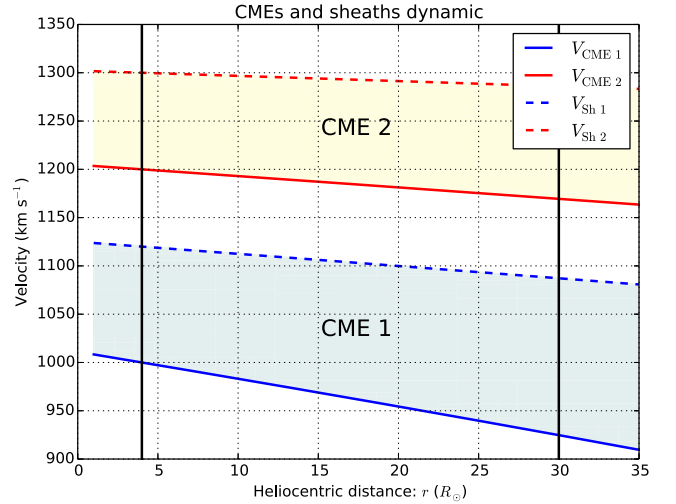


Figure 4. CME 1 velocity profile ($V_{\text{CME}1}$, solid blue line) and sheath 1 ($V_{\text{Sh}1}$, dashed blue line), together with the CME 2 velocity profile ($V_{\text{CME}2}$, solid red line) and sheath 2 ($V_{\text{Sh}2}$, dashed red line), in the outer corona between $4 R_\odot$ to $30 R_\odot$ (solid black vertical lines). The colors of the shadows are related to the sheath structure colors in Figure 1. The cyan and yellow regions between the solid and dashed blue and red lines represent the amplitude of the shear flow function, $S(r)$, Equation (15), for the cases of CME 1 and CME 2, respectively.

2.3. Shock and Sheath Structures

To model the CMEs, we assume the formation of a parallel coronal shock in the low corona, $< 2 R_\odot$, imposing that the ejecta velocities be faster than the magnetosonic background speed (e.g., Raymond et al. 2000; Mancuso et al. 2002). We take into account that the sheath structure becomes less dense and weaker with the increase of heliocentric distance; for this reason, we adopt the function for the sheath compression layer as the ratio between the downward and upward densities ($X = \rho_{\text{dw}}/\rho_{\text{up}}$) shown in Figure 1, panels (a) and (b). Bemporad & Mancuso (2011) and Bemporad et al. (2014) calculate the latitudinal plasma density compression ratio, X , in the event of 1999 June 11 observed in the C2 and C3 coronagraphs of LASCO. The authors reveal that the nose shock changes from

supercritical ($X < 3.0$) to subcritical ($X < 1.5$) from $\sim 2.5 R_{\odot}$ to $\sim 5.0 R_{\odot}$. In contrast, they affirm that the CME flanks are subcritical ($X < 1.5$) in this interval. In the present work, we propose a linear function for the compression ratio, X . We suggest that X decreases from 1.3 to 1.1 and 1.5 to 1.1 for CME 1 and CME 2, respectively. The compression functions, $X_{\text{CME}}(r)$, for CME 1 and CME 2 are given in Equations (6) and (7):

$$X_{\text{CME1}}(r) = -0.007 r + 1.328 \quad (6)$$

and

$$X_{\text{CME2}}(r) = -0.015 r + 1.56. \quad (7)$$

So, the sheath structure densities are, respectively,

$$n_{\text{Sh1}}(r) = X_{\text{CME1}}(r) n_{\text{SW}}^{\text{Slow}}(r) \quad (8)$$

and

$$n_{\text{Sh2}}(r) = X_{\text{CME2}}(r) n_{\text{SW}}^{\text{Fast}}(r), \quad (9)$$

where the slow and fast SW density, n_{SW} , correspond to Equation (4).

In contrast to the asymmetrical velocities in the CME nose and CME flanks calculated in Bemporad et al. (2014), we assume that the sheath structure propagates with only latitudinal shock velocity. We propose that the shock velocities are slightly larger than the CME velocities, but the shock accelerations are moderately lower than the CME accelerations. For CME 1 and CME 2, we assume the shock velocities of 1120 km s^{-1} and 1300 km s^{-1} and shock decelerations of -2 m s^{-2} and -1 m s^{-2} , respectively. Figure 4 shows the shock 1 (dashed blue line) and shock 2 (dashed red line) velocities in km s^{-1} between $4 R_{\odot}$ to $30 R_{\odot}$, indicated in the plot by vertical black lines.

3. KHI Formation in Boundary Layers

In this paper, we analyze KHI formation in two CMEs propagating in slow and fast SWs. We also analyze KHI formation on the CME flanks. Our hypothesis considers that in these regions, the magnetic field tension is less than that in the nose of the CME region. Here, we assume axial symmetry in both CMEs. Figure 5 shows the general situation in the KHI regions. In panel (a), the CME, sheath, and SW plasmas are shown by the gray shadows together with the CME–Sh (green shadow) and Sh–SW (orange shadow) interfaces. We show the helical magnetic field structure of the CME, $\mathbf{B}_{\text{CME}}^{\text{Helical}}$, with the black arrows between the \odot and \otimes symbols representing the outward and inward magnetic field polarities, respectively. The magnetic field lines of the sheaths (\mathbf{B}_{Sh}) and SW (\mathbf{B}_{SW}) are aligned with the interfaces and shear flow, $\hat{\mathbf{k}}$. In panel (b), we amplify the structure of the CME–Sh interface. We decompose $\mathbf{B}_{\text{CME}}^{\text{Helical}}$ into its poloidal ($\mathbf{B}_{\text{CME}}^{\text{Pol}}$, red arrow) and toroidal ($\mathbf{B}_{\text{CME}}^{\text{Tor}}$, brown arrow) components. Panel (c) shows the Sh–SW interface. The structure of this boundary is less complex than the CME–Sh interface due to the sheath structure being shaped by the compression of the SW magnetic field lines. In this section, we adapt the SW, CME, and sheath modeling of Section 2 for the condition of KHI formation, Equation (2), in order to find constraints for KHI formation at the CME–Sh and Sh–SW interfaces for the two CME cases.

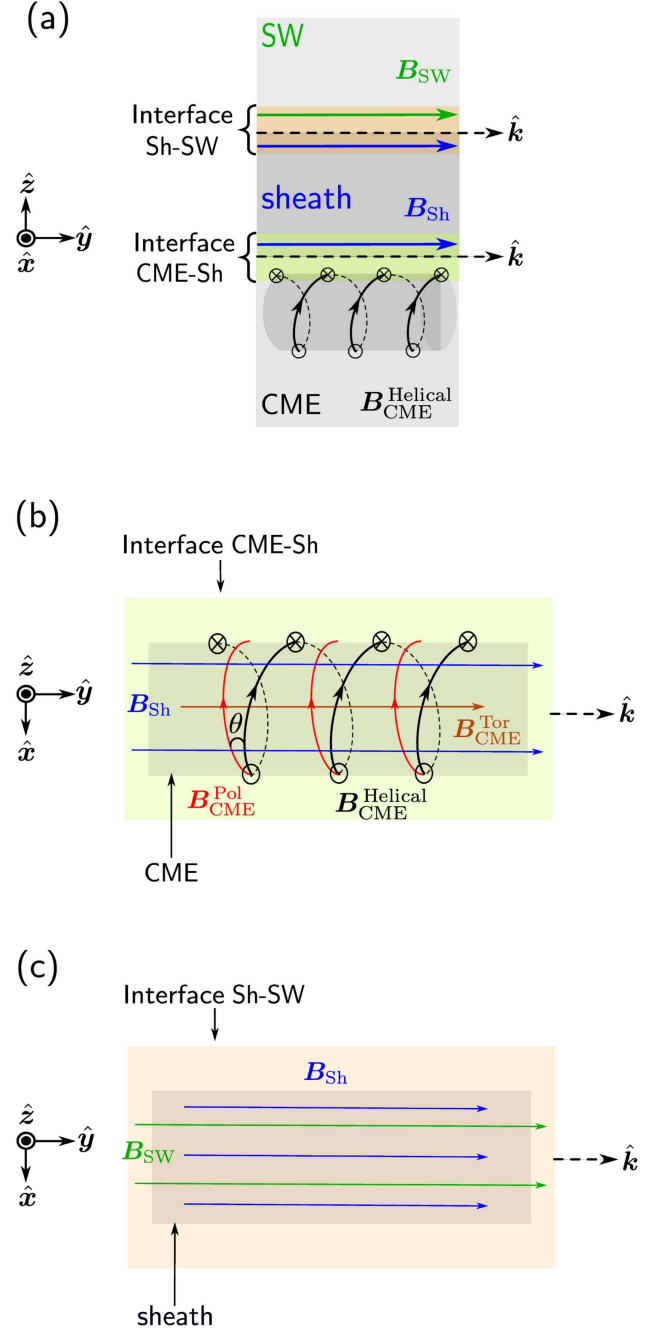


Figure 5. Schematic magnetic configuration of the KHI regions on the CME flanks. In panel (a), the CME, sheath, and SW plasmas are generalized by the gray shadows and the CME–Sh (green shadow) and Sh–SW (orange shadow) interfaces and the shear flow, $\hat{\mathbf{k}}$ (dashed black arrows) are indicated. We show the helical magnetic field structure of the CME, $\mathbf{B}_{\text{CME}}^{\text{Helical}}$, with the black arrows between the \odot and \otimes symbols, which represent the outward and inward magnetic field polarities, respectively. The magnetic field lines of the sheaths (\mathbf{B}_{Sh}) and SW (\mathbf{B}_{SW}) are shown by the blue and green arrows, respectively. In panel (b), we emphasize the structure of the CME–Sh interface. We decompose $\mathbf{B}_{\text{CME}}^{\text{Helical}}$ into its poloidal ($\mathbf{B}_{\text{CME}}^{\text{Pol}}$, red arrow) and toroidal ($\mathbf{B}_{\text{CME}}^{\text{Tor}}$, brown arrow) components. We simplify our calculation of these components by assuming the θ angle as the stretch caused by the propagation and expansion of the CME on the helical structure. We assume that $\mathbf{B}_{\text{CME}}^{\text{Tor}}$ affects KHI formation while $\mathbf{B}_{\text{CME}}^{\text{Pol}}$ does not (Chandrasekhar 1961). Panel (c) shows the Sh–SW interface. The structure of this boundary is less complex than that of the CME–Sh interface due to the sheath structure being shaped by the compression of the SW magnetic field lines.

3.1. Interface Between the CME and Its Sheath Structure

The density ratio in Equation (2) is simplified by assuming that the CME density (n_{CME}) is lower than the sheath density (n_{Sh}). In our calculation, we adopt $n_{\text{CME}} < n_{\text{Sh}} \lesssim 2 n_{\text{CME}}$, due to the plasma accumulating in the sheaths by the propagation and expansion of the CMEs. Thus, the ratio density can be written as

$$\frac{n_{\text{CME}} + n_{\text{Sh}}}{m_p n_{\text{CME}} n_{\text{Sh}}} \lesssim \frac{3}{m_p n_{\text{Sh}}}. \quad (10)$$

With this approximation, the calculation becomes independent of the CME density, n_{CME} .

We consider that $B_{\text{CME}} \gg B_{\text{Sh}}$ and so Equation (2) is independent of B_{Sh} ,

$$[\hat{\mathbf{k}} \cdot (\mathbf{V}_{\text{CME}} - \mathbf{V}_{\text{Sh}})]^2 > \frac{3}{m_p n_{\text{Sh}}} (\hat{\mathbf{k}} \cdot \mathbf{B}_{\text{CME}})^2. \quad (11)$$

In order to solve Equation (11), we analyze the term $\hat{\mathbf{k}} \cdot \mathbf{B}_{\text{CME}}$ through the poloidal, $\mathbf{B}_{\text{CME}}^{\text{Pol}}$, and toroidal, $\mathbf{B}_{\text{CME}}^{\text{Tor}}$ components of \mathbf{B}_{CME} ,

$$\hat{\mathbf{k}} \cdot \mathbf{B}_{\text{CME}}^{\text{Helical}} = \hat{\mathbf{k}} \cdot \mathbf{B}_{\text{CME}}^{\text{Pol}} + \hat{\mathbf{k}} \cdot \mathbf{B}_{\text{CME}}^{\text{Tor}}. \quad (12)$$

In Figure 5, panel (b), we show that $\mathbf{B}_{\text{CME}}^{\text{Pol}}$ is perpendicular to the shear flow, $\hat{\mathbf{k}}$, and so this component does not affect KHI formation (Chandrasekhar 1961). $\mathbf{B}_{\text{CME}}^{\text{Tor}}$ is parallel to $\hat{\mathbf{k}}$, which, as a consequence, can influence the instability formation. We simplify the calculation of the components $\mathbf{B}_{\text{CME}}^{\text{Pol}}$ and $\mathbf{B}_{\text{CME}}^{\text{Tor}}$ using the angle, θ , between the helical (black arrow) and poloidal (red arrow) components of the magnetic field (see Figure 5). We interpret this angle like a measurement of the “stretch” on the helical magnetic field structure due to the propagation and expansion of the CME. We suggest that a stronger stretch on the helical magnetic field may unbalance the magnetic components for larger values of θ . As first approximation, we use $\theta = 30^\circ$, proposing a possible equipartition between the poloidal and toroidal components,

$$\hat{\mathbf{k}} \cdot \mathbf{B}_{\text{CME}} = \hat{\mathbf{k}} \cdot \mathbf{B}_{\text{CME}}^{\text{Tor}} = \sin \theta B_{\text{CME}} = \frac{1}{2} B_{\text{CME}}. \quad (13)$$

Using Equation (13), Equation (11) can be written as

$$\hat{\mathbf{k}} \cdot (\mathbf{V}_{\text{CME}} - \mathbf{V}_{\text{Sh}})^2 > \frac{3 B_{\text{CME}}^2}{4 m_p n_{\text{Sh}}(r)}. \quad (14)$$

Assuming that the velocities \mathbf{V}_{CME} and \mathbf{V}_{Sh} are parallel to $\hat{\mathbf{k}}$, we define the left side of Equation (14) as a shear function $S(r)$,

$$S(r) = |V_{\text{CME}}(r) - V_{\text{Sh}}(r)|. \quad (15)$$

The $S(r)$ function represents the shear flow between the CME and its sheath structure. Figure 4 shows the amplitude of the shear flow function, $S(r)$, corresponding to the cyan and yellow regions between the solid and dashed blue and red lines for the CME 1 and CME 2 cases, respectively.

From Equation (14), we calculate the CME magnetic field appropriate for KHI, $B_{\text{CME}}^{\text{KH}}(r)$,

$$B_{\text{CME}}^{\text{KH}}(r) < \sqrt{\frac{4 m_p n_{\text{Sh}}(r)}{3}} S(r); \quad (16)$$

with Equation (16), it is possible to find the interval of magnetic field strengths that allows KHI formation between $4 R_\odot$ and $30 R_\odot$. In Section 2.1 of the SW model, we assume a $\pm 30\%$ error in the velocity, density, and magnetic field strength of the SWs. For $B_{\text{CME}}^{\text{KH}}(r)$, Equation (16), we assume an error of $\pm 34\%$ due to error propagation.

Figure 6 shows the results of KHI formation in the CME–Sh and Sh–SW interfaces. The CME 1 and CME 2 results are given in the left and right columns, respectively. The upper panels show the KHI constraint at the CME–Sh interface and the lower panels are linked to the KHI constraints at the Sh–SW interface modeled in the Section 3.2. The results for both CME cases are summarized in Table 1. Panels (a) and (b) show the appropriate magnetic field strength of the CME for KHI formation, Equation (16) ($B_{\text{CME}}^{\text{KH}}$, solid red line), and the logarithm of the shear flow function $S(r)$, Equation (15) ($\log S(r)$, dashed black line), respectively. The cyan and yellow shadows in the plots represent the colors assumed in Figure 1 for the sheath structures.

We find unequal results at the CME–Sh interface for the two CME cases. Our results illustrate a notable decrease of $B_{\text{CME}}^{\text{KH}}(r)$ due to the falling of the sheath density function as a consequence of the SW density (i.e., $n_{\text{Sh}}(r) \propto n_{\text{SW}}(r)$). The $S(r)$ and $\log S(r)$ functions increase due to the deceleration of the CME in the SW; see Figure 4. The differences in the $B_{\text{CME}}^{\text{KH}}(r)$ values for both CME cases, i.e., $B_{\text{CME1}}^{\text{KH}}(r) > B_{\text{CME2}}^{\text{KH}}(r)$, are a consequence of the SW densities because the shear values are similar (see Table 1). The set values for $B_{\text{CME1}}^{\text{KH}}(r)$ are two times larger than those for $B_{\text{CME2}}^{\text{KH}}(r)$; for this reason, we suppose that the conditions assumed for the CME 1 environment in this paper are more adequate for KHI formation than those assumed for the CME 2 environment. From the results, we conclude that the region close to $\gtrsim 4 R_\odot$ is more probable for KHI existence due to larger $B_{\text{CME}}^{\text{KH}}$ values compared to other distances, i.e., $\gtrsim 20 R_\odot$. As such, Figure 6 represents the quantitative KHI constraints that give evidence of the susceptibility of the CME–Sh boundary layer to KHI formation.

3.2. Interface Between the Sheath and Solar Wind

Using the same methodology as in Section 3.1, we model the Sh–SW interface. Through Equations (8) and (9), we can rewrite the term $n_{\text{SW}} + n_{\text{Sh}}$, which is equivalent to $(1 + X_{\text{CME}}) n_{\text{SW}}$. In this way, the density ratio in Equation (2) simplifies to

$$\frac{n_{\text{SW}} + n_{\text{Sh}}}{m_p n_{\text{SW}} n_{\text{Sh}}} \approx \frac{(1 + X_{\text{CME}})}{m_p n_{\text{Sh}}}. \quad (17)$$

Assuming the magnetic fields (\mathbf{B}_{Sh} , \mathbf{B}_{SW}) and velocities (\mathbf{V}_{Sh} , \mathbf{V}_{SW}) of the sheaths and SWs to be along the shear flow, $\hat{\mathbf{k}}$, we rewrite Equation (1) as

$$(V_{\text{Sh}} - V_{\text{SW}})^2 > \frac{(1 + X_{\text{CME}})}{m_p n_{\text{Sh}}} (B_{\text{Sh}}^2 + B_{\text{SW}}^2). \quad (18)$$

For Equation (18), we approximate the magnetic field strength of the sheaths as $B_{\text{SW}} < B_{\text{Sh}} < 2 B_{\text{SW}}$. So,

$$B_{\text{Sh}}^2 + B_{\text{SW}}^2 \lesssim 5 B_{\text{SW}}^2. \quad (19)$$

Inserting Equations (17) and (19) into Equation (18), we calculate the final condition for KHI formation at the Sh–SW

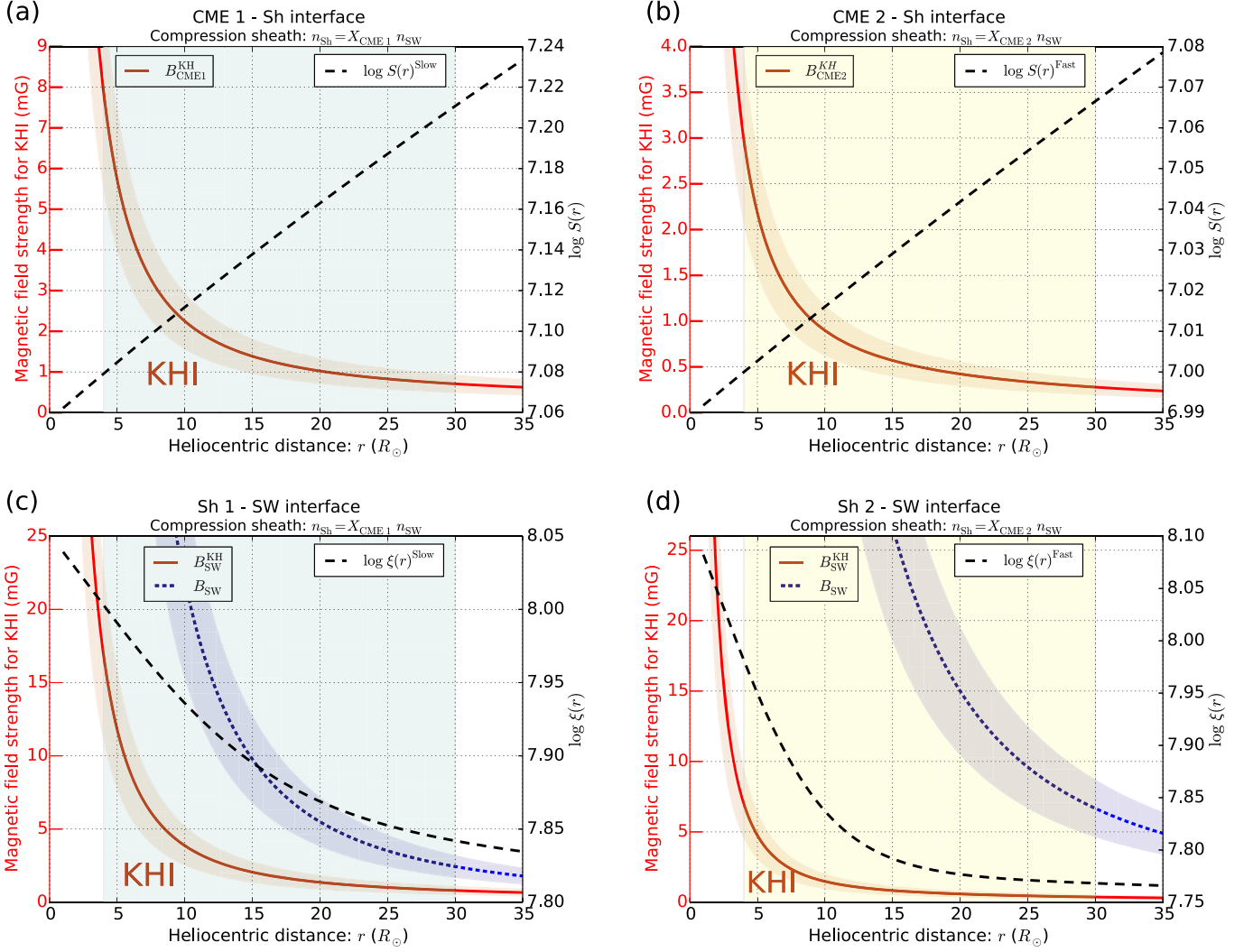


Figure 6. Plots for the KHI formation constraints. Panels (a) and (b) show the CME magnetic field, $B_{\text{CME}}^{\text{KH}}$ (Equation (16), solid red line) necessary for KHI formation and the logarithm of the shear flow, $S(r)$ (Equation (15), dashed black line) for the CME 1–Sh and CME 2–Sh interfaces, respectively. The values below the $B_{\text{CME}}^{\text{KH}}$ curve are those appropriate for KHI formation. Panels (c) and (d) show the SW magnetic field strength, B_{SW} (Equation (5), dotted blue line), SW magnetic field strength for KHI formation, $B_{\text{SW}}^{\text{KH}}$ (Equation (22), solid red line), and the shear flow, $\xi(r)$ (Equation (21), dashed black line). The values below the $B_{\text{SW}}^{\text{KH}}$ curve are linked with KHI formation. The blue shadow along B_{SW} represents the error of $\pm 30\%$ assumed in the SW model, while the red shadow along $B_{\text{CME}}^{\text{KH}}$ and $B_{\text{SW}}^{\text{KH}}$ represent the error propagation of $\pm 34\%$. The cyan and yellow shadows represent the colors assumed in Figure 1 for the sheath structures. We find CME and slow SW magnetic field values less than 7.9 ± 2.7 mG and 16.8 ± 5.7 mG, respectively, which may allow KHI in the slow SW environment, while the CME and fast SW magnetic field values less than 3.0 ± 1.0 and 7.0 ± 2.4 mG, respectively, allow the instability in the fast SW environment. These results are summarized in Table 1. Our calculations show that the KHI magnetic field strength of Sh–SW interfaces are larger than that of the CME–Sh interfaces for both CME cases. In this way, we note that the Sh–SW interface will be susceptible to KHI formation.

interface,

$$(V_{\text{Sh}} - V_{\text{SW}})^2 > \frac{5(1 + X_{\text{CME}})}{m_p n_{\text{Sh}}} B_{\text{SW}}^2. \quad (20)$$

From the left-hand side of Equation (20), we define the velocity shear function $\xi(r)$,

$$\xi(r) = |V_{\text{Sh}}(r) - V_{\text{SW}}(r)|. \quad (21)$$

The SW magnetic field strength appropriate for KHI formation is calculated from

$$B_{\text{SW}}^{\text{KH}}(r) < \sqrt{\frac{m_p n_{\text{Sh}}(r)}{5(1 + X_{\text{CME}})}} \xi(r). \quad (22)$$

In a similar way to $B_{\text{CME}}^{\text{KH}}(r)$, Equation (16), from the error assumed in the model of the SWs, i.e., $\pm 30\%$ (Section 2.1), we assume an error propagation of $\pm 34\%$ in $B_{\text{SW}}^{\text{KH}}(r)$, Equation (22).

Figures 6(c) and (d) show the SW magnetic field strength, $B_{\text{SW}}(r)$ (Equation (5), dotted blue line), the SW magnetic field strength appropriate for KHI formation, $B_{\text{SW}}^{\text{KH}}(r)$ (Equation (22), solid red line), and the logarithm of the shear flow, $\log \xi(r)$ (Equation (21), dashed black line). Magnetic field strength less than $B_{\text{SW}}^{\text{KH}}(r)$ allows KHI formation. In a similar way to Figures 6(a) and (b), $B_{\text{SW}}^{\text{KH}}(r)$ decreases due to the effect of the SW density, n_{SW} , at the heliocentric distance, r . The shear functions in the Sh–SW interface, $\xi(r)$ and $\log \xi(r)$, are larger than the shear functions in the CME–Sh interface, $S(r)$ and $\log S(r)$, that decrease as a consequence of the shock deceleration into SW; see Figure 4. The values of the $B_{\text{SW}}^{\text{KH}}$ of

Table 1
Results from Figure 6 for the CME 1 and CME 2 Cases for $4 R_{\odot}$
and $30 R_{\odot}$ at the CME–Sh and Sh–SW Interfaces

$r (R_{\odot})$	Interface CME–Sh		Interface Sh–SW	
	$S (\text{km s}^{-1})$	$B_{\text{CME}}^{\text{KH}} (\text{mG})$	$\xi (\text{km s}^{-1})$	$B_{\text{SW}}^{\text{KH}} (\text{mG})$
CME 1				
4.0	120.0	7.9 ± 2.7	1006.4	16.8 ± 5.7
30.0	162.4	0.7 ± 0.2	695.0	0.8 ± 0.3
CME 2				
4.0	100.0	3.0 ± 1.0	957.9	7.0 ± 2.4
30.0	116.5	0.3 ± 0.1	586.4	0.4 ± 0.1

Note. The shear function $S (\text{km s}^{-1})$, the CME magnetic field strengths for KHI existence $B_{\text{CME}}^{\text{KH}} (\text{mG})$, the shear function $\xi (\text{km s}^{-1})$, and the SW magnetic field strengths for KHI existence $B_{\text{SW}}^{\text{KH}} (\text{mG})$.

the slow SW are approximately two times larger than the $B_{\text{SW}}^{\text{KH}}$ of the fast SW. The results show that $B_{\text{SW}}^{\text{KH}}(r) < B_{\text{SW}}(r)$, but assuming error propagation ($\pm 34\%$, red shadow), we suppose that the region appropriate for KHI formation will be at larger distances, i.e., $\gtrsim 20 R_{\odot}$, in contrast to the CME–Sh interface. Panel (c) shows a larger $B_{\text{SW}}^{\text{KH}}$ than panel (d); as such, we consider the Sh–SW interface of CME 1 to be more conducive to KHI formation than the Sh–SW interface of CME 2.

Our calculation is focused on quantitative requirements in order to understand if the interfaces are predisposed to KHI formation. The results in Figure 6 indicate that the CME 1 interfaces are more conducive for KHI formation than the CME 2 interfaces, due to denser slow SWs and the amplitude of the shear flows. In order to optimize both CME environments for KHI formation, we can increase either the shear flow at the interfaces (i.e., analyze faster CMEs) or increase the density in the sheath structures (Zhelyazkov et al. 2015). These two options may be linked because the environments of faster CMEs can give rise to stronger shocks and consequently denser sheath structures. In a complementary way, from Magdalenic et al. (2010), we indicate that the flare energy released associated with a CME may give rise to denser sheath structures, increasing the possibility of KHI formation. We find that the best CME environment for KHI formation consists of a faster CME with an associated flare that propagates into the slow SW. These are exactly the features of the CME that occurred on 2010 November 3 and analyzed in Foullon et al. (2011), who found evidence of KHI formation.

4. Discussions and Conclusions

Previous works have shown KHI observations in low-corona distances (e.g., Foullon et al. 2011; Ofman & Thompson 2011; Möstl et al. 2013) in different CME events. In contrast, this paper shows the first discussion of KHI existence in the outer solar corona. Our work focused on analyzing the boundary layers CME–Sh and Sh–SW between $4 R_{\odot}$ to $30 R_{\odot}$ for two different CME cases. The interest in this interval is justified considering that the plasma magnetic field strengths decrease while the plasma velocities increase, and this combination may optimize the CME environments for KHI development.

In this paper, we define two CME-driven shock environments. In the first one, the CME propagates in the slow SW, and in the

second one, the CME propagates in the fast SW. The velocities, densities, and magnetic field strengths of the CMEs, the sheaths, and the SWs were modeled in order to solve the condition for KHI existence proposed by Chandrasekhar (1961). For both CME and shock propagation, a residual deceleration due to the drag force of the SW background is imposed. The geometrical disposition at the interfaces was simplified by assuming a parallel shock, and some variables that can affect the KHI existence e.g., compressibility and viscosity, were ignored. In this way, the most favorable environment for KHI development in order to understand the broadest set of KHI constraints is shown. In this work on the CME–Sh interface, we only consider the harmonics with the wave vector parallel to the flow. These harmonics are stabilized by a flow-aligned magnetic field. However, the harmonics that have wavenumbers perpendicular to the flow could still be unstable to KHI when there is a small transverse component of magnetic field (Singh & Talwar 1994; Zaqarashvili et al. 2010, 2014b, 2015).

The functions $B_{\text{CME}}^{\text{KH}}(r)$, Equation (16), and $B_{\text{SW}}^{\text{KH}}(r)$, Equation (22), represent the maximum magnetic field intervals that allow KHI formation at the CME–Sh and Sh–SW interfaces. Values here that are equal and lower are called the quantitative constraints for KHI formation. We find that CME 1 and slow SW magnetic field values lower than $7.9 \pm 2.7 \text{ mG}$ and $16.8 \pm 5.7 \text{ mG}$, respectively, may allow for the formation of the instability. CME 2 and fast SW magnetic field values lower than $3.0 \pm 1.0 \text{ mG}$ and $7.0 \pm 2.4 \text{ mG}$, respectively, are conducive to KHI existence (see Figure 6, Table 1). Our calculations show that the CME 1 environment is more conducive to KHI formation because $B_{\text{CME}}^{\text{KH}}$ and $B_{\text{SW}}^{\text{KH}}$ are larger than the respective magnetic fields strengths in the CME 2 environment. We explain this fact by the different values of the SW densities (i.e., $n_{\text{SW}}^{\text{Slow}}(r) > n_{\text{SW}}^{\text{Fast}}(r)$) and of the shear functions (i.e., $S_{\text{CME1}}(r) > S_{\text{CME2}}(r)$ and $\xi_{\text{CME1}}(r) > \xi_{\text{CME2}}(r)$), shown by the cyan and yellow regions in Figure 4. We consider a $\pm 30\%$ error on the SW model due to the variable behavior of the SWs; this drives an error propagation in our results of $\pm 34\%$. We consider that for both CME cases, the Sh–SW interface is more conducive to KHI formation due to the larger magnetic field strength that allows for instability formation, in addition to the magnetic structure being less complex than in the CME–Sh interfaces. Figure 6 shows that the slow Sh–SW interface close to $26 R_{\odot}$ has quantitative constraints on KHI formation, but the fast SW interface does not. From our results, we can affirm that the Sh–SW interface of the CME 1 case may be the best environment for KHI formation. So, our hypothesis shows that the best CME conditions for KHI formation are faster CMEs propagating in the solar equator region, features that are shown by the CME that occurred on 2010 November 3 and analyzed in Foullon et al. (2011). We accept some limitations of our model that are imposed by the complexity of the helical magnetic field structure of the CMEs. We consider the toroidal and poloidal components; through these, we find that the CME stretch may be a relevant parameter of the environment that may define KHI formation, in addition to previous constraints like the ratio density checked by Zhelyazkov et al. (2015).

We emphasize that a flare associated with the CME release energy contributes to the formation of a denser sheath structure (e.g., Magdalenic et al. 2010). Equations (16) and (22) show that increases in the sheath density, n_{Sh} , amplifies the threshold of the conditions for KHI existence, i.e., $B_{\text{CME}}^{\text{KH}} \propto n_{\text{Sh}}$. We conclude that a flare is a qualitative constraint of the CME

environment appropriate for KHI formation. On the other hand, from the results of Magdaleníć et al. (2010), it may be possible to have KHI formation in slow CMEs ($<500 \text{ km s}^{-1}$) due to the energy liberation of the associated flare. Finally, we indicate the results as examples of the predisposition of CME environments to the instability. We interpret our calculations as a prediction of the CME magnetic field measurements from KHI observations and vice versa.

We discuss two relevant points of the KHI phenomenon in CME events and use the KHI observations as a tool to estimate the CME magnetic field strength. The rare observations of KHI may indicate two limitations associated with KHI formation and evolution. The first may question whether the system—the CME, sheath, shock, and SW—is predisposed to the existence of KHI. The second is linked to the question of KHI evolution, and whether the rare observations of KHI in CME events may be consequences of the technological limitations of the instruments on board currently operating solar spacecraft. Our work shows the predisposition of the system to the existence of KHI in outer solar corona distances. Our results show that KHI may be more frequent in CME environments than in the events registered. On this point, the features of KHI evolution may be imperceptible, i.e., smaller vortex sizes or wavelengths, or growth rates; these features may not allow the instability to be monitored. In this way, we consider that a new generation of spacecraft i.e., the *Parker Solar Probe*, *Solar Orbiter*, and *Solar Sentinels* (all launching 2018) may overcome these limitations and detect more frequently the KHI evolution in outer corona distances. Finally, we think that our paper can be interpreted as the first discussion on KHI formation in a new solar corona environment, which is unlike the discussions in previous works. We show that KHI may exist; in this way, our work is the departure point for new studies on KHI formation and CME magnetic field strength.

D.F.G. thanks the Brazilian agencies CNPq (no. 302949/2014-3) and FAPESP (no. 2013/10559-5) for financial support. A.P. thanks the financial support from the Brazilian agency CAPES (Coordenação de Aperfeiçoamento de Pessoal de Nível Superior—PROEX 3474/2014).

ORCID iDs

A. Páez  <https://orcid.org/0000-0002-5954-8447>
M. Opher  <https://orcid.org/0000-0002-8767-8273>

References

- Abbo, L., Antonucci, E., Mikić, Z., et al. 2010, *AdSpR*, **46**, 1400
 Amerstorfer, U. V., Erkaev, N. V., Langmayr, D., & Biernat, H. K. 2007, *P&SS*, **55**, 1811
 Asai, A., Shibata, K., Ishii, T. T., et al. 2009, *JGRA*, **114**, A00A21
 Bacchini, F., Susino, R., Bemporad, A., & Lapenta, G. 2015, *ApJ*, **809**, 58
 Bemporad, A., & Mancuso, S. 2011, *ApJL*, **739**, L64
 Bemporad, A., Susino, R., & Lapenta, G. 2014, *ApJ*, **784**, 102
 Borgazzi, A., Lara, A., Echer, E., & Alves, M. V. 2009, *A&A*, **498**, 885
 Cavus, H., & Kazkapan, D. 2013, *NewA*, **25**, 89
 Chandrasekhar, S. 1961, *Hydrodynamic and Hydromagnetic Stability* (Oxford: Clarendon)
 Chen, J. 1996, *JGR*, **101**, 27499
 Coles, W. A., Esser, R., Løvhaug, U.-P., & Markkanen, J. 1991, *JGR*, **96**, 13849
 Cremades, H., Bothmer, V., & Tripathi, D. 2006, *AdSpR*, **38**, 461
 Dere, K. P., Brueckner, G. E., Howard, R. A., Michels, D. J., & Delaboudiniere, J. P. 1999, *ApJ*, **516**, 465
 Dulk, G. A., & McLean, D. J. 1978, *SoPh*, **57**, 279
 Emslie, A. G., Kucharek, H., Dennis, B. R., et al. 2004, *JGRA*, **109**, A10104
 Evans, R. M., Opher, M., & Gombosi, T. I. 2011, *ApJ*, **728**, 41
 Feng, L., Inhester, B., & Gan, W. Q. 2013, *ApJ*, **774**, 141
 Foullon, C., Verwichte, E., Nakariakov, V. M., Nykyri, K., & Farrugia, C. J. 2011, *ApJL*, **729**, L8
 Foullon, C., Verwichte, E., Nykyri, K., Aschwanden, M. J., & Hannah, I. G. 2013, *ApJ*, **767**, 170
 Gopalswamy, N., Mäkelä, P., Xie, H., Akiyama, S., & Yashiro, S. 2009, *JGRA*, **114**, A00A22
 Gopalswamy, N., & Yashiro, S. 2011, *ApJL*, **736**, L17
 Gosling, J. T. 1993, *JGR*, **98**, 18937
 Hasegawa, H., Fujimoto, M., Phan, T.-D., et al. 2004, *Natur*, **430**, 755
 Illing, R. M. E., & Hundhausen, A. J. 1985, *JGR*, **90**, 275
 Kay, C., Opher, M., & Evans, R. M. 2013, *ApJ*, **775**, 5
 Liu, Y. 2007, *ApJL*, **654**, L171
 Liu, Y., & Hayashi, K. 2006, *ApJ*, **640**, 1135
 Lugaz, N., Downs, C., Shibata, K., et al. 2011, *ApJ*, **738**, 127
 Lynch, B. J., Antiochos, S. K., Li, Y., Luhmann, J. G., & DeVore, C. R. 2009, *ApJ*, **697**, 1918
 Magdaleníć, J., Marqué, C., Zhukov, A. N., Vršnak, B., & Žic, T. 2010, *ApJ*, **718**, 266
 Manchester, W. B., Gombosi, T. I., Roussev, I., et al. 2004, *JGRA*, **109**, A01102
 Manchester, W. B., IV, Gombosi, T. I., De Zeeuw, D. L., et al. 2005, *ApJ*, **622**, 1225
 Mancuso, S., Raymond, J. C., Kohl, J., et al. 2002, *A&A*, **383**, 267
 Mann, G., Klassen, A., Aurass, H., & Klassen, H.-T. 2003, *A&A*, **400**, 329
 Miccono, M., Massaglia, S., Bodo, G., Rossi, P., & Ferrari, A. 1998, *A&A*, **333**, 989
 Möstl, U. V., Temmer, M., & Veronig, A. M. 2013, *ApJL*, **766**, L12
 Nykyri, K., & Foullon, C. 2013, *GeoRL*, **40**, 4154
 Ofman, L., & Thompson, B. J. 2011, *ApJL*, **734**, L11
 Patzold, M., Bird, M. K., Volland, H., et al. 1987, *SoPh*, **109**, 91
 Quémerais, E., Lallement, R., Koutroumpa, D., & Lamy, P. 2007, *ApJ*, **667**, 1229
 Raymond, J. C., Thompson, B. J., St., Cyr, O. C., et al. 2000, *GeoRL*, **27**, 1439
 Reames, D. V. 1999, *SSRv*, **90**, 413
 Sheeley, N. R., Jr., Wang, Y.-M., Hawley, S. H., et al. 1997, *ApJ*, **484**, 472
 Singh, A. P., & Talwar, S. P. 1994, *SoPh*, **149**, 331
 Stakhiv, M., Landi, E., Lepri, S. T., Oran, R., & Zurbuchen, T. H. 2015, *ApJ*, **801**, 100
 Sundberg, T., Boardsen, S. A., Slavin, J. A., Blomberg, L. G., & Korth, H. 2010, *P&SS*, **58**, 1434
 Zaqarashvili, T. V., Díaz, A. J., Oliver, R., & Ballester, J. L. 2010, *A&A*, **516**, A84
 Zaqarashvili, T. V., Vörös, Z., Narita, Y., & Bruno, R. 2014a, *ApJL*, **783**, L19
 Zaqarashvili, T. V., Vörös, Z., & Zhelyazkov, I. 2014b, *A&A*, **561**, A62
 Zaqarashvili, T. V., Zhelyazkov, I., & Ofman, L. 2015, *ApJ*, **813**, 123
 Zhang, J., & Dere, K. P. 2006, *ApJ*, **649**, 1100
 Zhelyazkov, I., Zaqarashvili, T. V., & Chandra, R. 2015, *A&A*, **574**, A55